ABSTRACT

Title of Document: CARBON COMPOSITES FOR LI-ION AND NA-ION BATTERIES

Yang Wen, Doctor of Philosophy, 2014

Directed By: Professor Chunsheng Wang
Department of Chemical and Biomolecular Engineering

Due to the high demand for power supply in hybrid vehicle and renewable energy storage, Li-ion battery (LIB) and Na-ion battery (NIB) technologies have developed rapidly in the past few years. LIB industry has bloomed for portable devices and hybrid electric vehicles, while NIB techniques have been revived for large-scale energy storage. In this dissertation, novel anode materials, including Si-graphene, Si-carbon nanotubes composites for LIB anodes, and expanded graphite for NIB anodes, were studied.

In LIB technology, Si is one of the most promising anode materials for next generation batteries because of its high theoretical capacity (~3598 mAh g^{-1}). However, the rapid capacity decay caused by the substantial volume change during the lithation/delithiation process limits the practical application of Si anode. In this dissertation, grahene and carbon nanotubes were used as frameworks to maintain the

integration and the electrical connection of Si during charge/discharge cycles. Both graphene-Si and CNT-Si species show superior performance and would be potentially beneficial for Si anode commercialization.

As for Na-ion battery, graphite, the most commonly used anode in Li-ion batteries, is not suitable for NIB due to its limit of interlayer distance. In this dissertation, expanded graphite (EG) with similar long-term-ordered layer structure as graphite and larger interlayer distance was synthesized for NIB anode. EG is expected to allow reversible Na^+ insertion to occur and accommodate Na^+ mostly by intercalation, which is similar to how graphite stores Li^+ in LIB. The atomic observation by *in situ* TEM study and linear scanning voltammetry analysis confirm the storage mechanism.

CARBON COMPOSITES FOR LI-ION AND NA-ION BATTERIES

By

Yang Wen

Dissertation submitted to the Faculty of the Graduate School of the
University of Maryland, College Park, in partial fulfillment
of the requirements for the degree of
Doctor of Philosophy
2014

Advisory Committee:
Prof. Chunsheng Wang, chair
Prof. John Cumings
Prof. Sheryl H. Ehrman
Prof. Liangbing Hu
Prof. Dongxia Liu

Dedication

To

My beloved parents and dear Y. Yang.

Life is a journey full of joy and pain. It is my great honor to sail along and share every memorable moment with you.

Acknowledgements

It is with immerse gratitude that I acknowledge the support and help of my advisor, Professor Chunsheng Wang, who not only guided me on research but more importantly delivered the spirit of tackling the most challenge problems in scientific topics. Without his guidance and persistent help, this dissertation would not have been possible.

I would like to thank my advisory committee members, Professor John Cumings, Professor Sheryl Ehrman, Professor Liangbing Hu and Professor Dongxia Liu; who ignited me and encouraged me along my PhD path.

My grateful thanks go to all my close collaborators, including but not limited to: Dr Yujie Zhu, Mr Alex Langrock, Dr Kai He, Dr Yunhua Xu, Mr Fudong Han, Dr Karen Gaskell and Mr Sang Yool Lee.

I also want to acknowledge all my labmates, friends and colleagues, who generously offer their help in the past years and make my life full of enjoyable moments.

Last but not the least; I want to thank my dear family for their continuous love and supports in my pursuit of PhD.

Table of Contents

List of Figures

List of Abbreviations

APS	Aminoprupyltrimethoxysilane
BET	Brunauer-Emmett-Teller
CMC	Carboxymethyl Cellulose
CNT	Carbon Nano Tubes
CV	Cyclic Voltammetry
CVD	Chemical Vapor Deposition
DMC	Dimethyl Carbonate
DWCNT	Double Wall Carbon Nanotubes
EC	Ethylene Carbonate
EDS	Energy Dispersive X-Ray Spectroscopy
EG	Expanded Graphite
EG	Expanded Graphite
FEC	Fluoroethylene Carbonate
FTIR	Fourier Transform Infrared Spectroscopy
GITT	Galvanostatic Intermittant Titration
GO(chapter 3)	Graphene Oxide
GO(chapter 5)	Graphite Oxide
HRTEM	High Resolution Transmission Electron
LIB	Li-ion Batteries
MCMB	Mesocarbon Microbeads
MWCNT	Multiwall Carbon Nanotubes
NIB	Na-ion Batteries
PC	Polycarbonate
PG	Pristine Graphite
SA	Sodium Alginate
SEI	Solid Electrolyte Interphase
SEM	Scanning Electron Microscopy
SSNMR	Solid State Nuclear Magnetic Resonance
SWCNT	Single Wall Carbon Nanotubes
TEM	Transmission Electron Microscopy

Chapter 1: Introduction and Overview

1.1 Li-ion Battery System

Lithium is the lightest metal among all the metals. Along with suitable electrochemical potentials, Li has been proved to be able to carry large energy content. Rechargeable Li-ion battery with high voltage, extraordinary energy density and superior capacity, has become one of the most important components in electronic devices and hybrid vehicles in the past centuries. The Li-ion cells are known as key components of modern portable, entertainment, computing and telecommunication devices nowadays.

The development of rechargeable Li-ion battery (LIB) can date back to 1912 when G. N. Lewis first discovered the advantage in using Li metal of primary Li cells. The primary Li cell was non-rechargeable. The active research did not begin until the 1950s when organic electrolyte, such as $LiClO_4$ in propylene carbonate, was developed. [1] The development and commercialization of primary Li-ion battery followed rapidly in the following 20 years. The primary Li-ion cells became popular in 1970s when people found their great advantage as power sources for small electronic devices, such as watches, implantable medical devices and calculators.

Over the same period, numerous elements and compounds were found to be capable of reversely reacting with Li metal and other alkaline metals. In the 1970s, the starting point of the history of these power alternatives was denoted when M.S. Wittingham proposed the LIB at the Binghamton University. Even though the concept of electrcochemical interaction and its potential use have been well defined

by 1972,[2,3] the commercialization of large secondary Li-ion cells was not established until 1980s because of the safety concerns. Two companies in Canada, Moli Energy, Ltd. and Ballard Power System, Inc. initialed the large scale LIB cells production and Moli Energy became the manufacture of rechargeable LIB in late 1980s. The first generation rechargeable LIB was based on Li/MoS_2. Unfortunately, the secondary cell industry did not last long before the recall of all the batteries in the cellular phone of NTT Japan provided by Moli Energy due to a fire incident involving cells. The recall directly led the company to bankruptcy and also brought worldwide attention to the safety issue related to Li metal usage in the primary and secondary LIB. The secondary LIB system has been highly developed in the past 30 years from then on. In current commercial LIB, Li metal is no longer used in the most the cells. Instead, graphite is widely accepted as one of the most popular LIB anode materials.

The secondary LIB system is also known as the "rocking chair Li-ion battery" since Li^+ exchanges back and forth between two electrodes. Both the names of rocking-chair battery and lithium-ion battery are widely used in current LIB cell industry, referring to the same type of batteries. Major components in a typical LIB involve anode, cathode, and electrolyte (Figure 1.1). When the cell under goes the charging process, lithium ions migrate to the negative electrode, known as anode side of the cell, and react with anode material. During the first charging process, a passive layer, known as solid electrolyte interphase (SEI) layer, is formed on the anode surface, which prevents the solvent from further reduction. The formation of SEI film usually will generate ~5% to 15% of irreversible capacity on the initial cycle. The cell gains energy and functions as an energy storage system. When driving a load through a

closed external circuit, cell goes through a discharge process. Lithium ions transfer from negative electrode to positive electrode within the cell and generate electron flowing in the external circuit to drive the load.

Common cathode materials are lithium containing compounds, for example, $LiFePO_4$, $LiMn_2O_4$, $LiNi_{0.5}Mn_{1.5}O_4$ and $LiCoO_2$. A typical cathode half-cell reaction involves valence change of the transition metal. The half-cell reaction, taking $LiCoO_2$ as an example, is:

$$LiCoO_2 \underset{discharge}{\overset{charge}{\rightleftharpoons}} Li_{1-n}CoO_2 + nLi^+ + ne^-$$

The most commonly used anode material in current commercial cells is graphite which accommodates Li^+ through intercalation reaction. The half-cell reaction of the graphite anode can be written as:

$$nLi^+ + ne^- + C \underset{discharge}{\overset{charge}{\rightleftharpoons}} Li_nC$$

Looking at the cell as a whole, the overall reaction is:

$$LiCoO_2 + C \underset{discharge}{\overset{charge}{\rightleftharpoons}} Li_{1-n}CoO_2 + Li_nC$$

The overall cell performance, such as energy storage ability and charging/discharging kinetics, highly relies on anode and cathode properties. Thus, anode/cathode material study is critical in LIB studies.

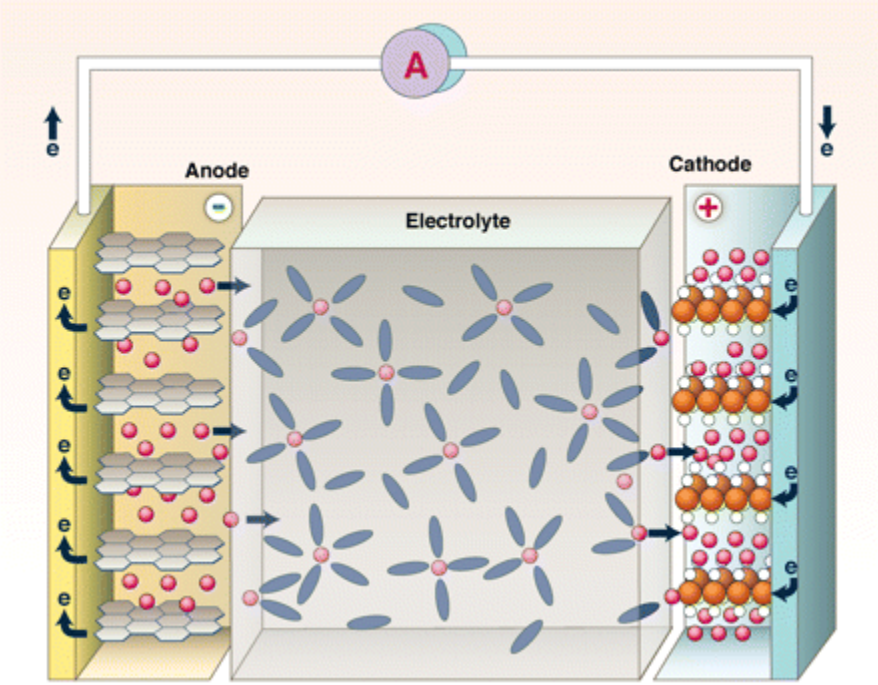

Figure 1.1 Schematic operating principle of a typical rechargeable LIB.[4]

1.2 Na-ion Battery System

The initial investigation of Na-ion battery (NIB) can date back to late 1970s and through the 1980s,[5-11] which is approximately the same time period of LIB development. Due to the pronounced advantages of LIB, such as higher energy density, higher potential and lower mass, the battery community shifted the attention away from NIB. The development of NIB went, in the opposite of LIB industry, very slowly in the past 30 years.

In the past years, as a result of fast growing portable electronic market, the sales of LIB increased dramatically. It is reported that more than one-quarter of the lithium-containing precursor was consumed by LIB industry and led to a steep price rise on Li_2CO_3 over the first quarter of the 21 century.[12] People started to worry that the lithium supply may be used up in a foreseeable future. On the other hand, the high

cost of LIB constrains the potential of LIB usage in large-scale energy storage, such like power grid. At this point, battery community regained the interest on NIB study. Na-ion battery is a good alternative to Li-ion battery when seeking a cheaper energy storage solution. Since sodium is two orders of magnitude more abundant than lithium (3% vs 0.02%) on earth, the general cost of NIB is expected to be much lower than LIB, which makes it possible to apply NIB for massive energy. NIB shares similar mechanism with LIB as well as some other advantages such as ambient working temperature. The major difference is that NIB use Na^+ ions as the charge carriers (Figure 1.2).

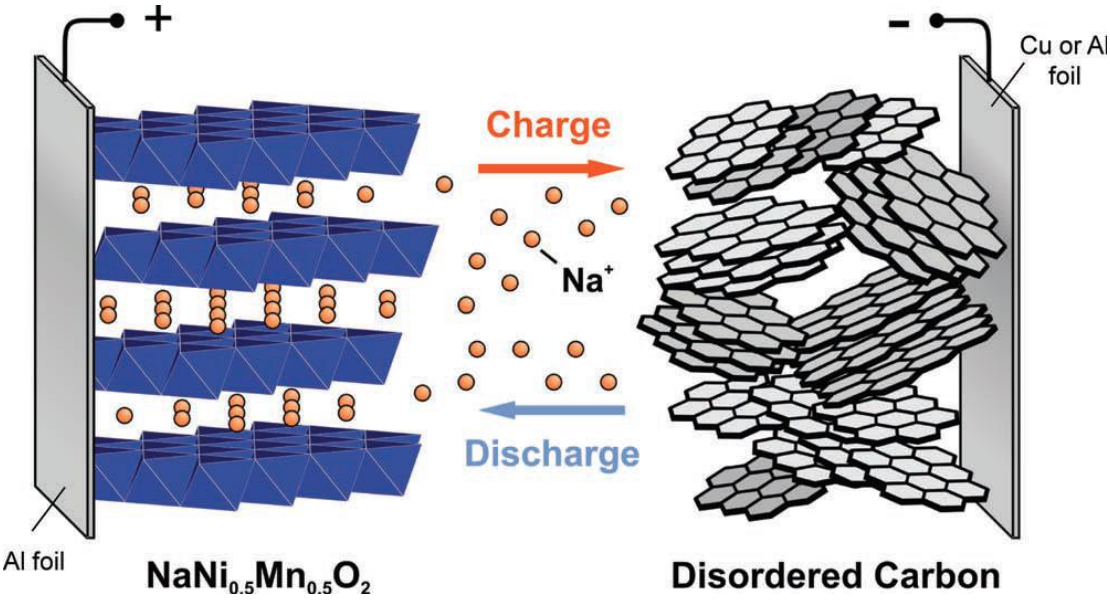

Figure 1.2 Schematic figure of a typical rechargeable NIB. [13]

Similar to LIB, in a typical charging process, sodium ion is released into the electrolyte from the positive electrode and intercalate with the negative electrode on the other side. The battery stores the energy. When discharging, Na-ion shifts back to

positive electrode, and releases the energy to drive a load. Not surprisingly, many of the LIB development experience can be easily adopted for NIB and many of the materials that are suitable for LIB and have been exhaustively studied in the past 20 years are also suitable for NIB. However, comparing to the blooming LIB industry, commercial NIB cells are still in the initial developing stage. Current study on NIB anodes are mainly on carbon materials which store Na^+ ion via intercalation reaction. Studies on NIB cathode are mainly focused on the layered transition metal oxides.

1.3 Graphitic Carbon, Graphene, Carbon Nanotubes and Their Applications in Battery System

Graphitic carbon refers to carbon material with three-dimensional crystalline structure and long-range ordered morphology. [14] Graphitic material has been widely used in current LIB system. As a typical graphitic carbon, graphite has been widely used in commercial lithium cells for decades. As advanced carbon material developed, new carbon materials, such as graphene and carbon nanotubes, became very polular. They have been investigated as energy storage material, electron conductivity additives or structure enhancement function material in today's LIB study.

It is interesting that, the graphitic material (graphite), graphene and carbon nanotubes share one common character that they are all built up by sp2 carbons, and can be cataloged as a family (Figure 1.3). Graphene can be considered as a 2D building material. When it's rolled up, it forms the 1D nanotubes. On the other hand, it can be stacked up into 3D graphite.

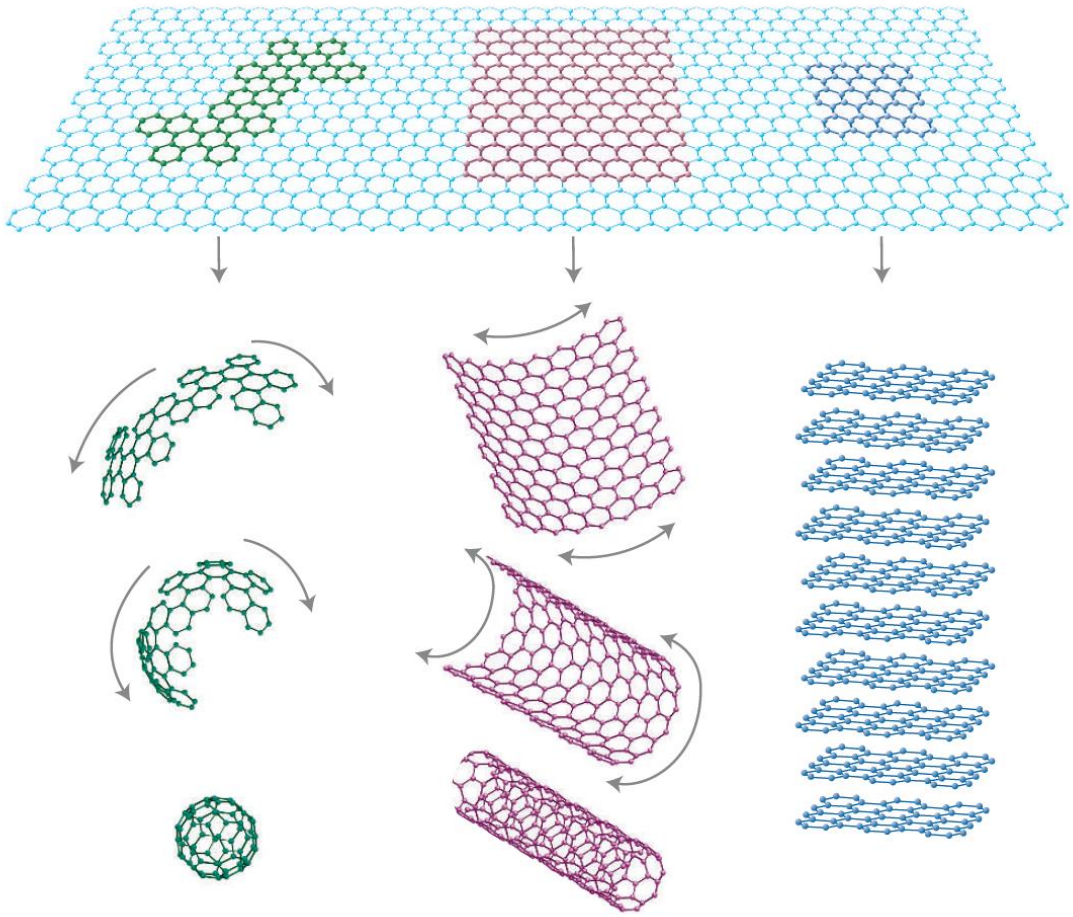

Figure 1.3 Schematic figure of relations between graphite, carbon nanotubes and graphene. [15]

In this section, graphitic carbon, graphene and carbon nanotubes materials will be discussed. A general review on related current LIB study will be covered.

1.3.1 Graphite and Graphitic Carbon

Graphite is one of the most commonly utilized anode materials in today's commercial LIB cells, due to various advantages such as low cost, superior Li ion intercalation potential and excellent cycling stability. [16-18]

Graphite is a specific type of carbon with a layered planar structure. Within each of the layers, each of the carbon atoms is sp2-hybridized and combines with three other sp^2-hybridized carbons. Carbon atoms are arranged in a regular hexagonal pattern located in parallel planes (Figure 1.4).

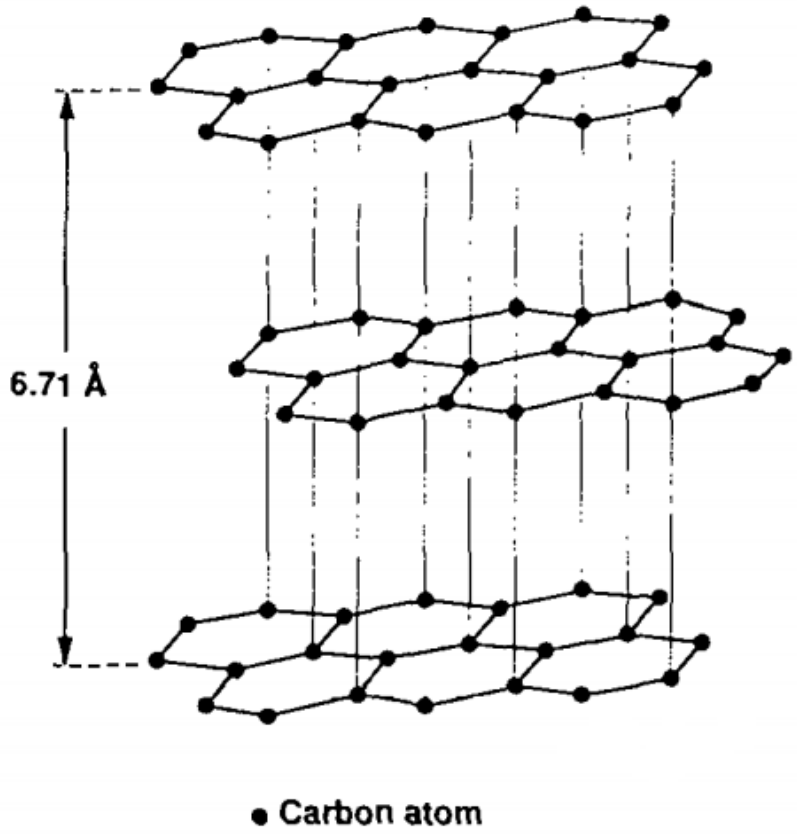

Figure 1.4 Three-dimensional schematic of the graphite structure. [19]

Historically speaking, graphite is the first type of carbon that was found to be capable of reversible lithiation.[20] The lithiation of graphite is a well-known intercalation reaction in which lithium ions are inserted into graphene layers. The 0.335nm interlayer spacing appears to be a perfect space for lithium ion to intercalate. The process involves phase transitions of 4 stages and a small scale volume expansion of

graphite (~12%). Theoretical capacity of graphite is 372mAh g^{-1} when the stoichiometry ratio of LiC_6 is reached. Ideally, the robust layer structure will regain the initial parallel morphology when the lithium ions are extracted from graphene layers. However, it is reported that the optimal behavior strongly depended on the electrolyte solution used. Exfoliation may occur due to co-intercalation of Li-ion and solvent molecule composites.[20,21] To prevent graphite anode from solvent exfoliation and stabilized the material, co-solvent system of dimethyl carbonate (DMC) and ethylene carbonate (EC) is widely used in today's LIB cells. [22,23]

As another important species in graphitic carbon, expanded graphite was also studied for potential LIB anode.[24] Expanded graphite is identified as graphite with wider *d* spacing. Currently, the most common way to achieve expended graphite is to heat-treat or electrochemically activate the mesocarbon microbeads (MCMB).

Although graphite is well known as superior anode in LIB system, the limited interlayer spacing constrains the potential for its application in NIB. There is no study reported on graphitic materials as NIB anode so far.

1.3.2 Graphene

Graphene is a single layer of graphite. It is known to have superior properties such as good electrical conductivity, superior mechanical strength, and excellent chemical stability.[15,25,26]

The easiest way to produce graphene is exfoliation of bulk graphite. This methodology can be cataloged into two ways. One is direct exfoliation of graphite by mechanical force. Common methods include adhesive-tape (scotch-tape) pealing[27] and wet ball milling[28]. This method is comparatively quick and easy. However, the

quality of the material (eg. numbers of layers, size of the graphene pieces) is comparatively random. When producing large amount of the material where high quality is needed, this method is not applicable.

The other common approach to synthesize graphene is through the cleavage of oxidized graphite, in which sonication or thermally cracking was generally used to peel off graphene layers. This method is also known as modified Hummer's method.[29] In this synthesis process, graphite firstly reacts with strong oxidization reagents to form graphite oxide. The formed oxygen containing groups will insert into graphite layers, resulting in graphite oxide with enlarged interlayer distance. In the following step, sonication can be applied to peel off the single layered or multi-layered graphene oxide. Then further chemical/thermal reduction of graphene oxide is conducted to achieve graphene. Alternatively, thermal reduction of graphite oxide with a high heating rate (10 $^{o}Cmin^{-1}$) can be used to achieve graphene in a single step. In this method, the fast heating rate promotes fast reduction reaction. The evaporation of reducing product such as CO_2 will crack the layer structure of graphite oxide, thus producing single layered/multi-layered graphene. Graphene, resulting from modified Hummer's method, has considerable amount of defects generated during the O-containing removal process, which can provide good transportation channels for Li^+.

Graphene has been widely used in LIB anodes and cathodes recently to improve the structure stability and material conductivity. [30-35] The common issue for using graphene in LIB anode is that it brings in larger surface area, which would lead into higher irreversible capacity at the first cycle due to SEI film formation. For the NIB research, even though the graphene composites were less studied, a few researches

were reported[36-43], demonstrating that graphene can improve the anode and cathode performance as conductive addictive and structure material in Na-ion batteries.

1.3.3 Carbon nanotubes

Carbon nanotube is another strong candidate for LIB electrode due to its unique electrochemical and mechanical properties. Similar to graphene, carbon nanotubes can function as conductive additive with much lower loading than conventional carbons (eg. graphite and carbon black). More additionally, carbon nanotubes can be assembled into free-standing electrode that has no binder and current collector (Figure 1.5). Since the "dead weight" attributed to the binder and current collector, the energy density (measured in Ah/g) would be greatly improved for the whole battery and it is promising for flexible light weight LIB.

Carbon nanotube structure weres first discovered in 1991 by Lijima [44]. After then, significant amount of research has been conducted to study the unique properties of carbon nanotubes, including the lithium vapor interaction and the electrochemical properties. As a consequence, more and more attentions are drawn to carbon nanotubes for LIB electrodes, both cathode and anode.[45-53] In most of the studies, active materials were mixed with carbon nanotubes (single wall or multi walls) to achieve the composites. Free-standing carbon nanotube paper was usually prepared by vacuum filtration.

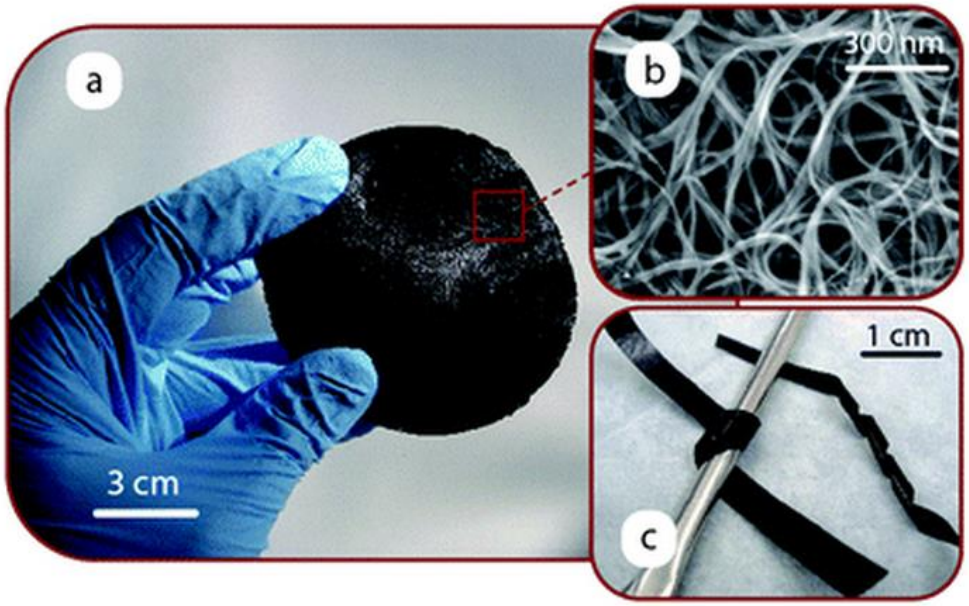

Figure 1.5 (a) Photograph of a free-standing single-wall-carbon naonutube (SWCNT) paper. (b) SEM image of the high purity SWCNTs. (c) Image of SWCNT paper strips which are bent around a curved surface and twisted without any unintended or irreversible deformation to illustrate the flexible mechanical properties.[54]

1.4 Electrochemical Terminologies and Calculations

1.4.1 Half cells and full cells

Generally speaking, an electrochemical cell (full cell) consists of two half cells, known as two electrodes (anode and cathode) in the battery. In laboratory scale, a typical cell (Li-ion battery, Na-ion battery, etc) usually consist of a specific active material as working electrode and a piece of metal (Li, Na. etc) as contour electrode. This type of device is also called half-cell since it is used to study specifically behavior of an anode or cathode material during the electrochemical reactions.

Each half cell has its own characteristic voltage, determined by its equilibrium reduction potentials. This equilibrium reduction potential under specific conditions can be calculated by Nernst equation (1.1)

$$E_{red} = E_{red}^{\theta} - \frac{RT}{zF} \ln \frac{a_{Red}}{a_{Ox}} \tag{1.1}$$

Where E_{red}^{θ} refers to the standard half cell potential measured under standard state, in which the effective solutes concentration is 1 mol dm^{-3}, the pressure is 1 atm and the temperature is 25 °C.*R* is the ideal gas constant, *T* is the absolute temperature, *z* is the amount of electrons that have been transferred during reactions in moles, *F* is the Faraday constant, and *a* is chemical activity.

In a full cell that consists of two half-cell reactions, the ultimately equivalent can be calculated as in (1.2)

$$E_{cell} = E_{cell}^{\theta} - \frac{RT}{zF} \ln Q \tag{1.2}$$

Where Q is the reaction quotient. And E_{cell}^{θ} is the standard cell potential that can be calculated by (1.3)

$$E_{cell}^{\theta} = E_{cathode}^{\theta} - E_{anode}^{\theta} \tag{1.3}$$

In this dissertation, all the cells/batteries refer to half cells since they are aimed to study specific anode material behavior during electrochemical reactions. Thus all the calculations are based on half cells.

1.4.2 Power density and energy density

Power density usually refers to the amount of power that can be provided by the battery measured in per mass or volume unit. Power is measured in energy transfer in

time unit. Thus this character is more related to the electron/ions transfer speed within the cells.

On the other hand, energy density refers to the maximum energy that can provided by the cell per unit mass or volume. This number is usually discussed under certain discharging rate and it can be calculated by specific capacity of the cell multiply by the average operating voltage.

In this dissertation, materials are evaluated mostly on capacity under certain charging/discharging rate. The ability of providing high power is also evaluated by rate capability performance.

1.4.3 Theoretical capacities and actual capacity based on experiment.

Theoretical capacity refers to the amount of electricity involved in a specific electrochemical reaction process. The theoretical capacity of a specific material can be evaluated by specific molar capacity and specific mass capacity. All the specific capacities that are discussed in this dissertation are referring to the specific mass capacity with unit of mAh g^{-1}. And it is calculated by (1.4)

$$C_{specific} = \frac{nF}{M_t} \tag{1.4}$$

Where n refers to the amount of electrons that have been transferred during the half cell reaction, F is the Faraday constant and M_t is the molecular mass of the electrochemical active component.

The actual specific capacity discussed in this dissertation is calculated based on electrochemical process (charging/discharging) time and current density by (1.5)

$$C_{real,specific} = \int I d_t \tag{1.5}$$

Where *I* is the current density. And it is measured based on electrochemical active material in mA g^{-1}.

1.5 Related References

1 Jasinski, R. High-energy Batteries. *Plenum Press, New York* (1967).

2 Steele, B. C. H. in Fast Ion Transport in Solids (ed. Van Gool, W.) 103-109 (1973).

3 Armand, M. B. in Fast Ion Transport in Solids (ed. Van Gool, W.) 665–673 (1973).

4 Dunn, B., Kamath, H., & Tarascon, J.-M. Electrical Energy Storage for the Grid: A Battery of Choices. *Science* 334, 928-935 (2011).

5 Whittingham, M. S. chemistry of intercalation compounds metal guests in chalcogenide hosts. *Prog. Solid St. Chem.* 12, 41-99 (1978).

6 Nagelberg, A. S. & Worrell, W. L. A thermodynamic study of sodium-intercalated TaS_2 and TiS_2. *J. Solid State Chem.* 29, 345-354 (1979).

7 Delmas, C., Braconnier, J.-J., Fouassier, C., & Hagenmuller, P. Electrochemical intercalation of sodium in Na_xCoO_2 bronzes. *Solid State Ionics* 3-4, 165-169 (1981).

8 Shacklette, L. W., Jow, T. R. & Townsend, L. Rechargeable electrodes from sodium cobalt bronzes. *J Electrochem Soc* 135, 2669-2674 (1985).

9 Tarascon, J.-M. & Hull, G. Sodium intercalaction into the layered oxides Na_xMoO_4. *Solid State Ionics* 22, 85-96 (1986).

10 Jow, T. R., Shacklette, L., Maxfield M &Vernick D. The role of conductive polymers in alkali-metal secondary electrodes. *J Electrochem Soc* 134, 1730-1733 (1987).

11 West, K, Zachau-Christiansenm, B., Jacobsen, T. & Skaarup, S. Sodium insertion in vanadium oxides. *Solid State Ionics* 30, 1128-1131 (1988).

12 Slater, M. D., Kim, D., Lee, E., & Johnson, C. S. Sodium-Ion Batteries. *Adv. Funct. Mater.* 23, 947-958 (2013).

13 Komaba, S. *et al.* Electrochemical Na Insertion and Solid Electrolyte Interphase for Hard-Carbon Electrodes and Application to Na-Ion Batteries. *Adv.Func. Mater.* 21, 3859-3867 (2011).

14 E. Fitzer, K.-H. K., H. P. Boehm, H. Marsh. Recommended terminology for the description of carbon as a solid (IUPAC Recommendations 1995). *Pure and Applied Chemistry* 67, 473-506 (2009).

15 Novoselov, A. K. G. a. K. S. The rise of graphene. *Nature Mater.* 6, 183-191 (2007).

16 Kang, B. & Ceder, G. Battery materials for ultrafast charging and discharging. *Nature* 458, 190-193 (2009).

17 Tarascom, J.-M. & Armand, M. Issues and challenges facing rechargeable lithium batteries. *Nature* 414, 359-367 (2001).

18 Simon, P. & Gogotsi, Y. Materials for electrochemical capacitors. *Nature mater.* 7, 845-854 (2008).

19 Pierson, H. O. *Handbook of carbon, graphite, diamonds and fullerenes: processing, properties and applications*. (William Andrew, 1994).

20 Fauteux, D. & Koksbang, R. Rechargeable lithium battery anodes: alternatives to metallic lithium. *J. Appl. electrochem.* 23, 1-10 (1993).

21 Winter, M., Besenhard, J. O., Spahr, M. E. & Novak, P. Insertion electrode materials for rechargeable lithium batteries. *Adv. mater.* 10, 725-763 (1998).

22 Aurbach, D. *et al.* The Study of Electrolyte Solutions Based on Ethylene and Diethyl Carbonates for Rechargeable Li Batteries II. Graphite Electrodes. *J.of Electrochem. Soc.* 142, 2882-2890 (1995).

23 Ein-Eli, Y. Dithiocarbonic anhydride (CS_2)—a new additive in Li-ion battery electrolytes. *J. Electroanal. Chem.*531, 95-99 (2002).

24 Bok, H. K. & Oh, S. M. Electrochemical activation of expanded graphite electrode for electrochemical capacitor. *J. Electrochem. Soc.* 155, A685-A692 (2008).

25 A. H. Castro Neto, F. G., N. M. R. Peres, K.S. Novoselov, A.K. Geim. The Electronic Properties of Graphene. *Rev. Mod. Phys.* 81, 109-162 (2009).

26 Sasha Stankovich, D. A. D., Geoffrey H. B. Dommett, Kevin M. Kohlhaas, Eric J. Zimney, Eric A. Stach, Richard D. Piner, SonBinh T. Nguyen and Rodney S. Ruoff. Graphene-based Composite Materials. *Nature* 442, 282-286 (2006).

27 Novoselov, K. S. *et al.* Electric field effect in atomically thin carbon films. *science* 306, 666-669 (2004).

28 Zhao, W. *et al.* Preparation of graphene by exfoliation of graphite using wet ball milling. *J. Mater. Chem.* 20, 5817-5819 (2010).

29 Hummers JR, W.S. & Offeman, R. E. Preparation of Graphitic Oxide. *J. Am. Chem. Soc.* 80, 1339-1339 (1957).

30 Wu, Z.-S. *et al.* Graphene anchored with Co3O4 nanoparticles as anode of lithium ion batteries with enhanced reversible capacity and cyclic performance. *ACS nano* 4, 3187-3194 (2010).

31 Zhou, G. *et al.* Graphene-wrapped Fe3O4 anode material with improved reversible capacity and cyclic stability for lithium ion batteries. *Chem. Mater.* 22, 5306-5313 (2010).

32 Wang, H. *et al.* Mn3O4− graphene hybrid as a high-capacity anode material for lithium ion batteries. *J. Am. Chem. Soc.* 132, 13978-13980 (2010).

33 Yoo, E. *et al.* Large reversible Li storage of graphene nanosheet families for use in rechargeable lithium ion batteries. *Nano Lett.* 8, 2277-2282 (2008).

34 Wang, H. *et al.* Graphene-wrapped sulfur particles as a rechargeable lithium–sulfur battery cathode material with high capacity and cycling stability. *Nano lett.* 11, 2644-2647 (2011).

35 Wang, D. *et al.* Self-assembled TiO2–graphene hybrid nanostructures for enhanced Li-ion insertion. *ACS nano* 3, 907-914 (2009).

36 Su, D., Ahn, H. J. & Wang, G. SnO_2@graphene nanocomposites as anode materials for Na-ion batteries with superior electrochemical performance. *Chem. Commun.* 49, 3131-3133 (2013).

37 Zhu, H. *et al.* Free-standing $Na_{2/3}Fe_{1/2}Mn_{1/2}O_2$@graphene film for a sodium-ion battery cathode. *ACS appl. Mater. Interfaces* 6, 4242-4247 (2014).

38 Wang, Y.-X. *et al.* Ultrafine SnO_2 nanoparticle loading onto reduced graphene oxide as anodes for sodium-ion batteries with superior rate and cycling performances. *J. Mater.Chem. A* 2, 529-534 (2014).

39 Fan, Q., Lei, L., Yin, G., Chen, Y. & Sun, Y. Direct growth of $FePO_4$/graphene hybrids for Li-ion and Na-ion storage. *Electrochemistry Communications* 38, 120-123 (2014)

40 Ling, C. & Mizuno, F. Boron-doped graphene as a promising anode for Na-ion batteries. *Phys. Chem. Chem. Phys.* 16, 10419-10424 (2014).

41 Su, D., Dou, S. & Wang, G. WS_2@graphene nanocomposites as anode materials for Na-ion batteries with enhanced electrochemical performances. *Chem. Commun.* 50, 4192-4195 (2014).

42 Pang, G. *et al.* Synthesis of NASICON-type structured $NaTi_2(PO_4)_3$-graphene nanocomposite as an anode for aqueous rechargeable Na-ion batteries. *Nanoscale.* 6, 6328-6334 (2014).

43 Zhang, Y. *et al.* Activation of electrochemical lithium and sodium storage of nanocrystalline antimony by anchoring on graphene via a facile in situ solvothermal route. *J. Power Sources* 247, 204-212 (2014).

44 Iijima, S. Helical microtubules of graphitic carbon. *Nature* 354, 56-58 (1991).

45 Reddy, A. L. M., Shaijumon, M. M., Gowda, S. R. & Ajayan, P. M. Coaxial MnO_2/carbon nanotube array electrodes for high-performance lithium batteries. *Nano Lett.* 9, 1002-1006 (2009).

46 Che, G., Lakshmi, B. B., Fisher, E. R. & Martin, C. R. Carbon nanotubule membranes for electrochemical energy storage and production. *Nature* 393, 346-349 (1998).

47 Zhang, Y. *et al.* Composite anode material of silicon/graphite/carbon nanotubes for Li-ion batteries. *Electrochim. Acta* 51, 4994-5000 (2006).

48 Li, X., Kang, F., Bai, X. & Shen, W. A novel network composite cathode of $LiFePO_4$/multiwalled carbon nanotubes with high rate capability for lithium ion batteries. *Electrochem. Commun.* 9, 663-666 (2007).

49 Morris, R. S., Dixon, B. G., Gennett, T., Raffaelle, R. & Heben, M. J. High-energy, rechargeable Li-ion battery based on carbon nanotube technology. *J. Power Sources* 138, 277-280 (2004).

50 Chen, J. *et al.* Flexible, aligned carbon nanotube/conducting polymer electrodes for a lithium-ion battery. *Chem. mater.* 19, 3595-3597 (2007).

51 Shu, J., Li, H., Yang, R., Shi, Y. & Huang, X. Cage-like carbon nanotubes/Si composite as anode material for lithium ion batteries. *Electrochem. commun.* 8, 51-54 (2006).

52 Cui, L.-F., Hu, L., Choi, J. W. & Cui, Y. Light-weight free-standing carbon nanotube-silicon films for anodes of lithium ion batteries. *Acs Nano* 4, 3671-3678 (2010).

53 de las Casas, C. & Li, W. A review of application of carbon nanotubes for lithium ion battery anode material. *J. Power Sources* 208, 74-85 (2012).

54 Landi, B. J., Ganter, M. J., Cress, C. D., DiLeo, R. A. & Raffaelle, R. P. Carbon nanotubes for lithium ion batteries. *Energy Env. Sci.* 2, 638-654 (2009).

Chapter 2: Background

2.1 Challenges of Li-ion Battery Anodes

Li-ion batteries (LIB) are an attractive energy storage system for today's electronic devices and hybrid vehicle industry. [55] As one of the main components of LIB, anode materials play a critical role in the LIB performance. Current LIB anodes can be cataloged into three types according to their interaction with Li-ion: intercalation (Figure 2.1 (a)), conversion (Figure 2.1(b)) and alloying. Today the most studied materials are mainly carbon species, metal oxides, and alloys.

Carbon anodes are typical intercalation anode materials and can be divided into two species. One is graphite, which is the most used anode in current commercial LIBs. Graphite has a robust layer structure and it can sustainably provide reversible Li^+ storage over thousand cycles with a capacity of 372 mAh g^{-1}. The other branch in carbon LIB anodes involves soft carbon and hard carbon. Soft carbon and hard carbon are amorphous carbons with localized nanocrystalline structure. It is reported that both soft carbon and hard carbon can deliver a very high reversible capacity towards Li^+. However, serious voltage hysteresis appears in the delithiation process which compromises the performance and hard carbons are difficult to prepare.[56,57]

Metal oxide as LIB anodes has been extensively studied due to generally high capacity (500-1000 mAh g^{-1}). Most studied materials include SnO_2, TiO_2, Fe_2O_3, and Cu_2O. Common problems for metal oxide anode are low first cycle coulombic efficiency and large potential hysteresis.

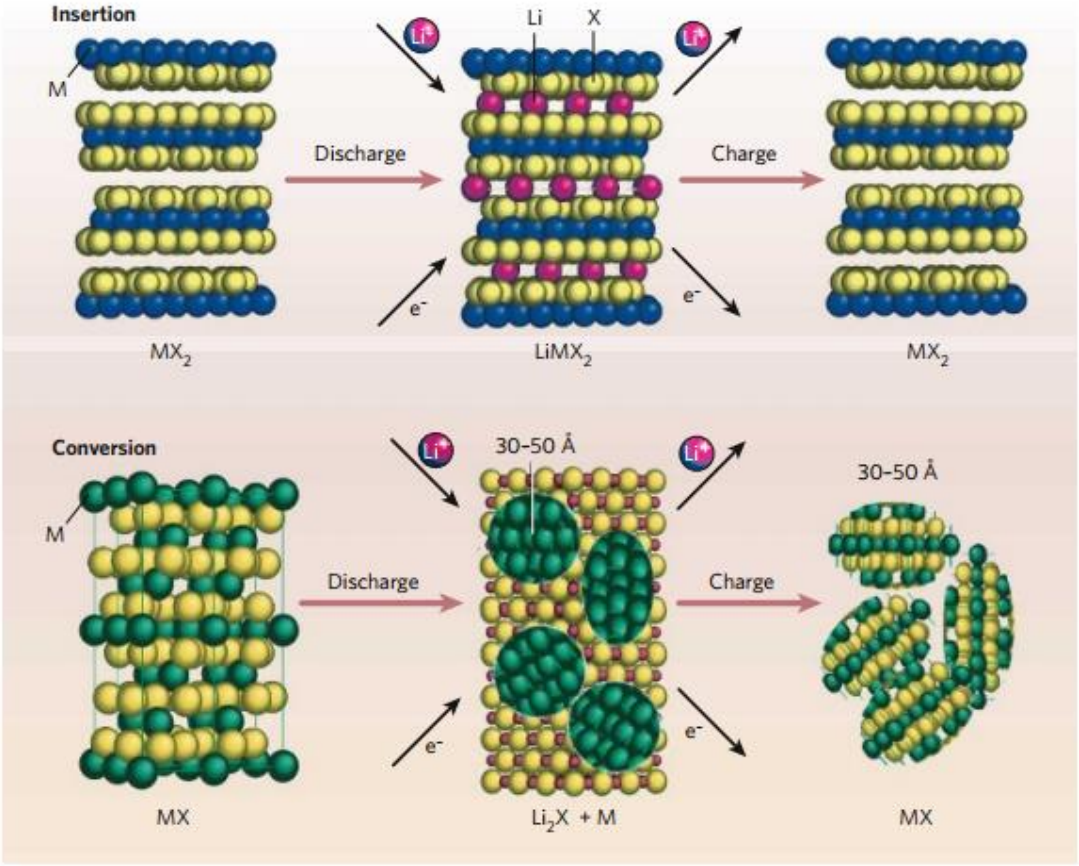

Figure 2.1 Schematic image shows the reaction mechanism occurring during discharge for (a) intercalation and (b) conversion. [58]

Alloy anode studies are mainly focused on group IV and group V elements, such as Si, Sn, Ge, Pb, P and Bi, and some of the metal elements, such as Ga, Zn, and Mg. [59,60] Alloy anodes are well-known to have high capacity and moderate operating potential towards Li/Li^+. The main challenge for alloy anode is that the large volume change (usually ~300%) during cycling. The mechanical stress caused by volume change may affect the integrity of the active mass, result in poor capacity retention. In addition, the alloying reaction occurs in a low potential, where the reduction of solution species would occur, forming thin layers (known as SEI films) on the anode

surface. This thin layer is known to be critical to achieve passivation of the Li-ion and prevent the continuous reduction of electrolyte solution. The continuous volume change in alloy/de-alloy process was found to crack the SEI fillm and generate irreversible capacity in each cycle. As a result, challenges remained towards to the commercialization of long-cycling alloy anode material in LIB. For example, silicon has a very high capacity of ~3589mAh g^{-1} which is the highest capacity among all the anodes. It has been considered as the most promising next generation anode in advanced LIB. However, commercialization of Si anode is still under development due to generally poor cycle life.

2.2 Challenges of Na-ion Battery Anodes

Studies on NIB anodes are comparatively less intensive than LIB anodes. Most investigated materials are carbons, metal phosphates and sodium metal oxides (Figure 2.2).[12] As Na ions cannot intercalate between carbon sheets, most carbon anodes in NIB are amorphous carbons with regional ordered graphene. A considerable amount of the Na ions are inserted into pores and voids. Metal phosphates such as $NaTi_2(PO_4)_3$ was reported as anodes with low operating potential which is an attractive feature for aqueous NIB.[61] Sodium metal oxides such as $Na_2Ti_3O_7$ and $NaVO_2$ were also reported to show low potential intercalation reaction towards Na^+.[62,63] However, practical applications still remain a challenge due to the large voltage variation and high sensitivity towards air.

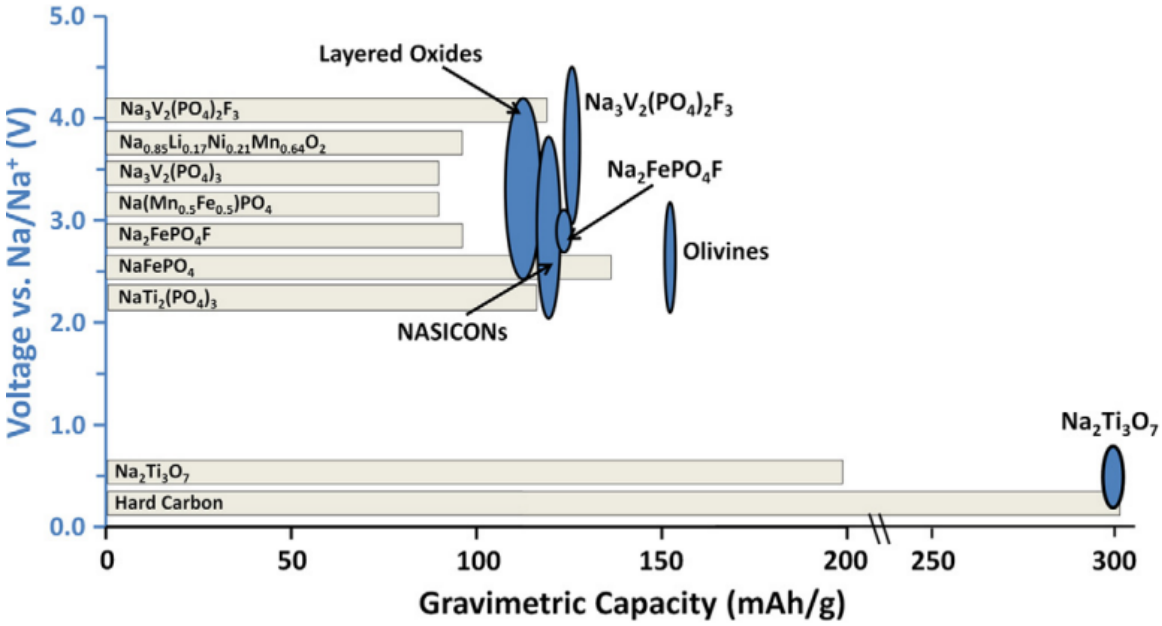

Figure 2.2 Key positive and negative electrode intercalation materials for sodium-ion batteries.[64]

2.3 Scope of the Dissertation

This dissertation is focused on advanced anode material fabrications for Li-ion batteries and Na-ion batteries. The main strategy is to utilize various carbon composites including graphitic carbon, graphene and carbon nanotubes as functional structure material to stabilize high energy density active material, for example, silicon for Li-ion batteries. More additional, modified carbon will also be studied as advanced Na-ion battery anode material as part of the anode design.

The work of the dissertation will be discussed in 3 chapters. Chapter 3 and chapter 4 are mainly about Li-ion battery anodes, while chapter 5 is about Na-ion battery anodes.

In chapter 3 and chapter 4, different approaches, such as aerosol pyrolysis (chapter 3) and chemical vapor deposition (chapter 4), were used to fabricate carbon – encapsulated/-entangled Si nanoparticles. Different type of carbon material, such as graphene (chapter 3) and carbon naotubes (chapter 4), were utilized as structure functional materials to enhance the structure stability and improve the conductivity. Fundamental kinetic study and electrochemical analysis were performed to study the lithiation/delithiation process.

In chapter 5, expended graphite will be designed, synthesized and studied as advanced NIB anode. *In situ* TEM was conducted as atomic scale observation for detailed fundamental mechanism study chapter 5.

2.4 Related References

55 Johan, C. & Rydha, B. S. Impact on global metal flows arising from the use of portable rechargeable batteries. *Sci. Total Environ.* 302, 167-184 (2003).

56 Hideto Azuma), H. I., Shin'ichiro Yamada, Koji Sekai. Advanced carbon anode materials for lithium ion cells. *J. Power Sources* 81-82, 1-7 (1999).

57 Dahn, J. D., Zheng, T., Liu, Y.-H. & Xue, J. S. Mechanisms for Lithium Insertion in Carbonaceous Materials. *Science* 270, 590-593 (1995).

58 Armand, M. & Tarascon, J. M. Building better batteries. *Nature* 451, 652-657 (2008).

59 Holzapfel, M., Buga, H., Scheifele, W., Novák, P. & Petrat, F.-M. A new type of nano-sized silicon/carbon composite electrode for reversible lithium insertion. *Chem.Commun.* 1566-1568 (2005).

60 Cheol-Min Park, J.-H. K., Hansu Kim and Hun-Joon Sohn. Li-alloy based anode materials for Li secondary batteries. *Chem. Soc. Rev.* 39, 3115-3141 (2010).

61 Park, S. II, Gocheva, I., Okada, S. & Yamaki, J.-I. Yamaki. Electrochemical properties of $NaTi_2(PO_4)_3$ anode for rechargeable Aqueous sodium-ion batteries. *J. Electrochem. Soc.* 158, A1067-A1070 (2011).

62 Senguttuvan, P., Rousse, G., Seznec, V., Tarascon, J.-M. & Palacín, a. M. R. $Na_2Ti_3O_7$: Lowest Voltage Ever Reported Oxide Insertion Electrode for Sodium Ion Batteries. *Chem. Mater.* 23, 4109-4111 (2011).

63 Liua, H., Zhou, H., Chena, L., Tanga, Z., & Yang, W. Electrochemical insertion/deinsertion of sodium on NaV_6O_{15} nanorods as cathode material of rechargeable sodiumbased batteries. *J. Power Sources* 196, 814-819 (2011).

64 Ellis, B. L. & Nazar, L. F. Sodium and sodium-ion energy storage batteries. *Curr. Opin. Solid State Mater. Sci.* 16, 168-177 (2012).

Chapter 3: Graphene-bonded and –Encapsulated Si Nanoparticles as Anode for Li-ion Batteries

3.1 Introduction

As electric vehicles and portable electronic device technology develop, the demand for lithium ion batteries with high energy density and long cycle life has increased rapidly in recent years. [58,65-67] Silicon (Si) is a promising anode material due to its high theoretical storage capacity of ~3600 mAh g^{-1} which is an order of magnitude beyond graphite anodes in current commercial cells. Besides, it features a low discharge potential, low cost, high natural abundance, and environmental benignity, which make it highly attractive to the lithium ion battery industry. [68,69] However, it has been difficult to develop a practical Si anode since significant structure and volume changes (around 270%) occur during the lithiation/delithiation process, resulting in poor cycle life and low coulombic efficiency. To improve electrochemical performance of Si anodes, various nano-structured Si anodes, including Si nanowires, Si nanotubes, hollow Si nanospheres, and carbon-coated yolk-shell structured Si composites, were developed.[15,25,26,70] Recently, graphene has been used in Si anodes to buffer the volume changes and improve electronic conductivities due to its unique properties, such as superior electrical conductivity, high surface area (2600 m^2 g^{-1}), excellent chemical stability, and strong mechanical strength. [15,25,26] The most common method to prepare nano-Si/graphene composites is filtering of an aqueous nano-Si and graphene oxide (GO) suspension followed by reducing treatment or a one-step aerosol spray of aqueous nano-Si and GO suspension. [70-74] However, due to the

tendency for aggregation of Si nanoparticles in GO suspension, it is challenging to synthesize a uniform Si/graphene composite, which is critical to achieve long cycling life of Si/graphene anodes. If Si nanoparticles can be well dispersed and bonded to GO in the Si-GO suspension, a uniform Si/graphene composite can be obtained by either a two-step filtering/annealing process or one-step aerosol spray.

In this study, (3-aminopropyl)trimethoxysilane (APS) functionalized Si nanoparticles with strong bonds to micro-sized graphene shells were synthesized by a scalable aerosol method (Figure 3.1). APS is a special compound with a trimethoxysilane group on one end and amino group on the other. Firstly, Si nanoparticles were uniformly dispersed in an aqueous solution (Scheme 1a). The trimethoxysilane group reacts with SiO_2 on the Si nanoparticle surface (Scheme 1b) to functionalize the Si surface. When mixing with GO suspension, the amino group on the other end of APS interacts with the carboxylic group on GO to form a strong bond between GO and Si (Scheme 1c). The APS groups can also provide great steric hindering between Si nanoparticles to prevent them from aggregation in the suspension solution. The uniform aqueous dispersion of GO sheets and Si nanoparticles was nebulized to form aerosol droplets (Scheme 1d) and passed through a preheated tube furnace by N_2 as carrier gas. (Scheme 1e) In the aerosol spray process, water was quickly evaporated and GO was partially reduced resulting in a uniform graphene bonded and encapsulated nano-Si composite (Scheme 1f). For electrode preparation, sodium alginate was utilized to replace carboxymethyl cellulose (CMC) to further improve the interaction between the graphene-bonded-and-encapsulated-Si groups and current

collector (Scheme 1g). The optimized design of anode exhibited superior cycling stability and rate capability.

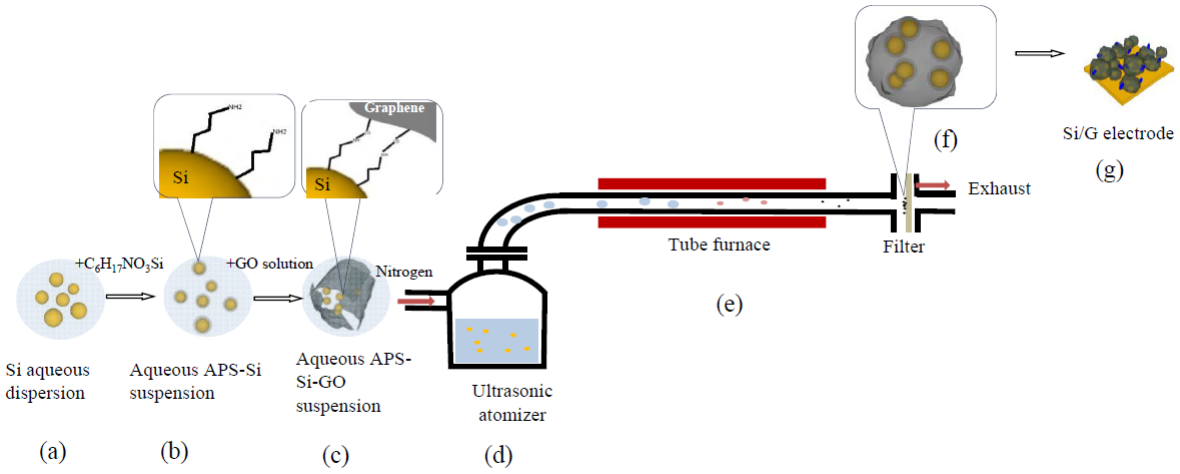

Figure 3.1 Schematic procedure for the synthesis of graphene bonded and encapsulated nano-Si composite.

3.2 Experimental Section

3.2.1 Graphene oxide (GO) synthesis

Graphite oxide was synthesized through a modified Hummer's method. [29] Graphite powder (1g, synthetic, 99.999%, Sigma Aldrich) and $NaNO_3$ (0.5 g, reagent plus, Sigma Aldrich) were mixed up with concentrated sulphuric acid (95%-98%, ACS reagent, Sigma Aldrich). Then $KMnO_4$ (3 g, ACS reagent, Sigma Aldrich) was added into the mixture while stirring in an ice bath, with the temperature maintained below 20 ^{o}C. After 10 minutes, the temperature was bring up to 35 ^{o}C and maintain at certain temperature in oil bath. A brown paste was obtained after 30 minutes. Distilled water (46 mL) was then added into the mixture to dilute the paste and the temperature was increased to 98 ^{o}C and held for 15 minutes. Warm water (140 mL)

was further added for dilution and H_2O_2 (20 mL, 30 wt % in H_2O, Sigma Aldrich) was then added into the liquid mixture. Liquid turned golden while adding. Then the resulting mixture was filtered out while hot and the solid (graphite oxide) was carefully dried out.

The fore-mentioned graphite oxide was then dispersed in distilled water and the mixture was sonicated for 30 minutes using a horn sonicator, followed by another two hours of sonication in a water bath sonicator, resulting in GO suspension.

3.2.2 Silicon dispersion and functionalization

To form a uniform SiO_2 layer on the surface of Si nanoparticles, Si nanoparticles were first oxidized in a mixture of sulphuric acid and hydrogen peroxide. These oxidized Si nanoparticles were then dispersed into distilled water and sonicated for 10 minutes using a horn sonicator, followed by another one hour sonication in a water bath sonicator to create a homogenous suspension of Si nanoparticles.10 wt% aminoprupyltrimethoxysilane (APS) (97%, Sigma Aldrich) was added to the Si suspension to functionalize the Si surface. The mechanism of the reaction involved is shown below

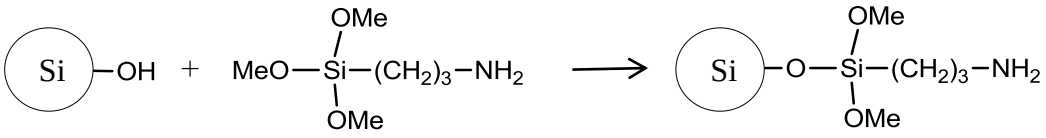

3.2.3 Homogenous Si-GO suspension

Homogenous Si-GO suspensions were obtained by slowly adding the aqueous nano-Si suspension into the GO suspension while stirring at room temperature. Terminal NH_2 groups on APS-Si reacts with COOH groups on GO to form an amide bond. Mechanism of reaction involved is shown below.

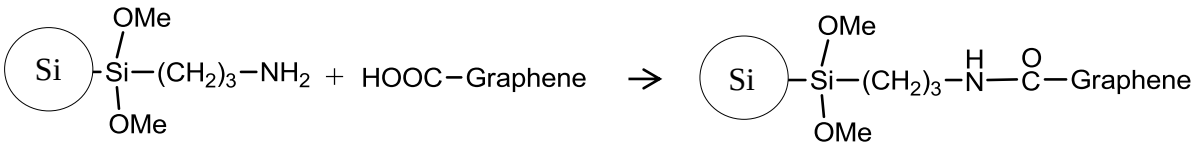

3.2.4 Si/G synthesis using aerosol spray process

The suspension of graphene bonded Si nanoparticles was nebulized by an ultrasonic atomizer. The aerosol droplets were carried by N_2 gas at a volumetric flow rate of 1 L/min to flow through a preheated horizontal tube (ID = 1.0 inch, length =32 inch) with a setting temperature at 700 ^{o}C. A control temperature test shows that the central temperature in the tube is expected to be ~50 °C lower than the setting temperature, thus the reaction is expected to take place at 650 °C. The bonds between Si nanoparticles and GO, and the rapid solvent evaporation force single-layered graphene to wrap up Si nanoparticles quickly. The rapid evaporation of the solvent would result in loss of solvent stablization and thus the crumple morphology. [75,76] The graphene would form a close shell to reduce the surface energy and the edges. The resulting graphene encapsulated Si composite was collected by a PTFE membrane. Since the reaction time in the furnace is short (< 3 seconds), GO was partially reduced, and part of the amide bond would survive. This unique structure provides sufficient connection between the two components and good conductivity as well. The resulting APS-Si-G composite appeared as black powder. Graphene-encapsulated Si anode without functionalization was also prepared by similar method.

3.2.5 Materials characterization

The morphology of the graphene-encapsulated Si was characterized by scanning electron microscopy (SEM) in the University of Maryland Nanocenter. The percentage of graphene in the composite was determined by thermogravimetric analysis (TGA). Powder sample was loaded into the TGA equipment (CAHN TG 2131, USA) with control bucket. The sample was heated from 200 °C to 750 °C in air atmosphere at a heating rate of 10°C per min. The APS-Si, GO and APS-Si-graphene composite samples were characterized by Fourier transform infrared spectroscopy (FTIR) on a high resolution infrared spectrometer (Model 670, Thermo Nicolet, USA). Powder samples were pressed into pellets and scanned from 4000 cm^{-1} to 650 cm^{-1} in air.

Electrochemical testing graphene-encapsulated Si electrodes were prepared by the slurry coating method. The active material was mixed with 10 wt% binder (CMC or sodium alginate) and milled for 30 minutes to form a slurry. Then, the obtained slurry was cast on copper foil and dried in a vacuum oven at 100 °C overnight. The loading amount of active material was ~ 0.5mg cm^{-2}. Coin cells, consisting of a graphene-encapsulated Si working electrode, a lithium metal counter electrode, Celgard 3501 separator, and 1.0 M $LiPF_6$ in dimethyl carbonate (DMC) : fluoroethylene carbonate (FEC) (1:1) co-solvent liquid electrolyte, were assembled in an argon-filled glove box for electrochemical tests.

Galvanostatic charge/discharge was performed using an Arbin test station. Cells were cycled between 0.002 V and 1.5 V at different currents. After the cell reached the cut off voltages, it was relaxed for 10 mins before subsequent charge or discharge. Cyclic

voltammetry (CV) test with voltage ranging from 0 V to 3 V was performed at a scan rate of 0.1 mV s^{-1} using a Solatron 1260/1287 Electrochemical Interface (Solatron Metrology, UK).

For the rate capability tests, cells were pre-cycled for 20 cycles for activation and then charged-discharged at various C rates between 0.002 V and 1.5 V. The capacity is calculated based on the overall mass of Si and graphene.

3.3 Result and Discussion

3.3.1 Materials Characterization

Figure 3.2 a show the SEM images of APS functionalized Si @ graphene (APS-Si-G) and Figure 3.2 b is the magnified view of the green square in Figure 3.2 a. Figure 1c shows the bare Si @ graphene (Si-G). The Si nanoparticles in both Si-G and APS-Si-G samples were well wrapped by graphene. Unwrapped Si nanoparticles were not observed, suggesting high yield of graphene-encapsulated Si composite in the aerosol process. The amount of Si nanoparticles wrapped by each graphene sheet in the APS-Si-G sample (Figure 3.2 a) is much less than that in Si-G sample (Figure 3.2 c) although the ratio of graphene to Si is the same for both samples in the precursors. This is because the functional groups on the APS-Si surface provide steric hindering between Si nanoparticles thus preventing Si nanoparticles from aggregation. This unique nano-structure of APS-Si-G not only improves the electronic conductivity of active materials, but also provides void space to accommodate the volume change of Si nanoparticles during lithiation, maintaining high electronic conductivity of the composite. The defects on graphene sheets generated during oxidation and reduction provide Li diffusion channels,[75,76] and the open ends of the graphene shell allow

electrolyte to penetrate into the graphene shell to electrochemically react with the Si nanoparticles inside the shell during charge/discharge (Figure 3.2 a). Clear SEM image of the open end structure is shown in Figure 3.2 d.

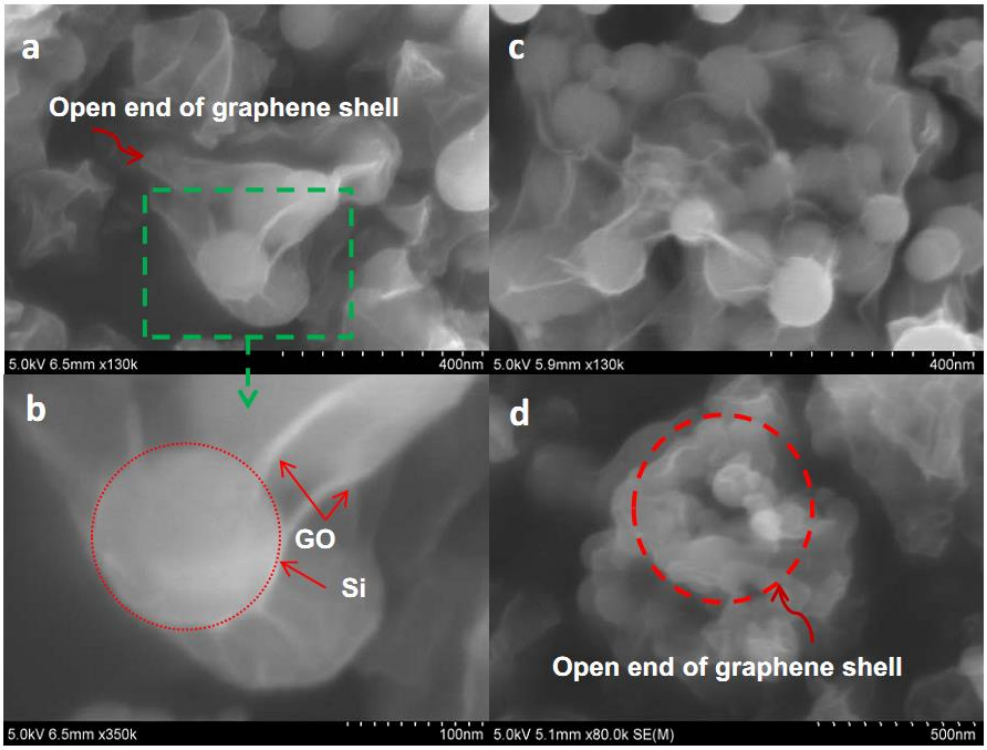

Figure 3.2 (a) SEM images of the APS-Si-G composite; and (b) the magnified view of the green square in (a), and (c) SEM image of unfunctionlized Si-G composite. (d) SEM image of APS-Si-G showing the open end structure of graphene shell (maked by red circle).

To further study the morphology of the material, Transmission Electron Microscopy (TEM) was used to analyze the material. Figure 3.3 a shows the TEM image of a single graphene capsule. Limit number (~10) of Si nanoparticles are wrapped in the graphene shell. The Si particles are separated from each other and there are large

space among the particles. The magnified view of the spot in blue square is given in Figure 3.3 b. The zoom in image identifies clear graphene layer on the surface of Si particles, confirming encapsulation. The high resolution TEM (HRTEM) image (Figure 3.3 c) provides clear view of fine Si lattice, silica layer and graphene shell. The thickness of silica layer is around 7 nm in thick.The graphene capsule is in multiple layers (~11 layers) with a thickness of about 8 nm.

TEM bright field image and Energy Dispersive X-ray Spectrospcopy (EDS) images were also using to probe the material structure and elemental distribution information. TEM bright field image (Figure 3.3 d) shows good dispersion of Si nanoparticles. EDS analysis was acquired on the same capsule to get the elemental distribution information. The element mapping (Figure 3.3, e and f) demonstrated uniform distribution of Si and C elements. Elemental map for Si (Figure 3.3 e, highlighted in red) shows distinct Si nanoparticles, implying good Si dispersion with large free space within the graphene shell.

The composition of APS-Si-G sample was determined using thermo gravimetric analysis (TGA). Figure 3.4 a shows the TGA curve of APS-Si-G sample. The 28% of mass loss below 500 °C corresponds to the oxidation of graphene in the sample. Si particles are stable up to 600 °C. The gradually regained mass above 600 °C is attributed to oxidation of the the Si core. The overall percentage of Si in APS-Si-G sample is determined to be 72 wt%. Given the fact that the original mixture was prepared in 1:1 mass ratio, it seems that the graphene species suffer from comparatively more significant mass loss during the pyrolysis procedure. This could

be due to the oxygen-containing species removal during reduction and the defects/edges etching effects occurs during aerosol spray. [77-79]

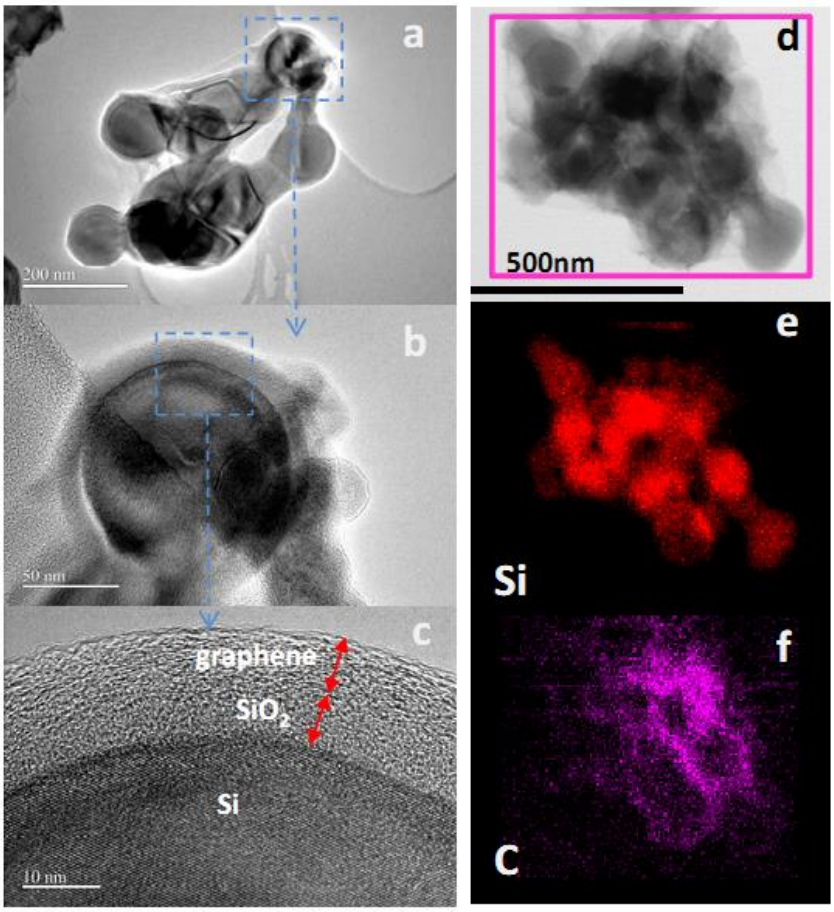

Figure 3.3 (a) TEM image of APS-Si-G, (b) The magnified view of the spot in blue square, and (c) HRTEM image of sample edge. (d) Bright field TEM image of APS-Si-G. (e) EDS elemental mapping for Si in (d). (f) EDS elemental mapping for C in (d).

The bonding effect between the Si and graphene shell was characterized by using Fourier transform infrared spectroscopy (FTIR). Figure 3.4 b shows FTIR spectra for

APS-Si, GO and APS-Si-G composites. In the FTIR of GO, the O-H (broad coupling ν O-H) at ~3200 cm^{-1} and the carbonyl stretch (ν C=O) at ~1700 cm^{-1} are generated by the carboxylic group on the surface of GO. This data is consistent with the reported GO FTIR curve.[80,81] In the APS-Si spectrum, the existence of amino groups is evidenced by the NH_2 stretch (ν NH_2) at ~3000cm^{-1}, the –NH_2 absorption (δ NH_2) at ~1600cm^{-1} and the characteristic peaks of amino groups (ɣ NH_2) at 900 cm^{-1}~650 cm^{-1}, which demonstrates well functionalization of Si. The O-H peak (broad coupling ν O-H) centered at ~3200 cm^{-1}, existing in GO, disappears in the APS-Si-G sample, which indicates bonds formation between two components. For the FTIR spectrum of APS-Si-G samples, new peak appearing at ~3600 cm^{-1} is resulted from the N-H stretch (ν N-H) and the sharp doublet at ~3000 cm^{-1} is generated by the N-H stretch overtone. C=O (ν C=O) peak at ~1700 cm^{-1} and C=N (ν C=N) peak at ~1450 cm^{-1} are also evidence of formation of amide groups.

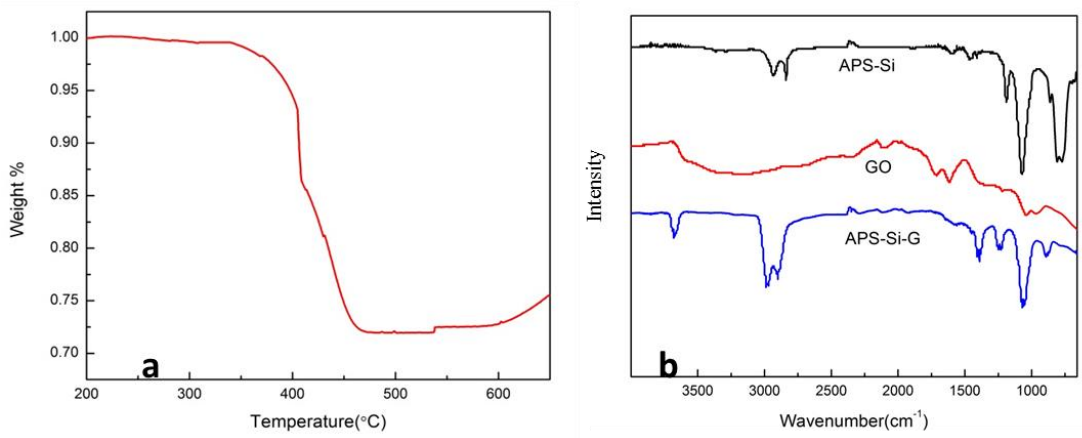

Figure 3.4 (a) TGA curve of APS-Si-G sample, and (b) FTIR transmittance spectra of APS-Si, GO, and APS-Si-G composite

3.3.2 Electrochemical Performance

The first three lithiation/delithiation cycling behavior of the APS-Si-G sample were characterized using cyclic voltammetry (CV) as shown in Figure 3.5 a. The broad peak between 1.7 V and 0.5 V (vs. Li/Li^+) in the first cathodic scan is attributed to the formation of solid electrolyte interphase (SEI) film on graphene and Si. SEI film formation leads to irreversible capacity and low coulombic efficiency of the first cycle. [82,83] The peaks at 0.2 V and 0.05 V showing in the second and third cathodic sweeps correspond to lithium insertion to form different phases of Li-Si alloy. Peaks showing in the anodic sweep at 0.3 V and 0.5 V are attributed to the delithiation of Li-Si alloy. This figure exhibits the typical Si lithiation/delithiation behavior and is consistent with reported CV curves for Si-carbon composite. [84,85]

The cycling stability of APS-Si-G and Si-G samples during charge/discharge between 0.002 V-1.5 V (vs. Li/Li^+) at 500mA g^{-1} is shown in Figure 3.5 b. All the specific capacity is calculated based on the total mass of Si and graphene. Capacity of Si-G without APS decreased quickly from initially 1000 mAh g^{-1} to 160 mAh g^{-1} after 100 cycles. This is due to the disconnection between graphene and Si nanoparticles and the inter-particle crush effect caused by volume expansion/shrinkage. Since the Si particles inside graphene are aggregated and no bonds between the two components exist, the large volume change may affect the structure stability and cause detachment of Si from graphene, resulting in disconnection to the current collector. Different from the Si-G sample, the APS-Si-G sample contains bonds between Si and graphene and larger void space between Si nanoparticles in each graphene shell. This unique

morphology greatly improves the structure stability, thus contribute to superior cycling stability.

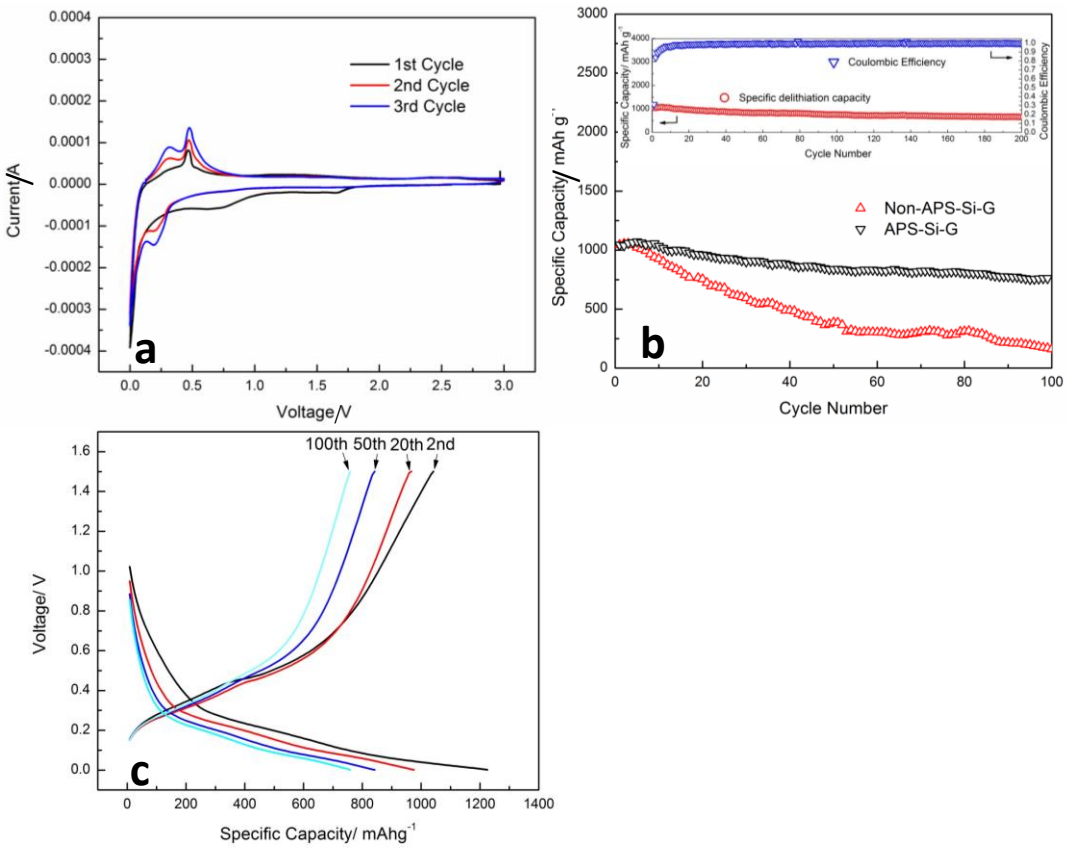

Figure 3.5 (a) Cyclic voltammetry curve of APS-Si-G composite at scan rate of 0.1 mV s^{-1}. (b) Capacity stability of APS-Si-G and Si-G composites; (c) Charge/discharge curves of APS-Si-G composite.

The capacity of APS-Si-G retains a specific charge capacity of 760mAh g^{-1} after 100 cycles and 656 mAh g^{-1} even after 200 cycles which reveal the superior cycling ability (inset of Figure 3.5 b). The coulombic efficiency of ASP-Si-G reaches around 100% after 15 cycles and remains stable during the subsequent charge-discharge

cycles. Figure 3.5 c shows the charge/discharge curves for the APS-Si-G sample at the 2^{nd} cycle, 20^{th} cycle, 50^{th} cycle and 100^{th} cycle, respectively. The plateaus appearing at 0.1 V and 0.2 V during the discharge process and at 0.4 V on the charge process correspond to Li-Si alloy and dealloy processes.

SEM images of APS-Si-G after 100 charge/discharge cycles are provided in Figure 3.6. Images show good graphene encapsulated Si structure, demonstrating good structure retention after cycles.

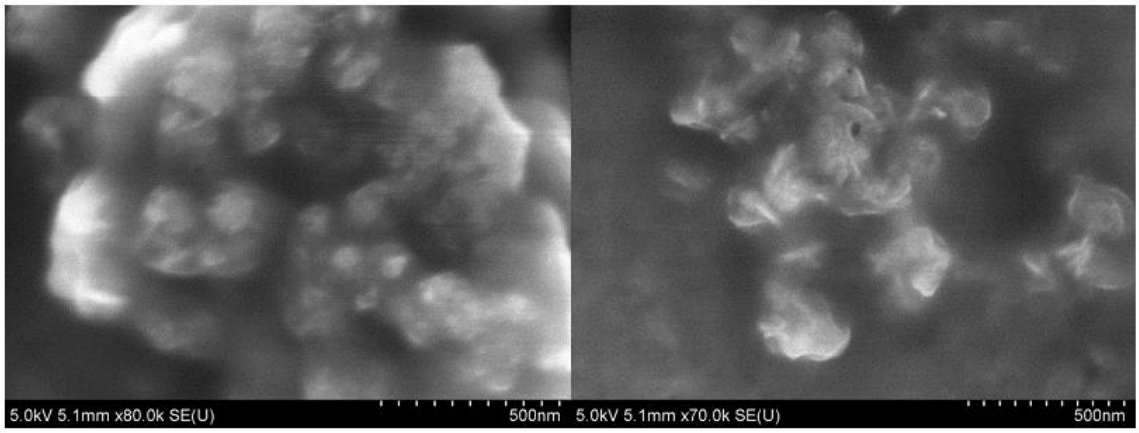

Figure 3.6 SEM images of APS-Si-G after 100 charge/discharge cycles at a current density of 500 mA g^{-1}.

The capacity contributed by Si in APS-Si-G composite was calculated by extracting the capacity of graphene measured at the same current. The specific capacity of graphene at 500 mA g^{-1} charging/discharging rate is 180 mAh g^{-1}. For an initial capacity of ~1000 mAh g^{-1} for the APS-Si-G sample, the capacity of Si is around 1318 mAh g^{-1}, which is much lower than theoretical capacity of 3589 mAh g^{-1}. The low utilization of Si may be attributed to insufficient binding of ASP-Si-G particles to ASP-Si-G particles and ASP-Si-G particles to current collector. To further increase

the utilization of Si nanoparticles in APS-Si-G sample, sodium alginate (SA) was used as an alternative binder. Carboxymethylcellulose (CMC) (Figure 3.7a) is a chain-like polymer with hydropholic polysaccharide backbone and large amount of hydrophilic carboxylic groups attached to the backbone.[86] CMC is one of the most widely used water soluble binder in LIB engineering. Recently, sharing the similar chain structure with abundant of carboxylic groups, sodium alginate (SA) (Figure 3.7b)[87] is reported to be a superior binder. It has been revealed that SA can provide more uniform binder coverage than CMC binder due to higher concentration and more uniform distribution of carboxylic groups. Besides, SA can also stabilize SEI film and provide fast Li ion transport. [88]

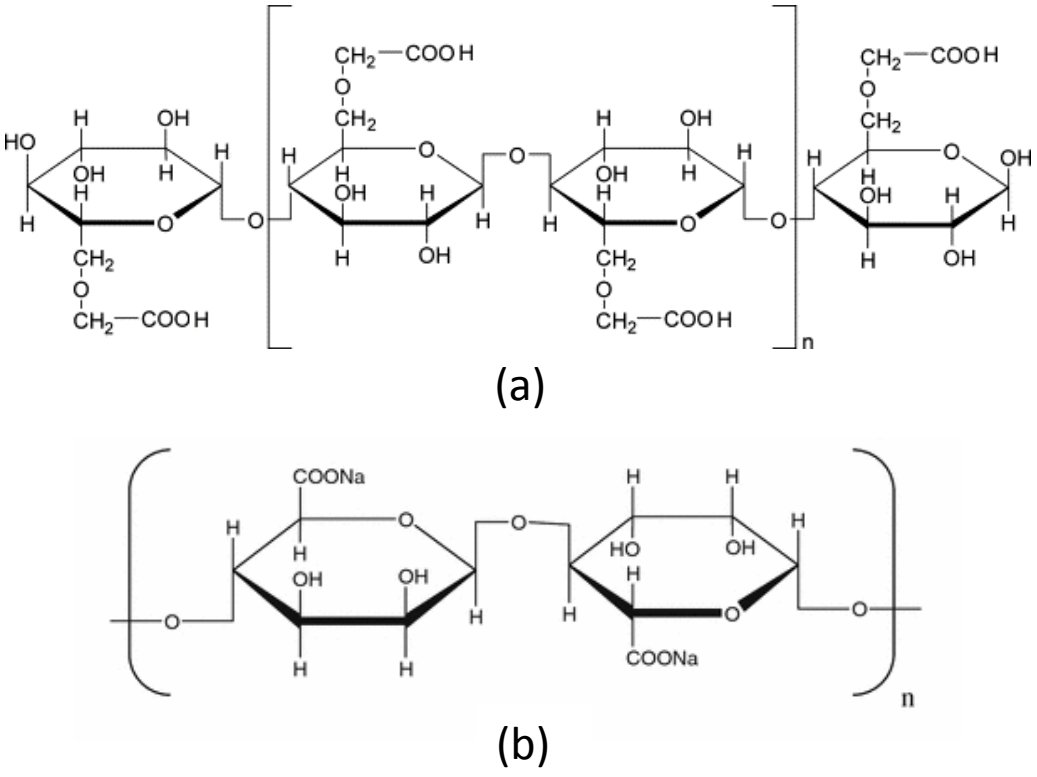

Figure 3.7 Molecular Structure of (a) CMC and (b) SA[87].

Figure 3.8 a shows the comparison of cycling stability for APS-Si-G sample using CMC and SA binders. Although the APS-Si-G samples show sustainable cycling stability with both CMC and SA binders, the utilization of Si in the APS-Si-G sample with SA binder is much higher than that with CMC binder. As shown in Figure 4a, the APS-Si-G sample with SA binder can deliver a specific charge capacity above 1800 mAh g^{-1} with the above 2422 mAh g^{-1} on Si, which is much higher than the APS-Si-G sample with CMC binder. For the APS-Si-G sample with SA binder, a specific charge capacity of 1500 mAh g^{-1} can be achieved even after 120 full charge-discharge cycles. Also, the 1^{st} cycle coulombic efficiency for the APS-Si-G sample with SA binder is 60% which is much higher than the sample with CMC binder (~30%). Moreover, compared to the slow activation process of the APS-Si-G sample with CMC, the coulombic efficiency for APS-Si-G with SA binder quickly reached 100% after first 5cycles.

Figure 3.8 b compares the rate capability of the APS-Si-G sample using CMC and SA binders. APS-Si-G sample with CMC binder shows good rate capability up to 8C while the APS-Si-G with SA binder shows superior performance up to 12C. The strong mechanical strength of graphene shells ensures electronic conductivity of Si nanoparticles when undergoing volume expansion and contraction. At the same time, the open ends of graphene shells ensure the sufficient transfer of lithium ions even at high C rates. In Figure 4b, the capacity retains ~84% at 1C, 50% at 8C as in 0.1C in sample with SA binder, while retention for sample with CMC binder is 76% at 1C and 44% at 8C. The sample with SA binder cycled at high rate (12C) provides similar capacity (700 mAh g^{-1} based on total mass) as that of the sample with CMC at a

comparatively low charging/discharging rate (4C), demonstrating that SA binder enhanced the performance of APS-Si-G anode sample.

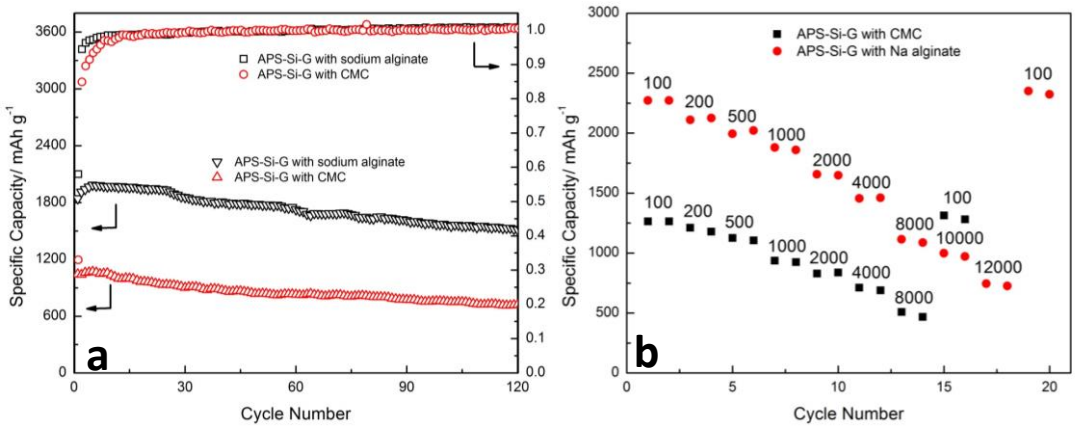

Figure 3.8 (a) Capacity stability of the APS-Si-G composite during charge/discharge cycles at 1C using CMC binder and Na alginate binder. (b) Rate capability of the APS-Si-G composite using CMC binder and Na alginate binder (labeled with current density in mA g^{-1}).

The great improvement of electrochemical performance by SA binder could be attributed to the high concentration of carboxylic groups in SA. It was reported that the ester-like bond resulting from reaction between hydroxyl groups on the active material and carboxylic groups in the binder was one of the most important factors for stabilizing the Si composite anode. [89,90] Since GO carries a large amount of OH groups on the surface, high concentration of COOH groups in SA would have more opportunity to generate ester-like bonds between binder and GO shells, thus providing better interaction within the electrode. The mophorlogy of APS-Si-G with

SA binder is highly favored in Si composite anode, since the bonding between graphene and Si ensures sufficient conductivity when Si undergoes the lithiation/delithiation process, and at the same time, SA will improve the conductivity between graphene shells and current collector to enhance the utilization of active material.

3.4 Summary

In summary, we have successfully synthesized the graphene –bonded and encapsulated material for LIB anode. Blending in graphene allow better conductivity of material and promote the cycling ability of Si anode. The APS-Si-G anode reveals superior cycle life with good capacity retention. A further improvement was achieved by utilizing SA binder.

3.5 Related References

58 Armand, M. & Tarascon, J. M. Building better batteries. *Nature* 451, 652-657 (2008).

65 Chen, J. & Cheng, F. Combination of Lightweight Elements and Nanostructured Materials for Batteries. *Acc. Chem. Res.* 42, 713-723 (2009).

66 Goodenough, J. B., & Kim, Y. Challenges for Rechargeable Li Batteries. *Chem. Mater.* 22, 587-603 (2010).

67 Li, H., Wang, Z., Chen, L. & Huang, X. Research on Advanced Materials for Li-ion Batteries. *Adv.Mater.* 21, 4593–4607 (2009).

68 Poizot, P., Laruell, S., Grugeon, S., Dupont, L. & Tarascon, J.-M. Searching for new anode materials for the Li-ion technology: time to deviate from the usual path. *J. Power Sources* 97-98, 235-239 (2001).

69 Liu, H. K., Guo, Z. P., Wang, J. Z., & Konstantinov, K. Si-based anode materials for lithium rechargeable batteries. *J. Mater. Chem.* 20, 10055-10057 (2010).

70 Chou, S. L., Wang, J. Z., Choucair, M., Liu, H. K., Stride, J. A., & Dou, S. X. Enhanced reversible lithium storage in a nanosize silicon/graphene composite. *Electrochem. Commun.* 12, 303-306 (2010).

71 Lee, J. K., Smith, K. B., Hayner, C. M. & Kung, H. H. Silicon nanoparticles–graphene paper composites for Li ion battery anodes. *Chem. Commun.* 46, 2025-2027 (2010).

72 Tao, H.-C., Fan, L.-Z., Mei, Y. & Qu, X. Self-supporting Si/Reduced Graphene Oxide nanocomposite films as anode for lithium ion batteries. *Electrochem. Commun.* 13, 1332-1335 (2011).

73 Zhao, X., Hayner, C. M., Kung, M. C. & Kung, H. H. In-Plane Vacancy-Enabled High-Power Si–Graphene Composite Electrode for Lithium-Ion Batteries. *Adv. Energy Mater.* 1, 1079-1084 (2011).

74 Luo, J., Zhao, X., Wu, J.-S., Jang, H. D., Kung, H. H. & Huang, J. Crumpled Graphene-Encapsulated Si Nanoparticles for Lithium Ion Battery Anodes. *J. Phys. Chem. Lett.* (2012).

75 Gómez-Navarro, C., et al. Atomic Structure of Reduced Graphene Oxide. *Nano Lett.* 10, 1144-1148 (2010).

76 Erickson, K., Erni, R., Lee, Z., Alem, N., Gannett, W., & Zettl, A. Determination of the Local Chemical Structure of Graphene Oxide and Reduced Graphene Oxide. *Adv. Mater.* 22, 4467-4472 (2010).

77 Ma, X., Zachariah, M. R. & Zangmeister, C. D. Crumpled nanopaper from graphene oxide. *Nano lett.* 12, 486-489 (2011).

78 Zangmeister, C. D., Ma, X. & Zachariah, M. R. Restructuring of graphene oxide sheets into monodisperse nanospheres. *Chem. Mater.* 24, 2554-2557 (2012).

79 Ma, X., Zachariah, M. R. & Zangmeister, C. D. Reduction of suspended graphene oxide single sheet nanopaper: the effect of crumpling. *J. Phys. Chem. C* 117, 3185-3191 (2013).

80 Si, Y. & Samulski, E. T. Synthesis of Water Soluble Graphene. *Nano Lett.* 8, 1679-1682 (2008).

81 Guo, H.-L., Wang, X.-F., Qian, Q.-Y., Wang, F.-B. & Xia, X.-H. A Green Appraoch to the Synthesis of Graphene Nanosheets. *ACS Nano* 3, 2653-2659 (2009).

82 Lee, Y. M., Lee, J. Y., Shim, H.-T., Lee, J. K. & Park, J,-K. SEI Layer Formation on Amorphous Si Thin Electrode during Precycling. *J. Electrochem. Soc.* 154, A515-A519 (2007).

83 McArthur, M. A., Trussler, S. & Dahn, J. R. In Situ Investigations of SEI Layer Growth on Electrode Materials for Lithium-Ion Batteries Using Spectroscopic Ellipsometry. *J. Electrochem. Soc.* 159, A198-A207 (2012).

84 Zhou, X., Yin, Y.-X., Wan, L.-J. & Guo, Y.-G. Facile synthesis of silicon nanoparticles inserted into graphene sheets as improved anode materials for lithium-ion batteries. *Chem. Commun.* 48, 2198-2200 (2012).

85 Wang, W. & Kumta, P. N. Nanostructured Hybrid Silicon/Carbon Nanotube Heterostructures: Reversible High-Capacity Lithium-Ion Anodes. *ACS Nano* 4, 2233-2241 (2010).

86 Su, J.-F., Huang, Z., Yuan, X.-Y., Wang, X.-Y. & Li, M. Structure and properties of carboxymethyl cellulose/soy protein isolate blend edible films crosslinked by Maillard reactions. *Carbohydr. Polym.* 79, 145-153 (2010).

87 Ichiura, H., Kaneda, Y. & Ohtani, Y. Functional geraniol-Ca (OH) 2 composite/sodium acetate alginate film on nonwoven polyethylene sheet: acetic acid gas production in response to acid. *J. Mater. Sci.* 45, 1343-1349 (2010).

88 Kovalenko, I., *et al*. A Major Constituent of Brown Algae for Use in High-Capacity Li-Ion Batteries. *Science* 334, 75-79 (2011).

89 Bridel, J. S., Azais, T., Morcrette, M., Tarascon, J. M. & Larcher, D. Key Parameters Governing the Reversibility of Si/Carbon/CMC Electrodes for Li-Ion Batteries. *Chem. Mater.* 22, 1229-1241 (2009).

90 Mazouzi, D., Lestriez,, B., Roué, L. & Guyomard, D. Silicon Composite Electrode with High Capacity and Long Cycle Life. *Electrochem. Solid-State Lett.* 12, A215-A218 (2009).

Chapter 4: Carbon Nanotubes-bonded and –Entangled Si Nanoparticles Composite as Anode for Li-ion Batteries

4.1 Introduction

Lithium-ion battery (LIB) is one of the most important rechargeable energy storage devices in portable electronic components and hybrid vehicles. The study to improve anode material performance, especially cycling stability and capacity, has been active for the past decades. [91-96] Silicon, with a high theoretical capacity of ~3600mAh g^{-1} that is a magnitude higher than that of current commercial LIB anode, is considered to be next generation anode material for advanced Li-ion batteries. However, it is well known that there is ~270% of the volumetric change during Si anode cycling, which would directly cause active material crumbling, conduction network failure and lead to capacity decay. It was proved that, using nano-size Si material will effectively prevent active material from pulverization.[97] However, the interruption of conduction network resulted from volumetric change remains unsolved.

A main approach to solve the problem is to blend in conductive material and to use composites instead of pure silicon. Among all the conductive additive material, carbon material was superior. Carbon material is low cost and it exists in various forms that can be easily handled. Moreover, most of the carbon materials, such as graphite, mesophase microbeads (MCMB) and pitch, are active to Li, they contribute to overall capacity while it is functional as structure material. In the past, various contempt of making well-dispersed Si in carbon host matrix was made.[96,98-100] And it was proved that carbon host can, to some extent, sufficiently buffer the volume

change, stabilize the Si anode and improve the cycling stability. However, in all the fore-mentioned cases, since Si particles and carbon materials were prepared separately and then mixed up by various methods, there is no sufficient interaction in the Si-carbon interface. As the composite go through electrochemical cycling, continuous volumetric change would crack the Si-carbon interaction; resulting in breakage and capacity fading. In the last chapter, graphene-encapsulated Si composites were synthesized and studied as anode material for LIB.

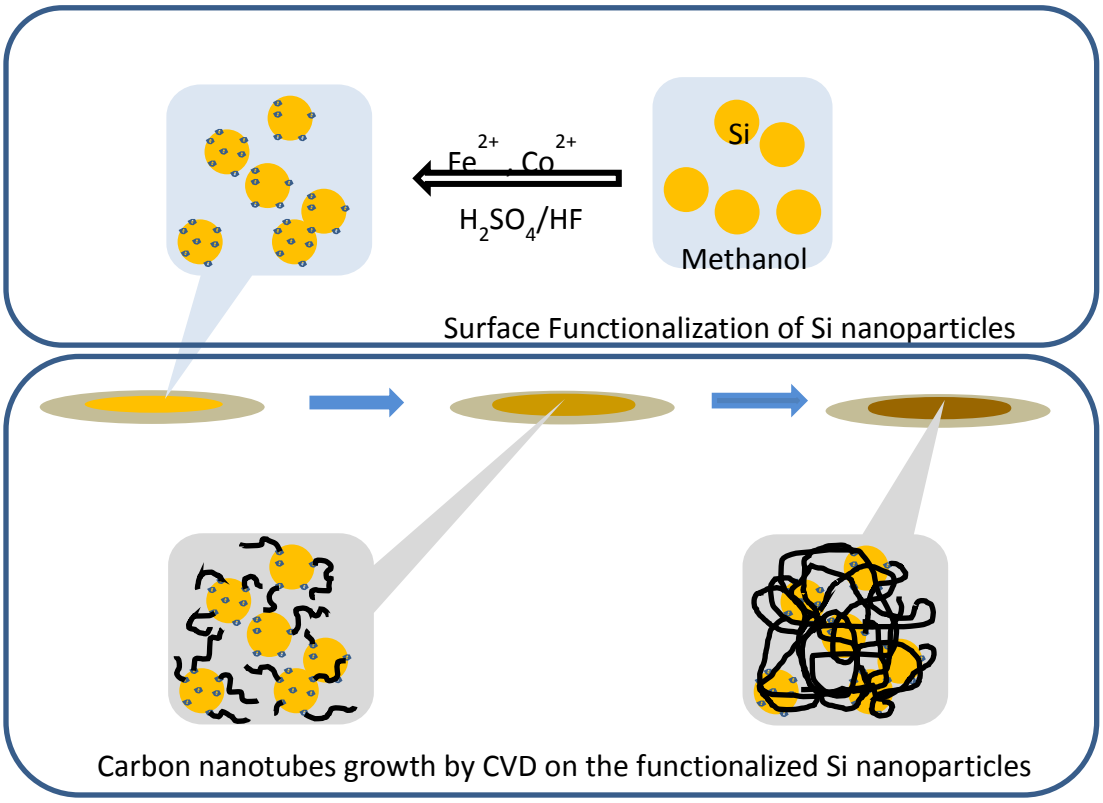

Figure 4.1 Schematic procedures for the synthesis of carbon nanotubes bonded- and entangled- nano-Si composite.

The encapsulation morphology was proved to be capable of successfully buffering the volume change and improve the stability along cycling. In this chapter, we further seek for methodology to enhance the interaction between Si and carbon matrix. In this

synthesis path, instead of mixing of the two parties, Si and carbon materials, the carbon matrix consists of carbon nanotubes nets was instantaneously grown on the well dispersed functionalized Si, to form carbon nanotubes –bonded and –entangles Si nanoparticals structured composites(Figure 4.1). The strong interaction delivered through carbon-metal-Si bonds ensures the superior electronic conductivity through cycling. More importantly, the direct connection between carbon nanotubes and Si particles will prevent active material (Si) from disconnecting to the current collector through cycling. The carbon nanotubes nest was proved to be capable to provide sufficient buffer and conductivity to Si.

4. 2 Experimental Sections

4.2.1 Si nanoparticle functionalization and carbon nanotubes growth

The Si nanoparticle surface functionalization was inspired by the metal-polysilicate complex synthesis technique that has been widely used in water treatment.[101] The reaction occurs between naturally found silica layer on the Si nanoparticle surface and the Fe^{2+} /Co^{2+} reagent. Thus the amount of silica layer on the Si nanoparticle surface would have significant influence on the surface functionalization reaction.

Both commercial Si nanoparticles and homemade Si nanoparticles were used in the experiment. The homemade Si was synthesized from reducing SiO_2 nanoparticles by magnesium. In a typical process, SiO_2 nanoparticles were mixed with Mg in a stoichiometric ratio as in the equation (4.1).

$$2Mg(S) + SiO_2(S) \rightarrow 2MgO(S) + Si(S) \qquad (4.1)$$

The mixture was prepared in the glove box filled with Ar to ensure there is no oxygen in the system. Then the mixture was heated up to 625^{o}C under argon atmosphere to trigger the reaction. The product was collected in powder format. Si particles were collected by washing out the MgO in the product by HCl. The Si ratio in the homemade Si was determined to be 65% while the oxygen element is 35%.

In a surface functionalization process, Si particles were pre-oxidized by strong acid or used as-is. In the oxidization reaction, Si nanoparticles were treated with H_2SO_4/HF (1:1 in volumetric ratio) solution for 30 min in room temperature to get surface oxidized before functionalization. Then, the oxidized Si nanoparticles were carefully filtered out by vacuum filtration and washed with DI water till neutral.

The treated or raw Si nanoparticles were dispersed in methanol by continuously stirring, surface functionalization reagent, $FeSO_4$ (2% in molar ratio) and $CoSO_4$ (2% in molar ratio) were added into the solution for reaction. The mixture was then continuing stirred for 1 hour to ensure the occurring of reaction. After surface functionalization, the mixture solution was loaded into surface dish, where the MeOH will be removed by evaporation. Using Fe^{2+}/Co^{2+} catalyst system is to better control the uniformly CNT growth. Potential problem is that Co could toxic if accumulated.

The loaded substrate was then transferred into a tube furnace with a quartz tube in 3 inch inner diameter for chemical vapor deposition (CVD) reaction. The whole tube furnace was set to 200°C to warm up prior to the reaction. And the whole system firstly quenched with N_2 for three times before CH_2 was introduced to the system. In the second step, the temperature was raised to 700^{o}C. The CH_2 was then introduced to the system as carbon source. The flow rate was controlled at a volumetric flow rate of

10L min^{-1} for all experiments. Various carbonization time was set to achieve different carbon nanotubes loading. The resulted powder material was collected for further morphology characterization and electrode preparation.

4.2.2 Material characterization

The morphology of the resulted carbon nanotubes-entangled Si(CNT-Si) was characterized by scanning electron microscopy (SEM) and transmission electron microscopy(TEM) in the University of Maryland Nanocenter. The ratio of carbon nanotubes in the composite was determined by thermogravimetric analysis (TGA). Powder sample was loaded into the TGA equipment (CAHN TG 2131, USA) with control bucket. The sample was heated from room temperature to 800 °C in air atmosphere at a heating rate of 10°C per min.

4.2.3 Electrochemical characterization

Electrochemical testing CNT-Si electrodes were prepared by the slurry coating method. The active material was mixed with 10 wt% binder (sodium alginate) and 10wt% of carbon black, and milled for 30 minutes to form slurry. Then, the obtained slurry was cast on copper foil and dried in a vacuum oven at 100 °C overnight. The loading amount of active material was ~ 0.5mg cm^{-2}. The loaded current collector was cut into a round dish with ~1cm in diameter before assembled into coin cell. A typical coin cells consists of a CNT-Si working electrode, a lithium metal counter electrode, Celgard 3501 separator, and 1.0 M $LiPF_6$ in dimethyl carbonate (DMC): fluoroethylene carbonate (FEC) (1:1) co-solvent liquid electrolyte. The whole

assembling process was carried out in an argon-filled glove box for electrochemical tests.

Galvanostatic charge/discharge was performed using an Arbin test station. Cells were cycled between 0.002 V and 1.5 V at different currents. After the cell reached the cut off voltages, it was relaxed for 10 mins before subsequent charge or discharge. Cyclic voltammetry (CV) test with voltage ranging from 0 V to 3 V was performed at a scan rate of 0.1 mV s^{-1} using a Solatron 1260/1287 Electrochemical Interface (Solatron Metrology, UK).

For the rate capability tests, cells were pre-cycled for 10 cycles for activation and then charged-discharged at various C rates between 0.002 V and 1.5 V. The capacity is calculated based on the overall mass of CNT-Si composites.

4.3 Result and Discussion

4.3.1 Material Characterization

CNT-Si fabricated with different CNT growth time (8min and 10 min, respectively; denoted as CNT-Si-8 and CNT-Si-10) and pre-oxidized Si (with 10min carbonization time, denoted as CNT-Si-10-O), were characterized with scanning electron microscopy (SEM) for morphology.

Figure 4.2 shows the SEM images of CNT-Si-8 composite. In the low magnification image (Figure 4.2 a), the composite shows a compacted bulk particle in micro scale, indicating that the carbon nanotubes were tangle the Si nanoparticles tightly. The tightened bulky morphology would result in smaller surface area that expose directly to the electrolyte, thus reduce the first cycle irreversible capacity. In a higher magnified image (Figure 4.2 (b), (C) and (d)), a thin layer of CNT consisting of CNT

in diameter that < 10nm and various length, was observed on the Si bulk surface (Figure 4.2 (b) and (C)) and in between the Si nanoparticle group (Figure 4.2(d)). It is clearly viewed that, yet the Si groups were tightly tangled by CNT, there are significant amount of the space between the individual particles generated by CNT nest. The spacing would be a good buffer for volumetric change during cycling.

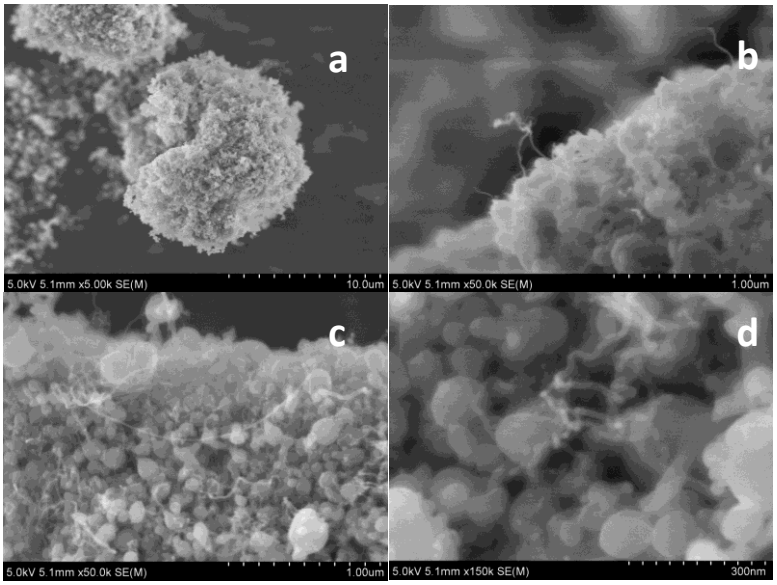

Figure 4.2 SEM images of the CNT-Si-8 composite in magnification of (a) 5k, (b) and (c) 50k, and (d) 150k.

Different CNT loading was achieved by manipulating the carbonization time. Figure 4.3 shows the SEM images of CNT-Si-10 composite. Similar tightened bulky structure was observed in the low magnification image (Figure 4.3 a). And the porous structure was also achieved with the bulk. In a higher magnified image (Figure 4.3

(b), (C) and (d)), we can see that, yet in around the same diameter, the CNTs are generally longer than that in CNT-Si-8 and appears more tangled morphology. More CNTs were found under the same magnification (Figure 4.3(d)), indicating that longer CNT growing time did promote the CNT mass.

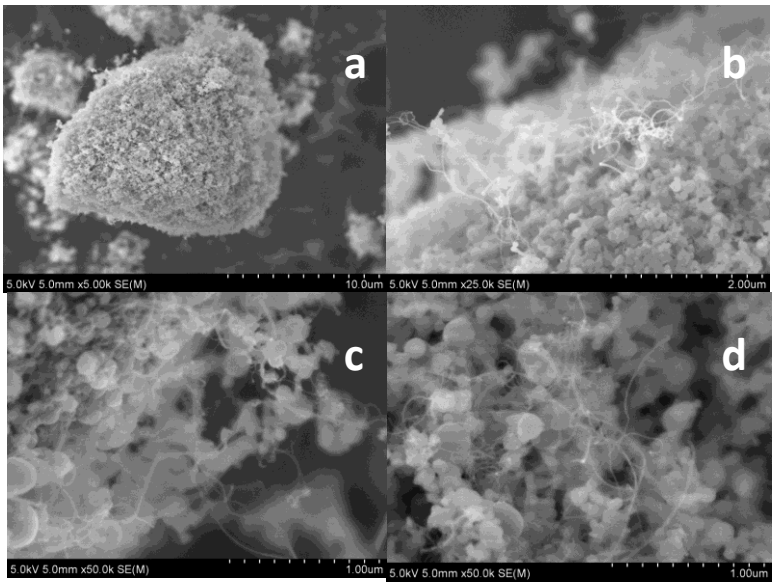

Figure 4.3 SEM images of the CNT-Si-10 composite in magnification of (a) 5k, (b) 25k, and (c) and (d) 50k.

When pre-oxidization process was performed, the surface SiO_2 layer gets thicker, and the functionalization becomes easier. In the CNT-Si-10-O (Figure 4.4), the CNT reveals much different morphology. Even though the same tightened micro scaled bulks were achieved (Figure 4.4 a), the CNTs show much larger diameter (Figure b and d) and shorter length (Figure c).

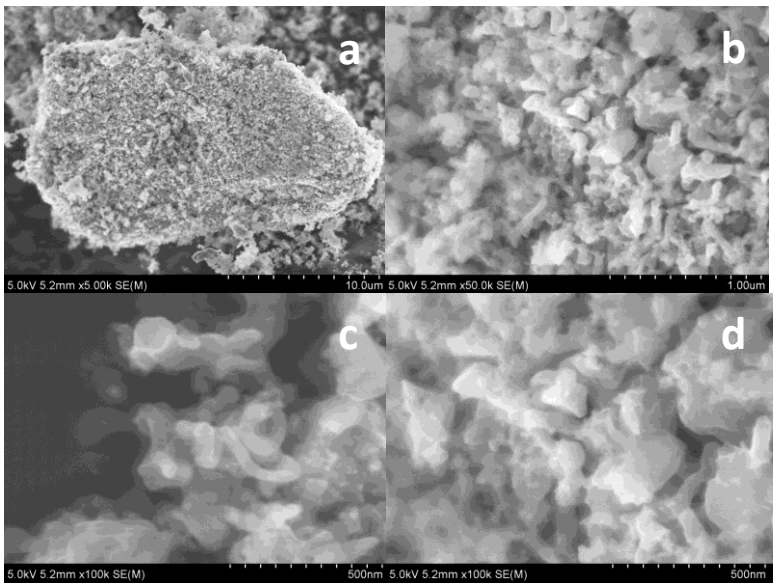

Figure 4.4 SEM images of the CNT-Si-10 composite in magnification of (a) 5k, (b) 50k, and (c) and (d) 100k.

To study the CNT growth mechanism, CNT-Si-8 was selected to do transmission electron microscopy (TEM) with EDS analysis. For TEM test, the powder sample was sonicated by horn sonicator to achieve well separation before testing. As shown in Figure 4.5, the CNT was directly grown on the Si particle surface. With the EDS elemental analysis, we can see that the metal catalyst (Fe, in this case) remains in the bottom of the CNT, function as a connection between Si particles and CNT. The Si-metal-C network would also benefit the electronic conductivity while cycling.

The composition of CNT-Si sample was determined using thermo gravimetric analysis (TGA) method. The TGA curves are shown in Figure 4.6. The overall percentage of carbon in CNT-Si-8, CNT-Si-10 and CNT-Si-10-O samples were determined to be 4 wt%, 8wt% and 12wt%, respectively. The ratio of conductive

carbon frame in the composites is significantly less than the reported Si-carbon anode,[102,103] revealing advantage of the in situ growth of CNT.

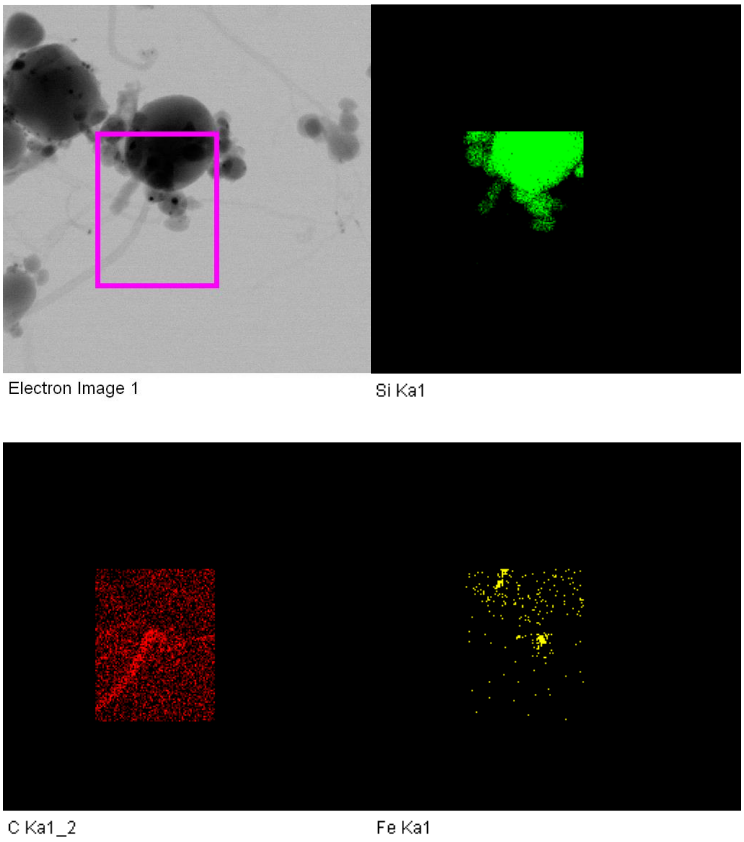

Figure 4.5 TEM images of the CNT-Si-8 with elemental mapping images.

The longer carbonization of CNT-Si-10 allow around as twice as the CNT growth on the surface than CNT-Si-8. CNT-Si-10 is expected to have better electronic conductivity.

The comparatively higher oxidation temperature of the Si core in CNT-Si-10-O (~650 ^{o}C) compared to that in CNT-Si-8 and CNT-Si-10 (~600 ^{o}C) is a side evidence of

significant thicker SiO_2 layer. The thicker layer of SiO_2 created by oxidation allows more active spots towards surface functionalization reaction, which directly yield to higher carbonization reaction yield. The amount of carbon nanotubes in CNT-Si-10-O is 4% higher than that in CNT-Si-10 even though they were carbonized under exactly the same condition.

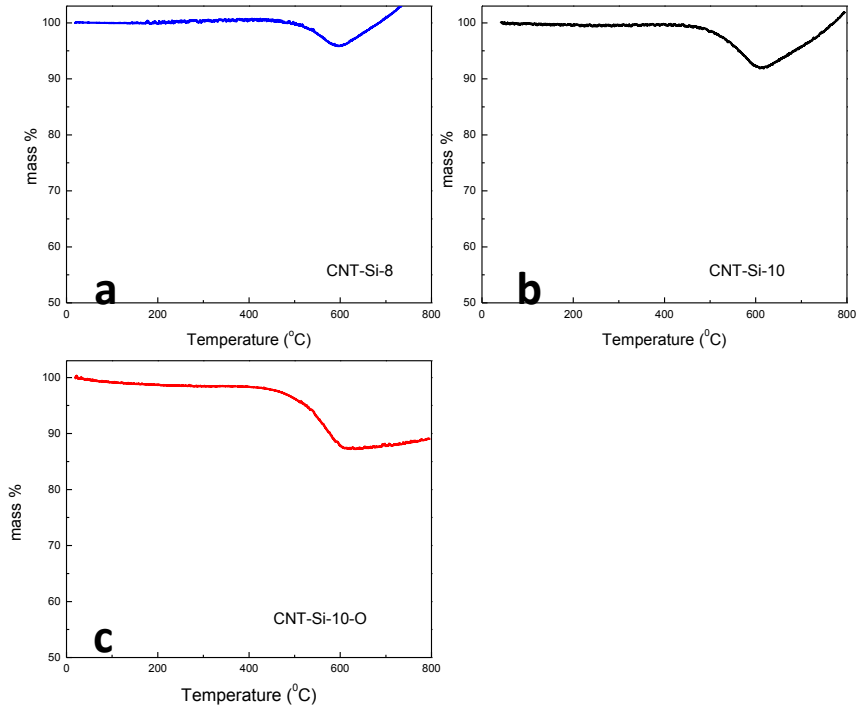

Figure 4.6 TGA curves of (a) CNT-Si-8, (b) CNT-Si-10 and (c) CBT-Si-10-O

4.3.2 Electrochemical Performance

The first five lithiation/delithiation cycling behavior of the CNT-Si samples were characterized using cyclic voltammetry (CV) as shown in Figure 4.7 All three samples share the similar CV pattern. This figure exhibits the typical Si lithiation/delithiation behavior and is consistent with reported CV curves for Si-carbon composite. [84,85] Compared to the precious CV study on grpahene-Si

composite, the disappearance of the broad peak between 1.7 V and 0.5 V (vs. Li/Li^+) in the first cathodic scan strongly indicated the significant decrease of the interphase between active composites and the electrolyte. The decreasing of formation of solid electrolyte interphase (SEI) film would improve the first cycle coulombic efficiency greatly. [82,83]

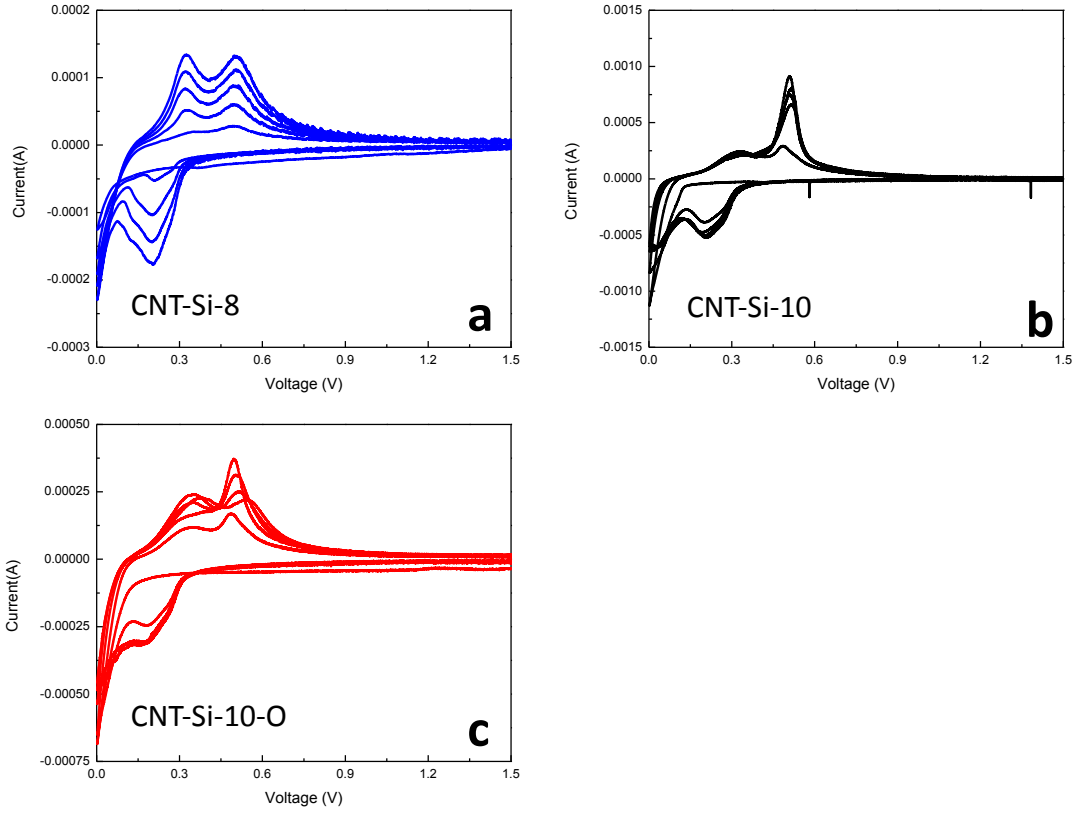

Figure 4.7 Cyclic voltammetry curve of (a) CNT-Si-8, (b) CNT-Si-10 and (c) CNT-Si-10-O composite at scan rate of 0.1 mV s^{-1}.

The peaks at 0.25 V and 0.1 V showing in cathodic sweeps correspond to lithium insertion to form different phases of Li-Si alloy. The existence of two peaks indicates that the CNT-Si composites adopt a two-step reaction to form fully lithiated state. Particularly, the cathodic peak at 0.25V is attributed to the formation of amorphous

alloys of Li_xSi ($0<x<3.75$), and the peak at ~0.1V is corresponding to the crystallization of $Li_{15}Si_4$. The curves are highly similar to the pure Si vs Li/Li^+,[101,104] suggesting low carbon loading in the composites, which is consistent with the TGA result. When going under delithiation process, the anodic curves are highly related to the lithiation status of the material. Generally speaking, the two Peaks showing in the anodic sweep at 0.3 V and 0.5 V are attributed to the delithiation of Li-Si alloy. The peak at 0.3V is attributed to the delithation from LixSi while the peak at 0.5V is related to the $Li_{15}Si_4$ de-alloy.[105] Notice that the anodic peak at 0.5V is more pronounced in CNT-Si-10 and CNT-Si-10-O than that in CNT-Si-8, indicating higher lithiated state in the CNT-Si-10. This could be related to more conductive network provide by higher CNT loading.

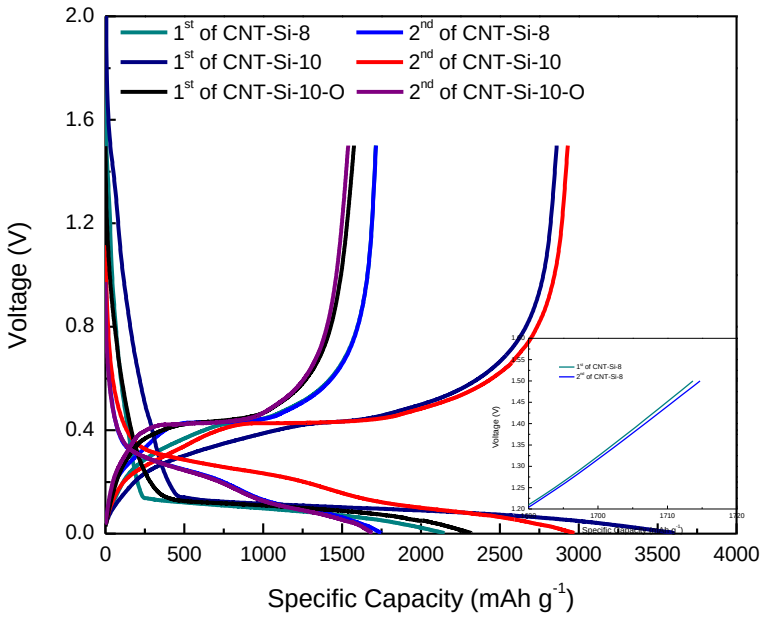

Figure 4.8 Charge/discharge curves of the initial first two cycles for CNT-Si-8, CNT-Si-10 and CNT-Si-10-O with current density of 100mA g^{-1}. The insert figure shows the zoom in image for CNT-Si-8.

Figure 4.8 shows the charge/discharge profiles of the CNT-Si species towards Li/Li^+ in the initial 2 cycles. All three samples reveal clearly long plateaus in the lithiation/delithiation process, which is consistent with the CV profile.

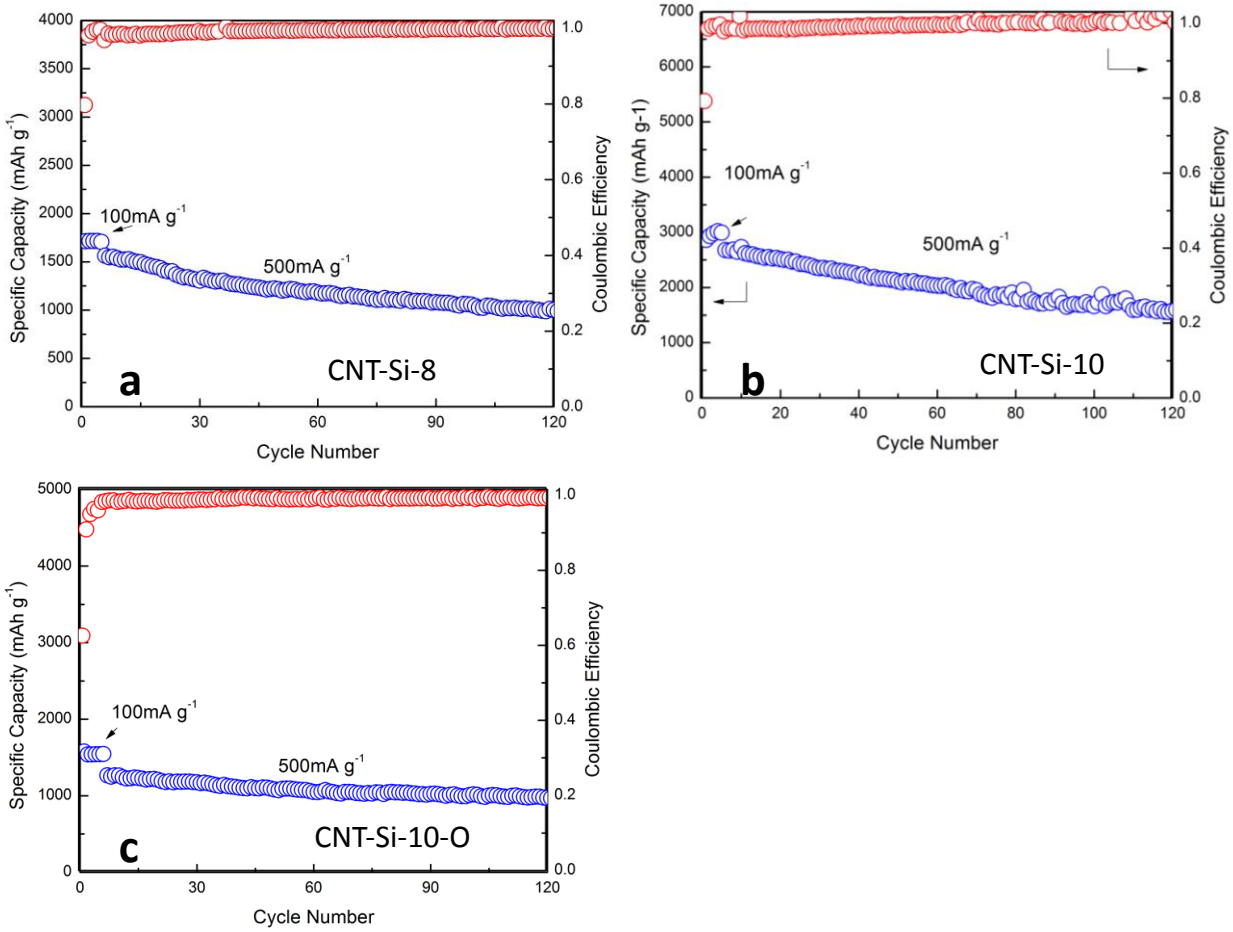

Figure 4.9 Cycling stability of (a) CNT-Si-8, (b) CNT-Si-10, and (c) CNT-Si-10-O

The cycling stability test profile between 0.002 V-1.5 V (vs. Li/Li^+) is shown in Figure 4.9. The cell was firstly cycle as current density of 100 mA g^{-1} for 5 cycles and then 500 mA g^{-1} for the rest cycles. All the specific capacities are calculated based on the total mass of Si and CNT. The CNT-Si-8 sample (Figure 4.9a) reveals a high

initial capacity of ~1700mAh g^{-1} at the first several cycles, and maintains a relatively high capacity after 120 cycles. The comparatively fast capacity decay could be due to insufficient CNT in the sample. Given the fact that the sample has only 4 wt% of CNT, the capacity indicates a utilization ratio on Si that is < 50%. This is also a side evidence shows that there is no sufficient conductive connecting within the bulk. The first cycle coulombic efficiency is ~80%, which is higher than the reported nano carbon-Si composite, suggesting that the carbon –entangled morphology successfully reduce the interphase that between composite and electrolyte.

The CNT-Si-10 sample (Figure 4.9b) shows higher initial capacity than CNT-Si-8, indicating the longer CNT growth time contributes to more CNT within the electrode. Similar high first cycle coulombic efficiency (~80%) was observed. However, the fast decay of the capacity indicates that the CNT network is still not strong enough to mechanically buffer the impact of volumetric change.

As shown in Figure 4.9 c, CNT-Si-10-O shows lower initial capacity (~62%) and slightly lower capacity than CNT-Si-10. The overall low capacity should be due to the oxidation process. Since SiO_2 contributes no capacity to the Li storage, the thicker SiO_2 layer in the material increases the "dead weight", leading to a lower overall capacity. On the other hand, the massive SiO_2 improve the CVD deposition yield of carbon nanotubes. The cycling stability of CNT-Si-10-O has been significantly improved. The CNT-Si-10-O retains 77% of the capacity of the original after 120 cycles, which is much higher than that in CNT-Si-10.

Since the CNT-Si-10-O shows the best capacity retention, it is chosen to proceed with further electrochemical characterization. Figure 4.10 shows the long term swiping of

CNT-Si-10-O. Good capacity retention (~50%) was achieved after 600 cycles. Around 25% of the capacity decay was occurring in the first 10 cycles. This could be due to the structure disturbing bring by volume change of initial lithiation and delithiation. From 200th to 600th cycle, the capacity lost is only ~0.05% per cycle.

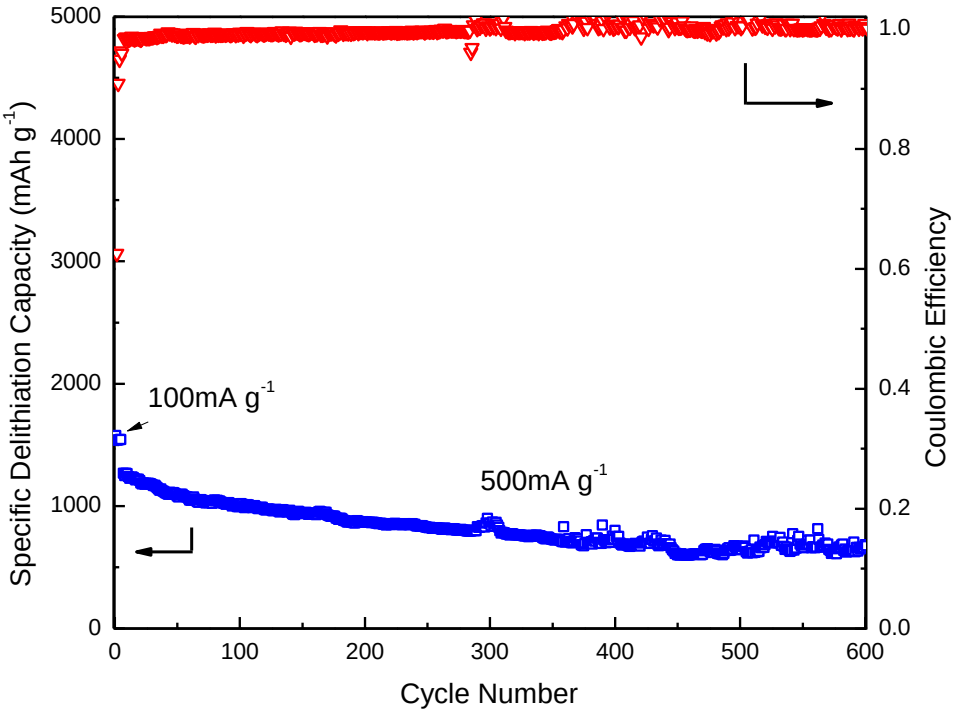

Figure 4.10 Long term cycling performance for CNT-Si-10-O

Rate capability performance was evaluated by cycling the CNT-Si-10-O Sample with different current density, range from 100mA g^{-1} to 10A g^{-1}. As shown in Figure 4.11, high capacity of ~570 mAh g^{-1} was achieved when the current density increased to 10A g^{-1}, indicating that the Si-metal-CNT bond and the CNT network provides good

electrical contact within the electrode material. Fast electron transport is feasible even at high charge/discharge rate.

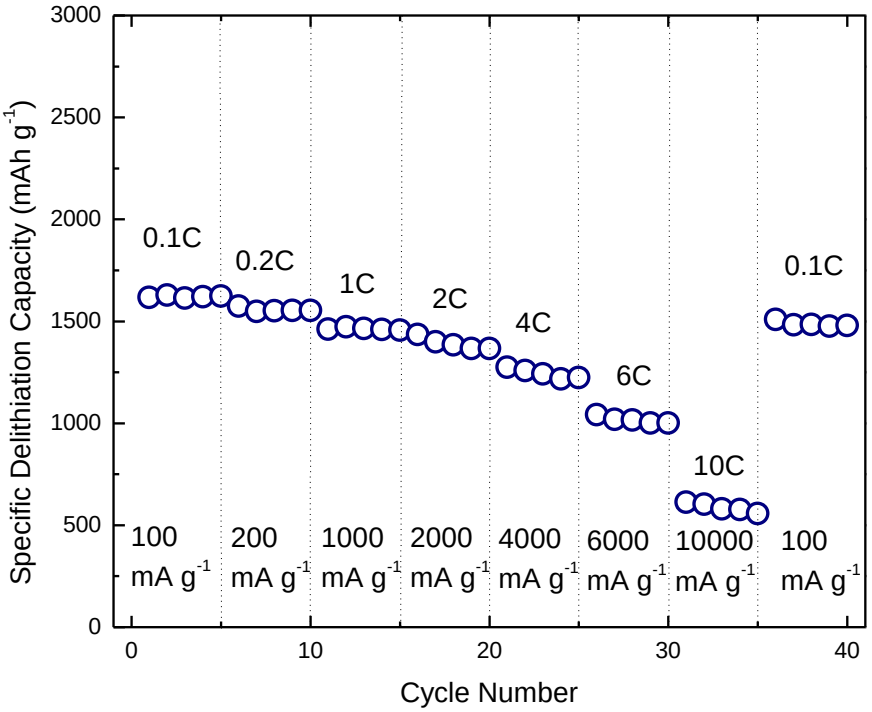

Figure 4.11 Rate capability performance for CNT-Si-10-O. The sample was pre-cycled for 10 cycles before test.

4.4 Summary

In summary, we have successfully synthesized the carbon nanotubes –bonded and –encapsulated Si composite. Different from traditional carbon-Si anode, the CNT-Si was fabricated by directly CVD growth of CNT on the functionalized Si. The CNT nest matrix was proved to be capable of sufficiently ensuring the conductivity and the metal-Si bonds were able to enhance the structure stability through long

electrochemical cycling. With significant lower carbon ratio than the reported work, the CNT-Si species can provide superior electrochemical performance as LIB anode, including: high initial coulombic efficiency of 60%-80%, superior rate capability with ~570mAh g^{-1} under high current density of 10A g^{-1}, and good capacity retention of ~50% after 600 cycles.

4.5 Related References

91 Shi, H., Barker, J., Saidi, M. & Koksbang, R. Structure and lithium intercalation properties of synthetic and natural graphite. *J. Electrochem. Soc.* 143, 3466-3472 (1996).

92 Idota, Y., Kubota, T., Matsufuji, A., Maekawa, Y. & Miyasaka, T. Tin-based amorphous oxide: a high-capacity lithium-ion-storage material. *Science* 276, 1395-1397 (1997).

93 Amezawa, K., Yamamoto, N., Tomii, Y. & Ito, Y. Single-Electrode Peltier Heats of Li-Si Alloy Electrodes in LiCl-KCl Eutectic Melt. *J. Electrochem. Soc.* 145, 1986-1993 (1998).

94 Mao, O. & Dahn, J. Mechanically Alloyed Sn-Fe (-C) Powders as Anode Materials for Li-Ion Batteries: II. The Sn-Fe System. *J. Electrochem. Soc.* 146, 414-422 (1999).

95 Endo, M. *et al.* Vapor-grown carbon fibers (VGCFs): basic properties and their battery applications. *Carbon* 39, 1287-1297 (2001).

96 Kim, I.-S., Blomgren, G. & Kumta, P. Nanostructured Si/TiB_2 composite anodes for Li-ion batteries. *Electrochem. solid-state lett.* 6, A157-A161 (2003).

97 Kim, H., Seo, M., Park, M. H. & Cho, J. A Critical Size of Silicon Nano-Anodes for Lithium Rechargeable Batteries. *Angew. Chem. Int. Ed.* 49, 2146-2149 (2010).

98 Zhang, X.-W. *et al.* Electrochemical performance of lithium ion battery, nano-silicon-based, disordered carbon composite anodes with different microstructures. *J. Power sources* 125, 206-213 (2004).

99 Dong, H., Feng, R., Ai, X., Cao, Y. & Yang, H. Structural and electrochemical characterization of Fe–Si/C composite anodes for Li-ion batteries synthesized by mechanical alloying. *Electrochim. acta* 49, 5217-5222 (2004).

100 Wolf, H., Pajkic, Z., Gerdes, T. & Willert-Porada, M. Carbon–fiber–silicon-nanocomposites for lithium-ion battery anodes by microwave plasma chemical vapor deposition. *J. Power Sources* 190, 157-161 (2009).

101 Fu, Y., Yu, S.-l., Yu, Y.-z., Qiu, L.-P. & Hui, B. Reaction mode between Si and Fe and evaluation of optimal species in poly-silicic-ferric coagulant. *J.Environ.Sci.* 19, 678-688 (2007).

102 Yoshio, M. *et al.* Carbon-coated Si as a lithium-ion battery anode material. *J. Electrochem. Soc.* 149, A1598-A1603 (2002).

103 Kim, H. & Cho, J. Superior lithium electroactive mesoporous Si@ Carbon core− shell nanowires for lithium battery anode material. *Nano Lett.* 8, 3688-3691 (2008).

104 Liu, X. H. *et al.* In situ TEM experiments of electrochemical lithiation and delithiation of individual nanostructures. *Adv. Energy Mater.* 2, 722-741 (2012).

105 Obrovac, M. & Christensen, L. Structural changes in silicon anodes during lithium insertion/extraction. *Electrochem. Solid-State Lett.* 7, A93-A96 (2004).

Chapter 5: Expanded Graphite as Superior Anode for Na-ion Batteries

5.1 Introduction

The Li-ion battery (LIB) industry has been continuously expanding over the last three decades, mostly due to the steadily increasing demands of a growing market for portable electronic devices. However, as demand emerges for hybrid and electric vehicles, and as emphasis shifts to the power grid and other large-scale applications, the limits of the natural abundance and uneven global distribution of lithium-containing precursors present unavoidable challenges to industry. For such large-scale applications, a low-cost and sustainable supply-chain is critical. As an alternative, Na-ion batteries (NIBs) have recently drawn significant attention, because, unlike Li, Na is a ubiquitous and earth-abundant element. NIBs were originally developed in the late 1980s, in approximately the same time period as LIBs[6,7,106], and the demand for large-scale energy storage for grid applications has recently revived the interest. Most of the recent research on NIB electrode materials has focused mainly on cathodes, but here we concentrate instead on a possible new anode material.

Since Li and Na share common properties as alkali metals, it is sometimes assumed to be convenient to transfer the insights gained from the science of LIBs to NIBs. However, Na^+ has a larger radius than Li^+, which directly affects the mass transport and storage in the electrochemical process. It makes many of the superior LIB anode materials, such as graphite, unsuitable for NIBs. Graphite, as the most common anode for commercial LIBs, has a long-range-ordered layered structure, and Li^+ can readily electrochemically intercalate between the graphite layers. The intercalated material

has a high theoretical reversible capability of 372 mAh g^{-1} and long cycle-life. However, the electrochemical sodiation/desodiation capacity of graphite is less than 35 mAh g^{-1}. [107,108] As demonstrated by recent theoretical calculations, the interlayer distance of graphite (~0.34 nm) is too small to accommodate the large Na^+ ion (Figure 5.1a), and a minimum interlayer distance of 0.37 nm is believed to be required for Na^+ insertion[109].

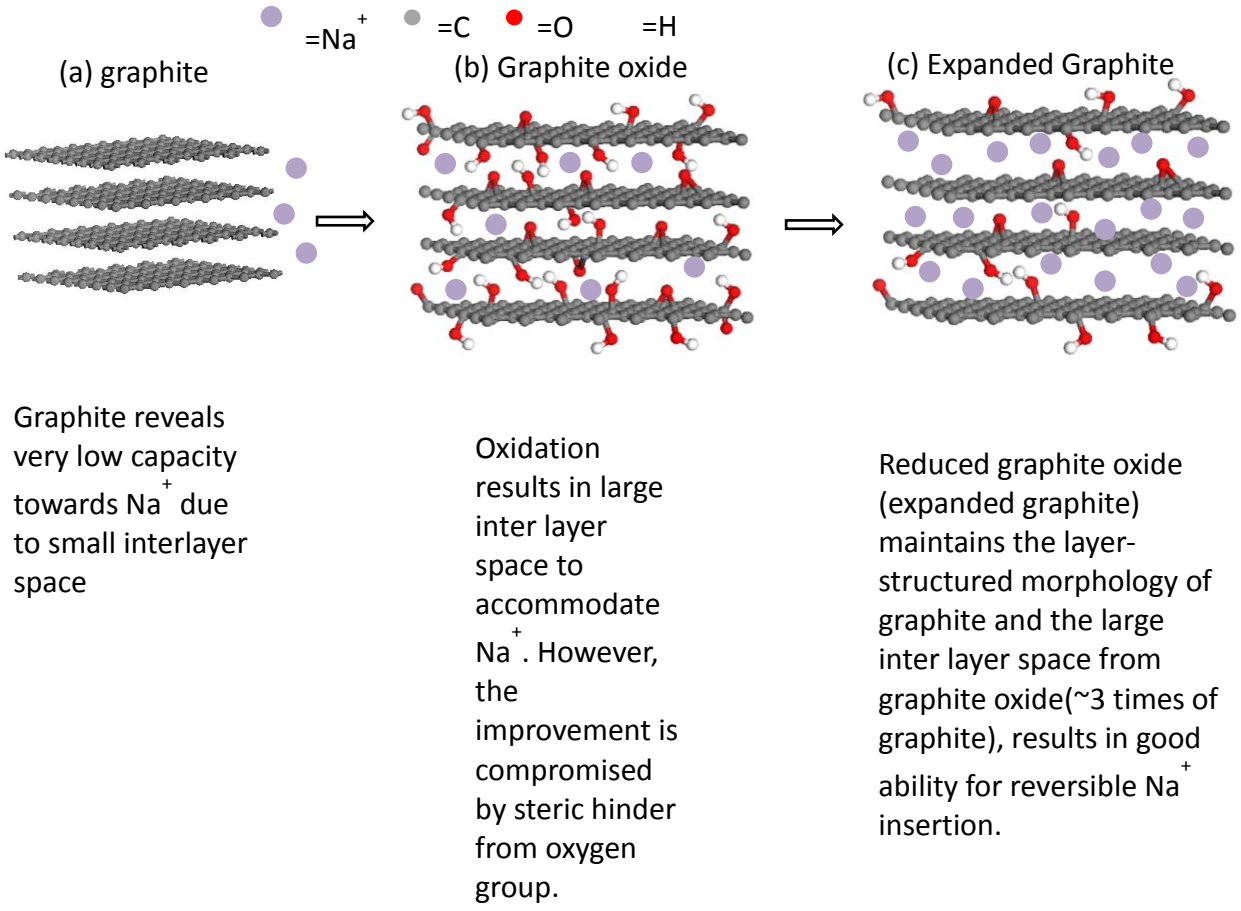

Figure 5.1 Schematic illustrations of the (a) graphite, (b) graphite oxide, (c) expanded graphite, and the mechanism for Na-ion storage.

A variety of carbon materials, such as carbon with different structures (soft carbons[108], hard carbons[108]), different compositions (hydrogen-contained carbons[108]), and

different morphologies (carbon nanotubes[109], porous carbons[110], hollow carbon nanoparticles[111], and reduced graphene oxides[112]) have been investigated as anodes for NIB in previous studies. Most of these carbon-based materials consist of few-layer-stacked graphite nanocrystallites with large interlayer distances in the range of 0.37-0.40 nm[109]. These localized nanocrystallites leave many disordered nanovoids within the materials[108-113], and it is believed that the Na^+ ions can reversibly insert into the graphite nanocrystallites and the nanovoids in these carbon materials. Na^+ insertion in nanocrystallite usually occurs in a wide potential range from 1.5 V to 0.1 V (vs. Na/Na^+), while the Na^+ filling into nanovoids happens in a low and narrow potential range of 0.1-0.0 V (vs. Na/Na^+)[108-113]. In these two mechanisms, the inter-layer insertion reaction would be preferred, since the pore-filling reaction occurs only at low potentials, where the insertion can be accompanied by Na plating during fast charging, causing Na loss and, more severely, battery failure due to electrical shorting. Certain conclusions can be drawn from these studies, and it is apparent that materials with long-range-ordered layered structures, larger interlayer distances, and low porosity are desired.

Here we report expanded graphite (EG) as a superior NIB anode material. EG is a graphite-derived material formed by a two-step oxidation-reduction process that retains the long-range-ordered layered structure of graphite, yielding a generally large interlayer distance (> 0.34 nm) (Figure 5.1 b, c). These features provide favorable conditions for electrochemical intercalation of Na^+ ions. Moreover, the interlayer spacing of EG can be manipulated by controlled oxidation and reduction processing, which positions EG as a promising anode material for NIBs. We report here that Na^+

indeed can reversibly insert into and extract from the EG, at an interlayer distance of 0.43 nm. The sodiation- and desodiation-induced micro-structure change of EG are dynamically captured during real-time imaging at the atomic-scale using *in situ* high-resolution transmission electron microscopy (HRTEM). The EG can provide a high reversible capacity of 284 mAh g^{-1} at a current density of 20 mA g^{-1}, 184 mAh g^{-1} at a current density of 100 mA g^{-1}, and retain 73.92% of the capacity after 2000 cycles. Along with the mature and low-cost synthesis technique of graphite anodes for LIBs, EG could be a very promising anode material for the NIBs industry in the near future.

5.2 Experimental Section

5.2.1 Graphit oxide (GO) and expanded graphite (EG) synthesis

GO was synthesized through a modified Hummer's method.[29] At room temperature, 1 g of graphite (synthetic, Sigma Aldrich) and 0.5 g of $NaNO_3$ (reagent plus, Sigma Aldrich) were added into 23 mL concentrated sulphuric acid (95%- 98%, ACS reagent, Sigma Aldrich) in a round bottom flask. The flask was then put into an ice bath. 3 g of $KMnO_4$ (ACS reagent, Sigma Aldrich) was added into the mixture slowly while stirring, during which the temperature was well controlled to lower than 20 °C. Then the temperature was brought to 35 °C and maintained for 2 hr. 46 mL of room temperature H_2O was added into the mixture slowly. The temperature was well-controlled to below 98 °C during this process. After mixing, the temperature was then slowly brought up to 98 °C and maintained for 30 min. 140 mL of warm water was further added to the liquid, followed by 20 mL of H_2O_2 (30 wt% in H_2O, Sigma Aldrich), upon which golden particles and dark brown solid particles were formed. The mixture was filtered while still warm. Around 1L of warm H_2O was further used

to wash the solid until the supernatant was pH neutral at the end of washing. The resulting dark brown solid was collected as the GO product. To synthesize EG, the fore-mentioned GO was reduced by heat treatment. GO powder was put into alumina combustion boat in tube furnace with a continuous flow of Ar. The temperature was then brought from 25 °C to 600 °C with a heating rate of 5 °C min^{-1}. Then, the temperature was maintained at 600 °C for 1 hr and 5 hr, to reach different degrees of reduction

5.2.2 Material characterization

The morphologies and microstructures of PG, GO and EG were characterized by a JEOL JEM-2100F TEM operated at 200 kV. For general structural characterization, the graphitic materials were transferred onto copper grids with amorphous carbon film support after stirring in isopropanol. For the XRD tests (Supplementary Figure S1), the sample was scanned from 5° - 90° at a scan rate of 0.5° per second in non-spin mode. The XRD data was collected by a D8 Advance diffractometer with LynxEye and SolX detectors in the X-ray Crystallographic Center at the University of Maryland. BET test was carried out on the Tristar II surface analysis system. In a typical measurement, ~100 mg of the powder sample was first degased for 5hr, and then loaded to the system to measurement.

Typical Raman tests (Supplementary Figure S2c) were carried out over the dried powder samples. For the *ex situ* Raman characterization (Supplementary Figure S7), in a typical procedure, EG anode material was assembled into a home-made glass cell with airtight structure. The cell was assembled with an EG electrode, a sodium metal counter electrode, and 1.0 M $NaClO_4$ in polycarbonate (PC) solvent liquid electrolyte

in glove box with Ar atmosphere. Raman data was collected by Horiba-Jobin-Yvon Raman microscope in the University of Maryland Nanocenter with laser wavelength of 532 nm.

X-ray photoelectron spectroscopy (XPS) investigation was performed on powdered samples at room temperature. Data was collected using a high-sensitivity Kratos AXIS 165 spectrometer with survey pass energy of 160 eV and high resolution pass energy of 20 eV, also at the University of Maryland Nanocenter.

The SSNMR experiment were performed at ^{1}H frequencies of 500.16 MHz with Bruker Avance III system using a Bruker 3.2-mm triple-resonance E-free CP-MAS probe in a double resonance mode. ^{13}C MAS spectra in Figure 4 were collected by a rotor-synchronous echo sequence with (a) and without (b, c) a background suppression RF scheme[114] using a Kel-F cap. The background suppression scheme was used in (b, c) to quantify the signals of very limited oxidized species without the effects of background signals. In the ^{13}C-^{1}H REDOR experiments,[115,116] the data were collected with ^{13}C π-pulse sandwiched by ^{13}C-^{1}H dephasing periods of 4 rotor cycles (τ_R = 66.7 μs). The details are described in the supplementary material.

5.2.3 Electrochemical characterization

Electrochemical properties were characterized using a half-cell against a pure Na counter electrode. To assemble a test cell, the EG powder was mixed with 15 wt % of Na alginate in water in mortar and milled for 30 minutes. The resulting slurry was then cast on copper foil. After drying at room temperature for ~12 hr, the sample was then transferred into a standard vacuum oven kept at 100 °C for overnight. A 0.5 inch circular die-punch was used to form the electrode. The loading amount of active

material was ~0.5 mg cm^{-2}. Coin cells, consisting of an EG electrode, a sodium metal counter electrode, Celgard 3501 separator, and 1.0 M $NaClO_4$ in polycarbonate (PC) solvent liquid electrolyte, were assembled in a glove box under Ar atmosphere for further electrochemical tests.

Galvanostatic charge/discharge was carried out on an *Arbin* BT-2000 test station. Cells were cycled between 0.0 V and 2.0 V (vs. Na/Na^+) at different current densities. After the cell reached the cut off voltage, it was relaxed for 10 mins before subsequent charge or discharge. The capacity was calculated based on the mass of active material.

For the rate capability tests, cells were pre-cycled for 20 cycles for activation and then charged-discharged at different current densities between 0.0 V and 2.0 V (Na/Na^+). The capacity is calculated based on the mass of EG.

The cyclic voltammetry test was carried out on the Solartron 1260/1287 Electrochemical Interface test station (Solartron Metrology, UK). Cells were pre-cycled for 20 cycles to achieve the stable status before loaded to the testing system. The scan range was 0-2V (vs. Na/Na^+) with various scan rates.

5.2.4 Setup of *in situ* HRTEM tests

In situ HRTEM experiments were performed with a customized NanoFactory manipulation holder equipped with a piezo-driven Pt probe. In a typical experiment, EG was glued onto a specimen rod using conductive Ag epoxy, and Na metal was scratched off a fresh-cut surface of Na bulk using the Pt manipulator inside a glove box filled with high purity nitrogen to prevent oxidation. Then the Na metal was

intentionally exposed to the air for less than 5 s during the holder loading process, in order to grow a thin layer of Na_2O on the surface, serving as a solid electrolyte. During the *in situ* operation, potentials of -1.0 V to -4.0 V were applied to EG with respect to Na metal to initiate sodiation, and +1.0 V to +4.0 V for desodiation.

5.3 Result and Discussion

5.3.1 Material and structural design

EG was synthesized by oxidizing pristine graphite (PG) to become graphite oxide (GO) using modified Hummer's method[29] and followed by a partial reducing process of GO. The modified Hummer's method is well known as an oxidization method to form GO in the graphene synthesis technique[112]. In a typical graphene synthesis procedure, the resulting GO is sonicated before (or after) the reduction reaction to peel off the functionalized graphene layers from graphite and acquire single-layer or few-layer graphenes. In our synthesis, we intentionally omitted the sonication step to avoid the damage caused by sonication and maintain the long-range-ordered layered structure. More experimental details are provided in Methods.

The crystal structures of PG, GO and two EG samples (EG-1hr and EG-5hr with 1hr/5hr denoting the thermal reduction period applied on GO to obtain the sample) were characterized using powder X-ray diffraction (XRD) (- Figure 5.2). For the purpose of systematically analysing the reduction time effect, GO was considered as EG-0hr to compare with EG samples (EG-1hr and EG-5hr). PG exhibits a sharp peak at $2\theta \sim 26.6^0$(Supplementary Figure S1), which corresponds to the diffraction of (002) plane with an interlayer distance of 3.36 Å (~0.34 nm)[117,118]. Upon oxidation, the

inserted oxygen containing groups will attach to both sides of the single graphene plane, causing distortion of the interlayer structure[119,120]. The diffraction peak of GO shifts to $2\theta \sim 13^0$, which indicates an enlarged inter-planar distance. After thermal reduction for one hour, the diffraction peak of EG-1hr shifts back to $2\theta \sim 23^0$, yet is still smaller than that in graphite (26.6^o), exhibiting a graphite-like structure with a larger inter-planar distance.

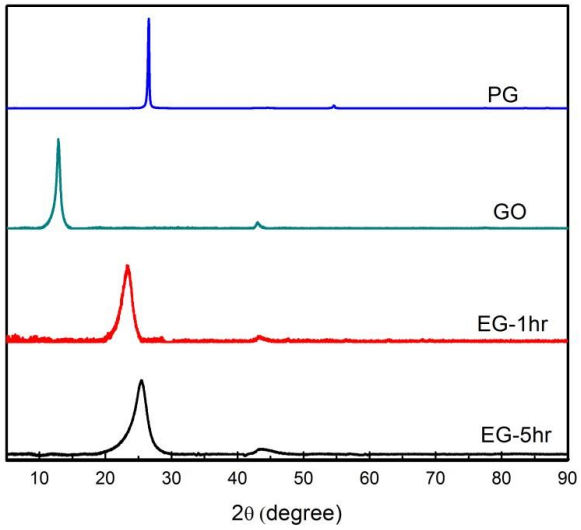

Figure 5.2 XRD pattern for pristine graphite (PG), graphite oxide (GO) and expanded graphite (EG-1hr and EG-5hr).

As thermal reduction time increases to 5 hours, the diffraction peak of EG-5hr shifts to $2\theta \sim 25.3^0$, indicating shrinkage of inter-layer distance compared with EG-1hr. The XRD data can be used to estimate the *d* spacing evolution trend via Bragg equation. Notice that this XRD result is the raw data without refinement. Since there are lots of factors, for example, the correct positioning of the sample, the scanning rate and the equipment alignment, would have significant influence on the absolute 2θ values, the

accurate *d* spacings information is hard to achieve directly from Bragg equation estimation. Further refinement and the uncertainty calculation are expected if the lattice data is desired from XRD. [121]

The surface areas of PG, GO and EG samples were characterized by using N_2 gas adsorption-desorption. The Brunauer-Emmett-Teller (BET) surface areas are measured to be 13.52 $m^2 g^{-1}$ for PG, 64.89 $m^2 g^{-1}$ for GO, 30.22 $m^2 g^{-1}$ for EG-1hr, and 34.70 $m^2 g^{-1}$ for EG-5hr. Both EG samples reveal a low surface area, which is much smaller than that of typical graphene/graphene oxide prepared through Hummer's method [122], indicating low exfoliation degree and good graphite-like stack morphology retention. On the other hand, the low surface area of EGs also implies only small amount of pores are introduced during oxidation and thermal reduction process. Different from graphite, the N_2 adsorption-desorption isotherm profiles of GO, EG-1hr and EG-5hr exhibit no limiting adsorption at high P/P_0 (Figure 5.3a), revealing a typical character of plate-like particle with slit-shaped pores [123] . The specific surface area of PG used in this study is 3 times higher than that of previously reported graphite, [124] and is similar to that of the hard carbon (SX114i19 in ref. 19) [125]. The EGs' surface areas are similar to the hard carbon (SX114i5 in ref. 19) reported by J. Dahn [125]. The tap densities for PG, GO, EG-1hr and 5hr samples were measured to be 0.72 g cm^{-3}, 4.38 g cm^{-3}, 2.38 g cm^{-3}, and 1.88 g cm^{-3}(Figure 5.3b). The PG's tap density is similar to hard carbon [125]. The EG samples were observed to be more condensed than the reported carbon material used in LIB [125]. The graphitization degree of PG, GO and EG materials was determined by Raman spectroscopy. All samples exhibit typical D band (centered at ~1360 cm^{-1}) and G

band (centered at ~ 1585 cm^{-1}) for carbon material.[126] The D band corresponds to the disordered carbon while the G band represents the typical signal for graphite-like morphology in carbon material. The I_D/I_G intensity ratios for PG, GO, EG-1hr and 5hr are 0.22, 0.86, 0.88 and 0.97 (Figure. 5.3c), indicating that EG partially maintains the graphitic character.

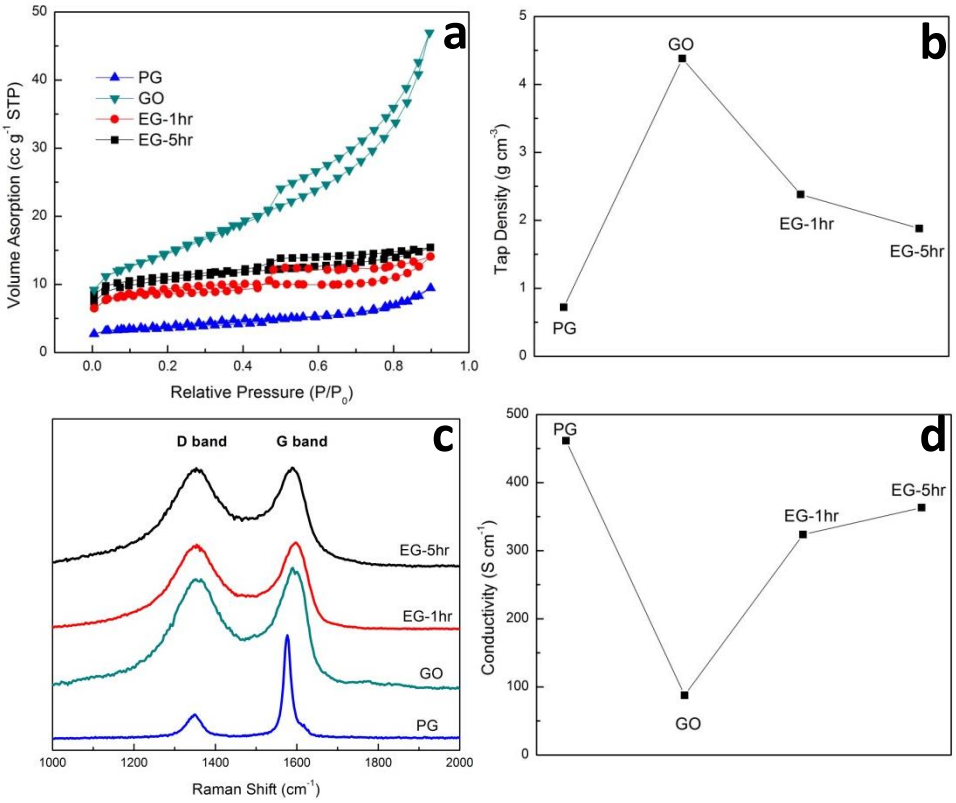

Figure 5.3 (a) N_2 adsorption-desorption isotherm, (b) tap density, (c) Raman profile, and (d) conductivity of pristine graphite(PG), graphite oxide(GO), EG-1hr, and EG-5hr.

The electronic conductivities of PG, GO, EG-1hr, and EG-5hr were measured by linear-scan method and were determined to be 461.47 S cm^{-1}, 87.65 S cm^{-1}, 322.62 S cm^{-1}, and 363.40 S cm^{-1}, respectively (Figure 5.3d). Both EG samples show much

better conductivity than GO (EG-0hr) due to the removal of O-containing groups during thermal reduction.

The structures of PG, GO, and EGs were further characterized by TEM. Figure 2 shows HRTEM images of the cross-sectional view for PG, GO, EG-1hr and EG-5hr, in which the layered structures of these specimens are well resolved by the alternating bright and dark contrast. The PG displays well-defined layers of long-range order stacking parallel to each other (Figure 5.4a).

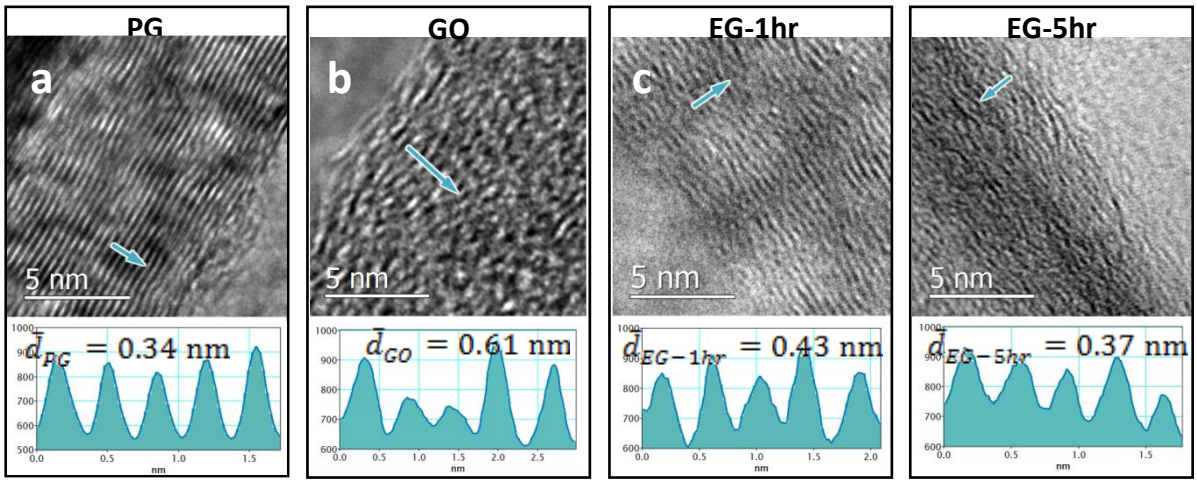

Figure 5.4 High-resolution TEM images showing cross-sectional layered structures for (a) graphite, (b) graphite oxide, (c) expanded graphite (reducing 1 h), and (d) expanded graphite (reducing 5h). Contrast profiles along the arrows indicate interlayer spacings of corresponding samples.

After oxidation, such long-range order is disrupted by massive intercalation of oxygen in the PG interlayer, forming a more disordered pattern with only localized short-range ordering, as shown in Figure 5.4b. However, after partial reduction, the material recovers toward a well-organized morphology, while preserving expanded

interlayer distances and the long-range channels suitable for Na ions transport, as shown in Figure 5.4c & d. In addition, the progressive change in interlayer distance is also clearly apparent. The contrast line-profiles across five stacking layers at representative locations, indicated by the arrows, are plotted under the corresponding images. The average interlayer spacings are measured to be approximate 0.34 nm for PG, 0.61 nm for GO, 0.43 nm for EG-1hr and 0.37 nm for EG-5hr. It is obvious that the distance between PG layers is expanded after the oxidation reactions due to the insertion of oxygen containing groups, and that it still retains larger than PG after reduction treatments.

5.3.2 Nature and content of oxygen-containing groups in the interlayer

From above XRD and HRTEM results, it is clear that the interlayer distances of PG, GO and EGs are related to the nature and content of oxygen-containing groups in the interlayer. So, the nature and amount of these O-containing groups in PG, GO and EG samples (EG-1hr and EG-5hr) were investigated using X-ray photoelectron spectroscopy (XPS), and the results are shown in Figure 5.5a-d, where C 1s peak presents at ~284.8 eV and O 1s presents at ~533.6 eV. Figure 5.5e illustrates the C/O ratio calculated from the intensity of C 1s and O 1s peaks for different samples. PG contains a very small amount of oxygen (3.56%) (Figure 5.5a). Upon oxidation, the intensity of O 1s peak increases significantly (Figure 5.5b) and the oxygen component reaches to 33.82%, indicating a high oxidation state. After 1 hour thermal reduction in Ar, the oxygen content of EG-1hr sample reduces to ~10% (Figure 5.5c), which is much less than that in GO, but it is still three times higher than that in PG.

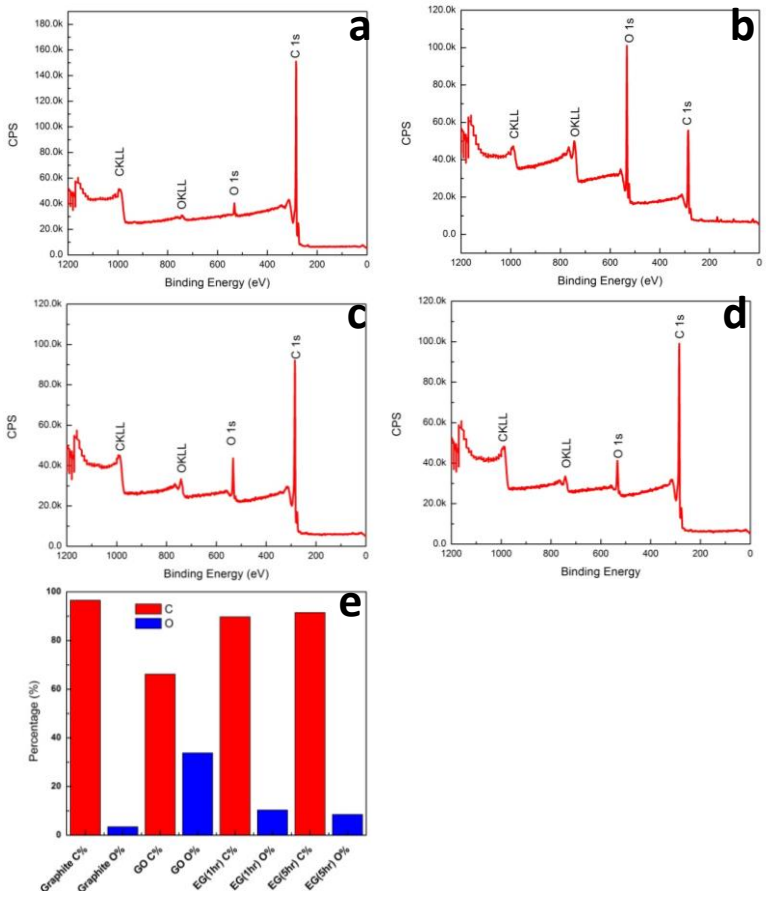

Figure 5.5 Wide-range XPS spectra of (a) graphite, (b) GO, (c) EG-1hr, (d) EG-5hr, and (e) Percentage of C and O element ratio in different samples.

The residual 10% oxygen-containing groups maintain the interlayer distance at ~0.43 nm (Figure 5.5c). As the reducing time increases from 1 hr to 5 hr, the oxygen content further drops to 8% in EG-5hr. The 2% decrease in O component was attributed to further loss of functional groups between graphene layers, resulting in some shrinkage of the interlayer distance, as evidenced by the HRTEM results in Figure 5.4d.

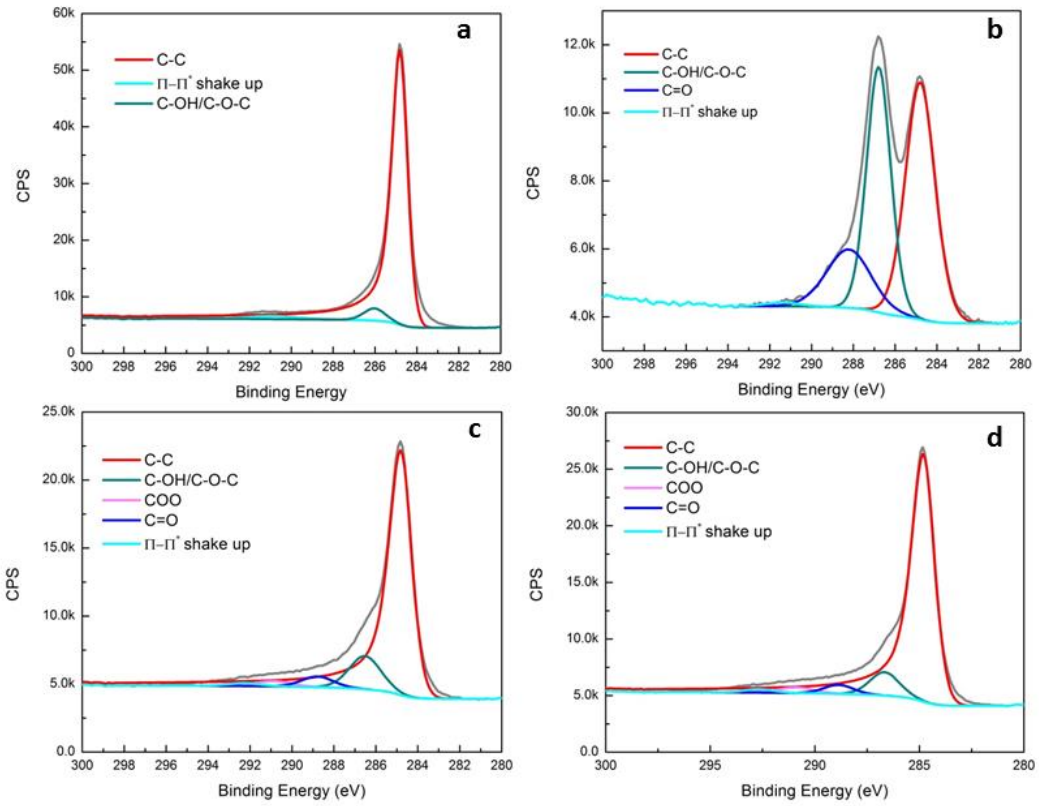

Figure 5.6 XPS spectra of C 1s spectra of (a) PG, (b) GO, (c) EG-1hr, and (d) EG-5hr.

The nature of O-containing functional groups was further analyzed by the high resolution C 1s scans (Figure 5.6). The minor O component in PG exists in form of C-OH or C-O-C groups (Figure 5.6a), while the O content in GO mainly exists as C-OH, C-O-C, and C=O components (Figure 5.6b). After thermal reduction, most of the O-containing groups in GO are removed. A small amount of residual O in the interlayer exist as C-OH/C-O-C and C=O groups in EG-1hr and EG-5hr (Figure 5.6c & d).

The structure evolution along O-containing groups amount change was further investigated by magic-angle-spinning nuclear magnetic resonance (MAS-NMR)

experiment. In the ^{13}C spectrum of GO (Figure 5.7a), three major peaks at 131 ppm, 69 ppm, 61 ppm evidence the occurring of the oxidization which is consistent to the previous study[127,128]. The weak peaks at ~165 ppm and ~190 ppm (indicated by blue arrows) can be assigned to $-CO_2-$ and C=O [129], consistent with the XPS measurements. The EG-1hr and EG-5hr samples show a single broader major peak at 117 ppm (Figure 5.7b) and116 ppm (Figure 5.7c) with another broad shoulder peak at ~170 ppm. The observed ^{13}C shifts are consistent with those for sp^2 carbons without oxidized sites (~120 ppm) such as graphene or graphite, suggesting the restoration of sp^2 conjugation network. The change in the ^{13}C shift position for the sp^2 species from ~130 ppm in GO to ~120 ppm in EG reflects the removal of electron-withdrawing oxygen-containing groups by the reduction. No noticeable peaks were observed either at 60 or 70 ppm, although a weak peak for the C-OH group may overlap with a tail of the sp^2 carbons at 120 ppm. The results suggest that thermal reduction for 1 hr is sufficient to restore the sp^2 network in the EG sample. Based on the integral intensities of the spectra at 40-80 ppm region in Figure 5.7b & c, these oxidized species should constitute approximately 3-8% of the carbon. This portion of the oxidized carbon is attributed to the C-OH or epoxide from graphene plane that is highly related to the interlayer spacing. The broad shoulder peak at ~170 ppm may be attributed minor species (such as C=O and $-CO_2H$ species) which that could be found around the edges/defects. Minor discrepancies from the XRD results may be attributed to the oxygen species at the edges/defects.

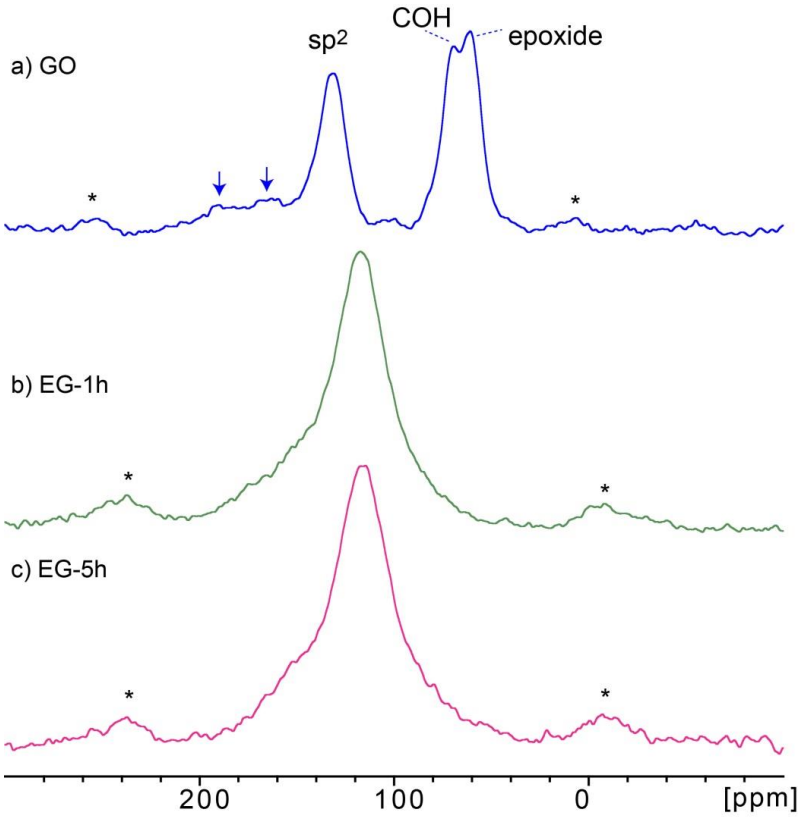

Figure 5.7 1D ^{13}C MAS solid-state NMR spectra of (a) graphite oxide (GO), (b) expanded GO (EG) that was thermally reduced for 1 h (EG-1hr), and (c) EG thermally reduced for 5 h (EG-5hr). All the spectra were obtained at a ^{13}C NMR frequency of 125.78 MHz frequency with 15 kHz MAS for the samples of (a) 33 mg, (b) 38 mg, (c) 45 mg. The ^{13}C MAS spectra were obtained with direct ^{13}C excitation by a $\pi/2$-pulse followed by a rotor-synchronous echo. The peaks marked by * denote spinning sidebands. The recycle delay was 2 s, and the experimental times were (a) 3 h, and (b, c) 7 h. A Lorentz broadening of 300 Hz was applied to improve the signal-to-noise ratios. ^{13}C T_1 values of the samples were found to be 0.5-0.6 s. The ^{13}C $\pi/2$-pulse widths are (a) 3.65 μs and (b, c) 5.75 μs.

To identify C-OH groups and other ^{1}H containing species in the GO and EG samples, ^{13}C-^{1}H dipolar dephasing experiments were performed by using a ^{13}C-^{1}H REDOR pulse sequence. It is notable that for GO sample, the signal for C-OH was mildly dephased (Figure S5.8).

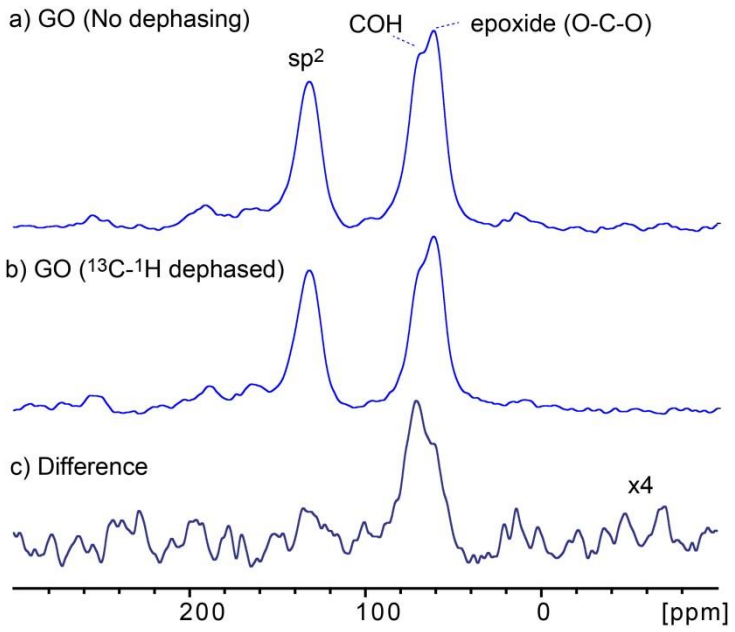

Figure 5.8 ^{13}C MAS spectra of GO (a) without and (b) with ^{13}C-^{1}H dipolar dephasing by ^{13}C-^{1}H REDOR, and (c) the difference spectrum (a) – (b). The spectrum in (c) is magnified by 4 times. The ^{13}C signals were excited by a $\pi/2$-pulse. The pulse widths for the $\pi/2$ and π-pulses for ^{13}C are 3.65 s and 7.3 μs while that for a ^{1}H π-pulse is 6.28 μs.

The difference between non-dephased spectrum (Supplementary S4a) and dephased spectrum (Figure 5.8b) clearly shows that the signal intensities for the C-OH and epoxide groups are reduced by about 20% and 13%, respectively while the intensity

for the sp^2 group is reduced by only 6%. The strongest dephasing is a direct evidence of the existent of massive O-containning species, especially the C-OH, in GO.

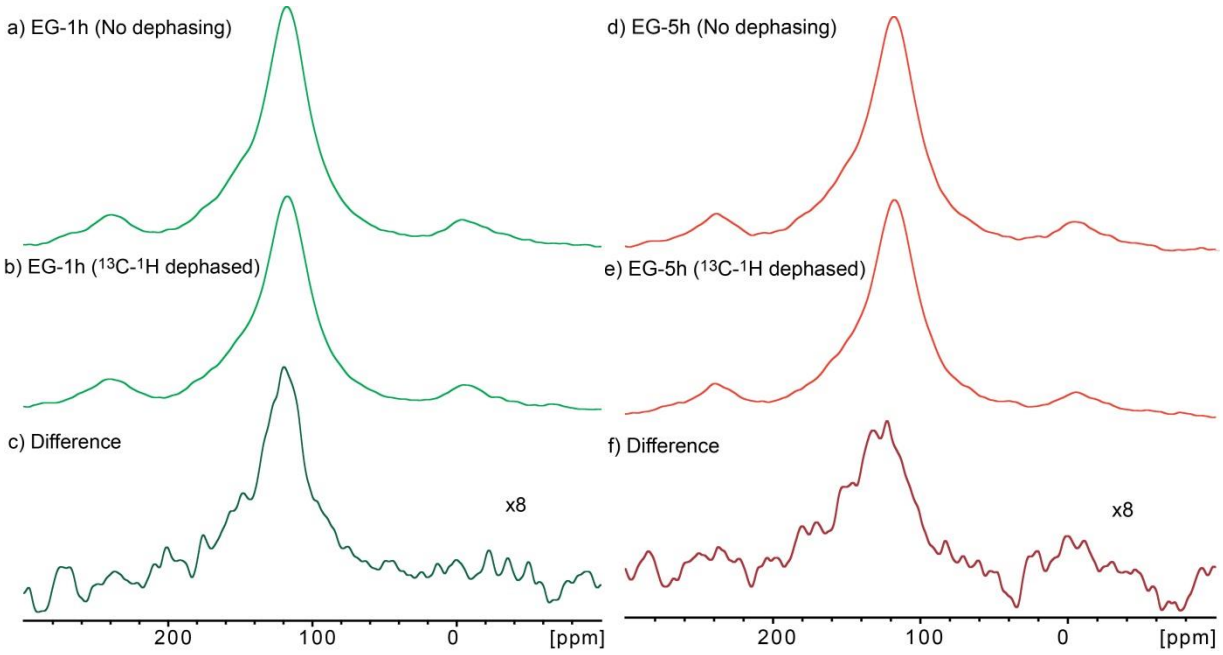

Figure 5.9 ^{13}C MAS spectra of (a-c) EG-1h and (d-f) EG-5h (a, d) without and (b, e) with ^{13}C-^{1}H dipolar dephasing by ^{13}C-^{1}H REDOR, together with (c, f) the difference spectra. The spectra in (c, f) are magnified by 8 times. The pulse widths for the $\pi/2$ and π-pulses for ^{13}C are 5.25 s and 10.5 μs while that for a ^{1}H π-pulse is 16 μs.

This approach is adopted to analyze EG-1hr and EG-5hr. Figure 5.9 shows ^{13}C MAS spectra of EG-1hr (Figure 5.9a-c) and EG-5hr (Figure 5.9 d-f) without and with ^{13}C-^{1}H dipolar dephasing by ^{13}C-^{1}H REDOR, together with (c, f) corresponding difference spectra. For the both samples, no notable selective dephasing was observed unlike the above-mentioned experiment for GO. Rather, the peaks corresponding to

sp^2 group at ~120 ppm were uniformly dephased for (c) EG-1hr and (f) EG-5hr by 12% and 8 %, respectively.

It is noteworthy that the signal reduction is higher than that was observed for sp^2 species in GO. The results indicate that the surface of the restored graphene sheets in EG can be covered by hydrogen containing species, and these species may be, in part, responsible for expanded inter-layer distances. Indeed, that EG-5hr shows a lower dephasing than EG-1hr, which is consistent with the observed smaller interlayer distance for EG-5hr.

5.3.3 Effect of oxygen content on sodium storage capacity

Theoretical calculations have revealed that when the interlayer spacing increases to ~0.37 nm, the energy barrier for Na^+ insertion drops to 0.053 eV[109]. This calculation suggests that it is thermodynamically feasible to electrochemically insert Na^+ into EG-1hr. Although a large interlayer distance is desired for Na^+ insertion, too many oxygen-containing groups between graphene layers could reduce the available positions for Na^+ and slow the Na^+ transport. The amount of remaining oxygen containing groups in the interlayer of EG should in principle be optimized to maintain the sufficient interlayer distance and maximize possible positions for Na-ion storage.

The effects of oxygen content on sodiation/desodiation capacity were investigated using galvanostatic charge/discharge at a current density of 20 mA g^{-1}. The charge and discharge curves of PG, GO, EG-1hr, and EG-5hr at the 2^{nd} cycles are presented in Figure 5.10a. Retarded by the small interlayer spacing, PG has a negligible sodium storage capacity of ~13 mAh g^{-1}, which is widely known and has been reported previously[130]. Oxidation of graphite increases the interlayer distance from 0.34 nm to

0.61 nm, allowing Na^+ intercalation into interlayer of GO. The GO shows monotonic voltage curves during the whole sodiation-desodiaton process with an increased capacity of ~156 mAh g^{-1}. However, 33.82% of oxygen-containing groups in the interlayer reduce the amount of possible positions for Na^+ storage. After 1 hour of thermal reduction, 23.80% of the O-containing functional groups are removed, allowing more Na^+ to insert into the carbon interlayer of EG, despite the reduced interlayer distance of EG-1hr as 0.43 nm. EG-1hr can deliver a high reversible Na^+ capacity of ~300 mAh g^{-1}, which is significantly higher than PG and GO. When the reduction time extends to 5 hours, the capacity of EG-5hr drops to ~100 mAh g^{-1}. Although similar charge-discharge pattern was observed between EG-1hr and EG-5hr, the capacity delivered by EG-5hr decreased significantly, implying that the interlayer distance predominantly controls the Na^+ storage capacity. The sodiation curve of EGs clearly consists of two stages, i.e. monotonic sloping voltage profile between 2.0 and 0.3 V (vs. Na/Na^+) and an inclined voltage plateau from 0.3 to 0.0 V (vs. Na/Na^+). As reported by previous studies on Na storage in hard carbon and soft carbon, the monotonic curves occurring in the high voltage region (> 0.3 V) correspond to insertion/extraction of Na^+ between graphene layers in EG [108,131] while the low-voltage plateau may represents the Na^+ insertion/extraction in the pores/defects[108,131]. The slope in the low voltage region (<0.3V) in desodiation curve could be possibly attributed to hysteresis cause by the interaction between Na^+ and the residual hydrogen [108,132] The second stage between 0.3-0.7 V should be corresponded to the Na^+ removal from pores while the slope at high voltage range(>0.7V) should be attributed to Na^+ extraction from graphitic layers.

The EG has long range graphene layer stacked approximately parallel to each other producing relative turbostratic disorder, which is similar to soft carbon.[108] When Na-ion inserts into turbostratically arranged layers, the distribution of sites generates a range of chemical environments, thus a sloping potential curves.[108] However, when the sodium inserts into pores in the EG generated during oxidation/reduction process, there is very little charge transfer from the carbon to the sodium. Therefore, the sodium insertion into/extraction from pores shows a low voltage plateau.[108] In addition, the existing of O-containing groups like –C=O could also contribute to Na^+ storage, exhibiting sloping profile at a high voltage range.[133]

As an observed result, charge/discharge capacity initially increases (from PG, GO, to EG-1hr), and then decreases (from EG-1hr to EG-5hr) with oxidation and reduction process. The cycling tests of PG, GO, EG-1hr and EG-5hr are shown in Figure 5.10b. All materials show stable cycling performances in the first 30 cycles except the initial few cycles, with EG-1hr exhibiting the highest sodium storage capacity. So, EG-1hr was selected for further electrochemical tests and investigation of sodium storage mechanisms. And thus the term "EG" that appears in the following sections refers to EG-1hr.

5.3.4 Electrochemical performance of EG

The thermodynamic equilibrium potentials of EG during sodiation/desodiation were measured using the galvanostatic intermittent titration technique (GITT) [134] GITT is a novel method that is widely used to determine the true ion diffusion in electrode. By setting a small constant current on the electrode and following by a long pulse, the

equilibrium voltage of the material in phase changes can be achieved.[134] By measuring this equilibrium voltage, the real ion diffusion profile can be analyzed.

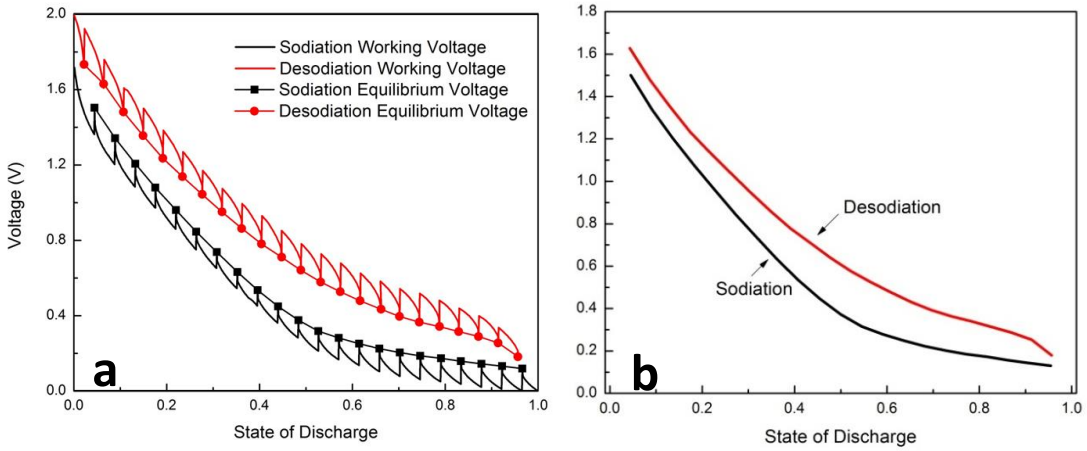

Figure 5.10 (a) Working and equilibrium voltage profile of EG during GITT measurement. (b) Normalized equilibrium voltage profile of EG in GITT.

Fig. 5.10a shows the working potential in the GITT test with all the equilibrium potential highlighted in dots and linked. To get a better view of the equilibrium potential profile, the equilibrium potential at different states of charge (SOC)/discharge (SOD) is shown in Fig. 5.10b. The open-circuit (equilibrium) potential curves of EG confirm that equilibrium potentials of EG almost linearly change with SOC/SOD when Na-ion insertion/extraction in the graphene layers at potential above 0.3 V (Na/Na^+), while the equilibrium potential shows a plateau when Na-ion inserts/extracts in nano-pores at potential below 0.3 V (Na/Na^+). In addition, there exists a small (thermodynamic) potential hysteresis of 0.2-0.3 V between sodiation and desodiation. The potential hysteresis has been observed in hydrogen-

containing carbon during sodiation/desodiation where the residual hydrogen terminates aromatic fragments in the carbon matrix [108]. Therefore, the function groups may be responsible for the potential hysteresis. The potential hysteresis was also observed in GO anodes, but is absent in soft carbon.[108-111]

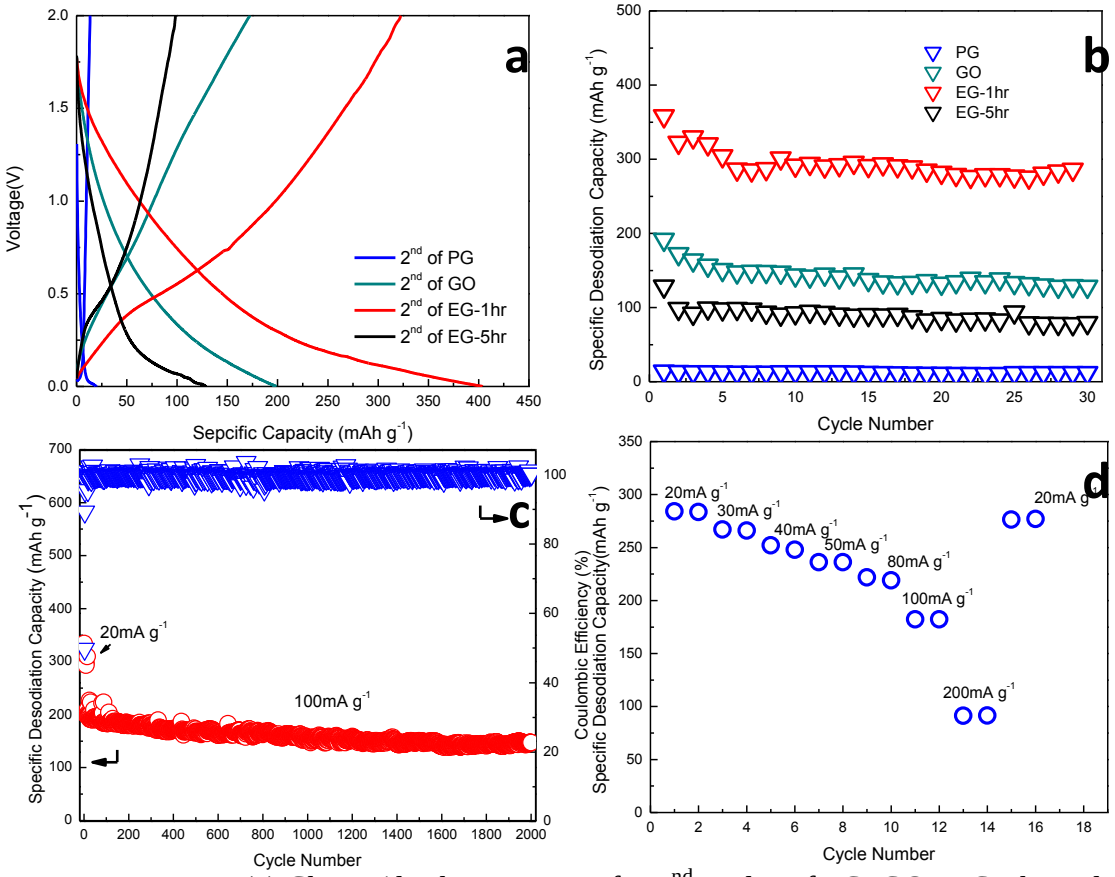

Figure 5.11 (a) Charge/discharge curves for 2nd cycles of PG, GO, EG-1hr and EG-5hr at current density of 20mA g^{-1}. (b) Capacity stability for (PG), GO, EG reduced for 1 hr and 5 hr. (c) Long-term cycling stability of EG. (d) Rate capability for EG after charge/discharge at 20 mA/g for 20 cycles with capacity reducing from initial 400 mAh/g to 284 mAh/g. Electrolyte is 1M $NaClO_4$ in PC.

The long-term cycling stability of EG was investigated at a low cycling rate of 20 mA g^{-1} for the first 10 cycles to achieve a full sodiation capacity and then at a high current

density of 100 mA g^{-1}, as shown in Figure 5.11c. The EG demonstrated excellent cycling stability for 2000 cycles with a very low capacity decay rate of ~0.013% per cycle from the 11^{th} cycle to 2000^{th} cycle. The coulombic efficiency in the 1^{st} cycle was around 49.53%, and approaches 100% after ~10 cycles.

The low coulombic efficiency in the first few cycles is due to the formation of solid electrolyte interphase (SEI) film, which can likely be reduced by (1) changing the electrolyte composition and (2) reducing the defects and voids of EG, both of which have been successfully applied to LIBs.

For the rate capability tests, technologically-significant capacities were achieved up to a current density of 200 mA g^{-1}. The specific cell was firstly cycled at 20 mA g^{-1} for 20 cycles to achieve stable cycling status prior to the rate capability experiment. As shown in Figure 5.11d, EG exhibits a capacity of 284 mAh g^{-1} at 20 mA g^{-1}, 184 mAh g^{-1} at 100 mA g^{-1}, and 91 mAh g^{-1} at 200 mA g^{-1}, and 278 mAh g^{-1} when the current density is changed back to 20 mA g^{-1}, demonstrating the stability of EG under a wide range of charge-discharge conditions.

5.3.5 Investigation on the sodium storage mechanism in EG

Cyclic voltammetry was utilized to analyze the sodium storage mechanism. EG was tested at the scan rates of 0.05 mV s^{-1} 0. 1 mV s^{-1}, 0.5 mV s^{-1}, 1 mV s^{-1}, 2 mV s^{-1}, 3 mV s^{-1}, 5 mV s^{-1}, 10 mV s^{-1}, and 20 mV s^{-1}, as shown in Supplementary Figure 5.12a. In Figure 5.12b & 6c, a linear relationship was found between the capacity and the reciprocal square root of scan rate, suggesting that the capacity was mainly limited by ion diffusion, similar to most traditional battery electrodes[135], because capacitive contributions, i.e. pseudocapacitance due to surface reaction between Na^+ and O-

containing functional groups (for example –C=O)[133] and double layer charging, should be independent of the scan rate[136]. The capacitive contribution was approximately estimated by extrapolating the plot to $V^{-1/2} \rightarrow 0$, and it only contributed to 10% of the total sodiation capacity (Figure 5.12a) and 11% of the total desodiation capacity (Figure 5.12b) at 0.05 mV s^{-1} (~0.1C rate), indicating the majority of the capacity is due to intercalation and it is highly reversible.

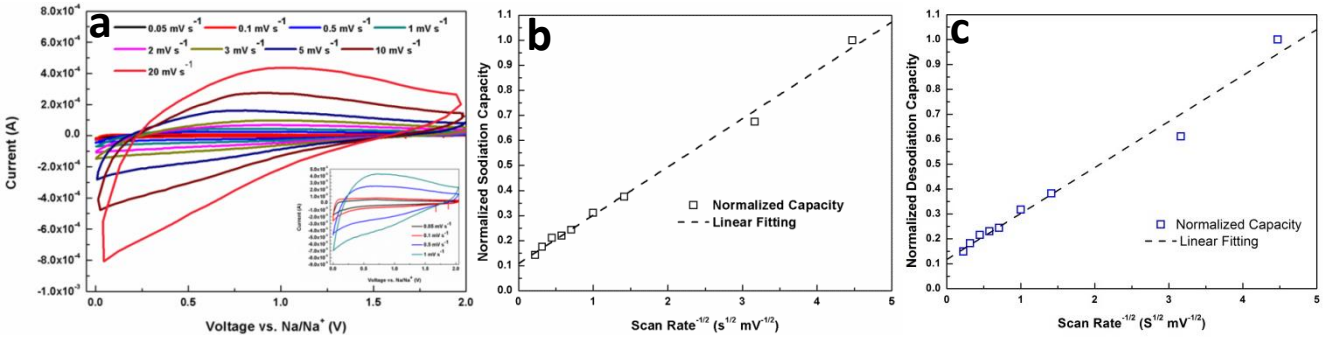

Figure 5.12 (a) Cyclic voltammograms of EG-1hr from 0.05 to 20 mV s^{-1}. The inset shows the results from 0.05 to 1 mV s^{-1}. (b) Sodiation, and (c) Desodiation capacity Q versus $V^{-1/2}$ profile with the dashed line indicating linear fitting between them. All capacities have been normalized by the value under 0.05 mV s^{-1}.

This mixed storage mechanism was also observed for lithium storage in soft carbon[137] in which the lithium storage capacity from intercalation was found to be reversible and stable with cycling[30]. This explains the long and stable cycling performance of EG (Figure 5.11c), since majority of the sodium storage capacity in EG is attributed to intercalation as demonstrated by Figure 5.12a,b .

In situ TEM observation was conducted to provide further insights into the sodium storage mechanism and microstructure evolution of EG during the sodiation and

desodiation processes. Figure 5.13a illustrates the experimental setup of the NIB in the half-cell configuration, in which the EG glued on a brass rod with conducting adhesive serves as the working electrode, and the Na metal on a Pt manipulator as the counter electrode. A layer of naturally formed Na_2O on the surface of Na source due to residual oxygen in the TEM vacuum is confirmed by the electron diffraction pattern from this area (Figure 5.13h) and serves as the solid electrolyte for Na ion transportation. The red boxed region at the curled edge of the graphite bulk was selected for high-resolution observations during the electrochemical reactions, and the corresponding close-up TEM morphologies for pristine EG, sodiated EG and desodiated EG are shown in Figure 5.13 b-d, respectively. To extract the relevant contrast, boxed areas at the approximate positions are re-plotted to display the representative features after filtering out high-frequency noise, as shown below the corresponding TEM images in Figure 5.13e-g, respectively. The EG displays a microstructure with well-aligned and long-range-ordered graphite layers (Figure 5.13b, e) and contains long-range pure graphitic structure with large interlayer distance (Figure 5.13h). After contacting the surface Na_2O electrolyte to the EG and applying a negative voltage of -3 V on the EG electrode (vs. Na metal), the sodiation process initiates. As the Na ions migrate into the EG, the shape of the EG changes by tilting or distorting to accommodate the large-scale morphology changes.

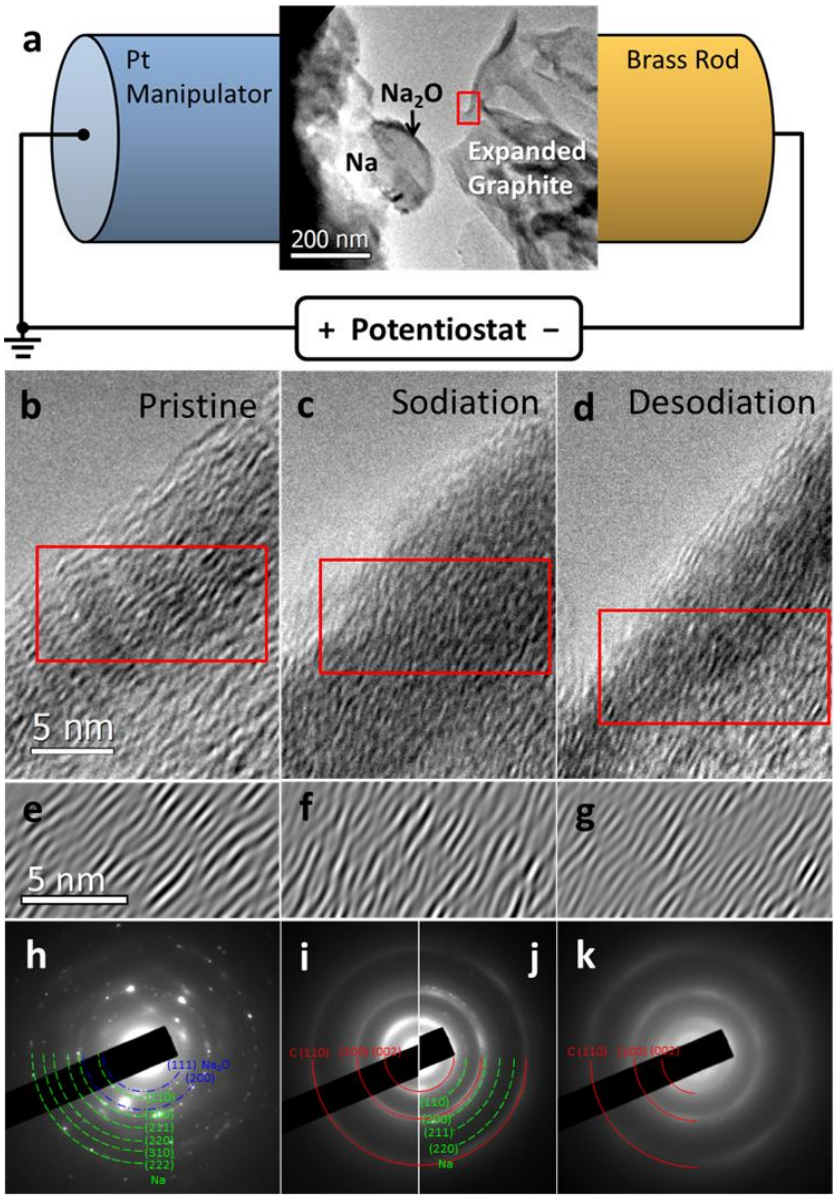

Figure 5.13 (a) Schematic illustration of *in situ* experimental setup for the half-cell configuration of the NIB. TEM graph shows EG on brass rod as the anode, Na metal on Pt manipulator as the counter electrode, and Na_2O on Na surface as the solid electrolyte. The boxed region in (a) corresponds to high-resolution images in (b)-(d). Typical microstructures of (b) pristine EG, (c) EG after the first sodiation, and (d) EG after the first desodiation. (e)-(g) Filtered TEM close-up images indicating

representative microstructural features corresponding to the boxed areas in (b)-(d), respectively. Electron diffraction patterns from (h) Na source area and EG area, (i) EG at pristine state, (j) EG after the first sodiation, and (k) EG after the first desodiation.

It is obvious that the microstructural disorder is complicated and more ripple-like features appear in the graphite layered pattern (Figure 5.13c, f). The electron diffraction pattern taken after the first sodiation (Figure 5.13j) indicates that amount of Na has been accommodated into the EG. The sodiation-induced structure change was also observed by *ex situ* Raman spectra (Figure 5.14). Compared with pristine EG, the intensity ratio between D band and G band becomes more pronounced for sodiated EG, indicating the increment in structure randomness after sodiation.

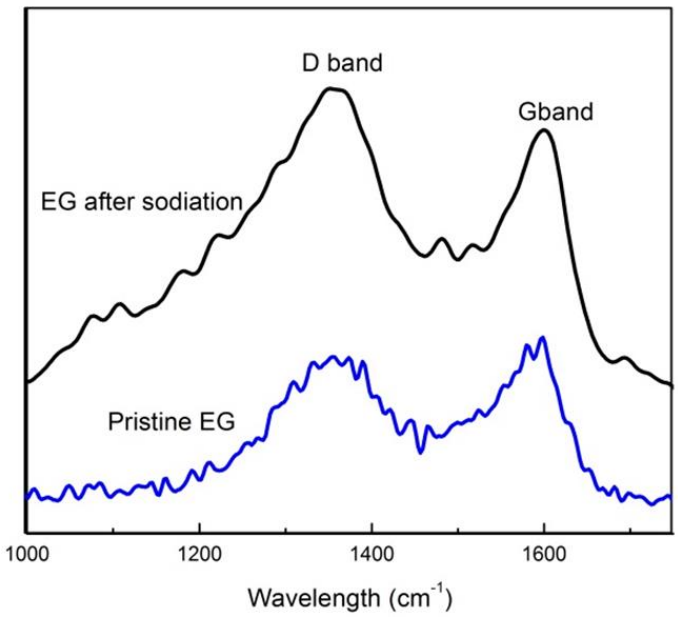

Figure 5.14 Raman profile for pristine EG and EG after sodiation.

When a positive voltage is applied on the EG against the Na electrode, the desodiation process begins. As Na ions migrate out of the EG anode, the microstructure of desodiated EG is reversibly recovered to a parallel layered pattern with long-range ordering (Figure 5.13d, g), and the residual Na ions in EG are found to be negligible as demonstrated by the disappearance of diffraction spots in Figure 5.13k.

It is also noted that, regardless of microstructural reorganization, the layered structure of the material does not exhibit large-scaled distortion throughout the entire reaction, which provides a constant transport space for Na ions. Though the clear reaction front of these electrochemical reactions was not directly imaged, due to insufficient volume change, the actual microstructural distortion and restoration associated with the sodiation and desodiation processes have been readily captured by *in situ* TEM.

It is of great importance that such microstructural evolutions are reversible and reproducible without any mechanical or electrochemical breakdown for the observed six charge/discharge cycles (Figure 5.15, and would also be expected for further cycles according to the excellent cycling performance). Evident from the *in situ* TEM results, the utilization of EG as the NIB anode material exhibits excellent performance attributed to the advantages of the unique and robust long range layered structures.

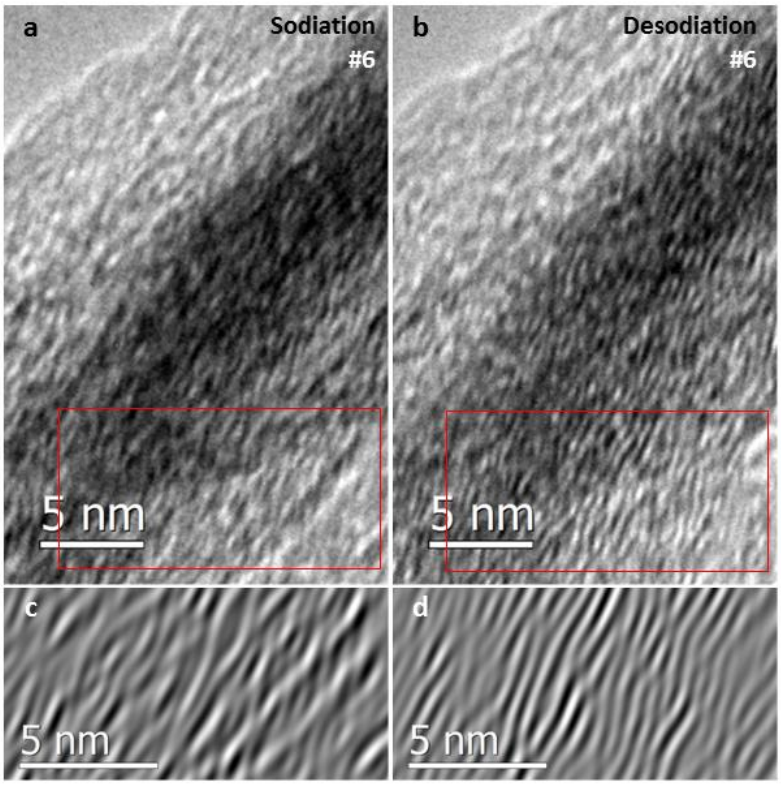

Figure 5.15 TEM images showing typical morphologies of EG (a) after the 6th sodiation cycle and (b) after the 6th desodiation cycle. (c), (d) Filtered TEM close-up images corresponding to the boxed areas in (a) and (b), respectively.

The *in situ* TEM results are consistent with post-mortem HRTEM study of after-cycled EG assembled in coin cells using liquid electrolyte. As shown in the HRTEM image in Supplementary Figure 5.16, after 150 sodiation-desodiation cycles, the EG still exhibits a long-lived layered structure with interlayer distance remaining at 0.42 nm, whereas the other local disordered contrast could be caused by effects of interaction with Na^+ morphologies.

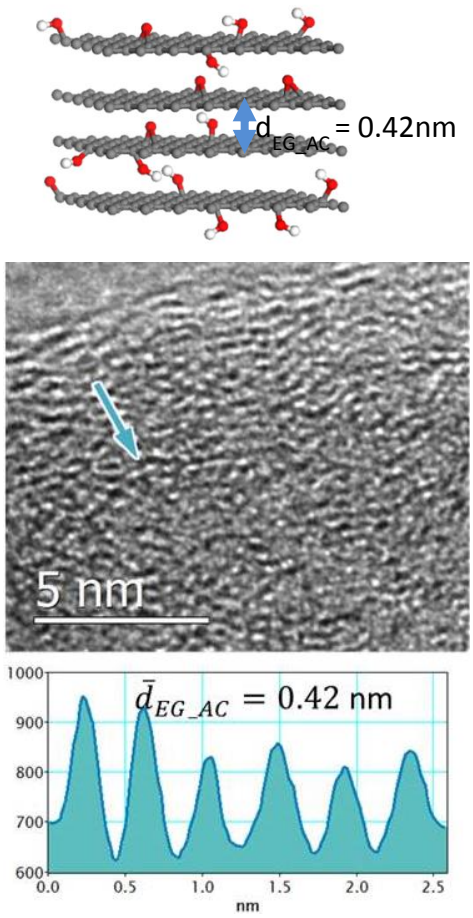

Figure 5.16 HR-TEM image (Contrast profiles along the arrows indicate interlayer spacings) of EG after 150 cycles.

5. 4 Summary

We have successfully developed EG with a long-range-ordered layered structure for NIB anodes. Different from other carbonaceous NIB anodes, EG stores Na^+ mostly by interlayer intercalation, which has been confirmed by cyclic voltammetry and *in situ* TEM observations through reversible interlayer expansion/shrinkage of the EG

material during the sodiation and desodiation. The robustness of the long-range-ordered layered structure of EG during sodiation/desodiation was also revealed by reproducible interlayer changes during multiple charge/discharge processes during *in situ* TEM observation. For practical NIB application, EG can deliver a high reversible capacity of 284 mA g^{-1} at a low current density of 20 mA g^{-1}. Superior capacity retention (73.92% after 2000 cycles) was achieved at fast cycling rate. This fundamental understanding is beneficial for the design and manufacture of rechargeable sodium ion batteries, positioning expanded graphite as a promising anodic material.

5.5 Related References

6 Nagelberg, A. S. & Worrell, W. L. A thermodynamic study of sodium-intercalated TaS_2 and TiS_2. *J. Solid State Chem.* 29, 345-354 (1979).

7 Delmas, C., Braconnier, J.-J., Fouassier, C., & Hagenmuller, P. Electrochemical intercalation of sodium in Na_xCoO_2 bronzes. *Solid State Ionics* 3-4, 165-169 (1981).

106 Molenda, J., Delmas, C. & Hagenmuller, P. Electronic and electrochemical properties of Na_xCoO_{2-y} cathode. *Solid State Ionics* 431-435 (1983).

107 Pascal Ge, M. F. Electrochemical interaction of sodium in graphite. *Solid State Ionics* 28-30, 1172-1175 (1988).

108 Stevens, D. A. & Dahn, J. R. The Mechanisms of Lithium and Sodium Insertion in Carbon Materials. *J. Electrochem. Soc.* 148, A803-A811 (2001).

109 Cao, Y., *et al*. Sodium Ion Insertion in Hollow Carbon Nanowires for Battery Applications. *Nano lETT.* 12, 3783-3787 (2012).

110 Wenzel, S., Hara, T., Janek, J., & Adelhelm, P. Room-temperature sodium-ion batteries: Improving the rate capability of carbon anode materials by templating strategies. *Energy Environ. Sci.* 4, 3342-3345 (2011).

111 Tang, K., *et al*. Hollow Carbon Nanosphere with Superior Rate Capability for Sodium-Based Batteries. *Adv. Energy Mater.* 2, 873-877 (2012).

112 Wang, Y.-X., Chou, S.-L., Liu, H.-K. & Dou, S.-X. Reduced graphene oxide with superior cycling stability and rate capability for sodium storage. *Carbon* 57, 202-208 (2013).

113 Sangster, J. C-Na (Carbon-Sodium) System. *J. Phase Equilib. Deff.* 28, 571-579 (2007).

114 Chen, Q., Hou, S. S. & Schmidt-Rohr, K. A simple scheme for probehead background suppression in one-pulse H-1 NMR. *Solid State Nucl. Magn. Reson.* 26, 11-15 (2004).

115 Ishii, Y., Chimon, S. & Wickramasinghe, N. P. A new approach in 1D and 2D 13C high resolution solid-state NMR spectroscopy of paramagnetic organometallic complexes by very fast magic-angle spinning. *J. Am. Chem. Soc.* 125, 3438-3439 (2003).

116 Wickramasinghe, N. P. *et al.* Progress in 13C and 1H solid-state NMR for paramagnetic systems under very fast MAS. *J. Chem. Phys.* 128, 52210 (2008).

117 Yagi, T., Utsumi, W., Yamakata, M.-a., Kikegawa, T. & Shimomura, O. High-pressure in situ x-ray-diffraction study of the phase transformation from

graphite to hexagonal diamond at room temperature. *Phys. Rev. B* 46, 6031-6039 (1992).

118 Ein-Eli, D. A. a. Y. The Study of Li-Graphite Intercalation Processes in Several Electrolyte Systems Using In Situ X-Ray Diffraction. *J. Electrochem. Soc.* 142, 1746-1752 (1995).

119 Lerf, A., He, H., Forster, M. & Klinowski, J. Structure of Graphite Oxide Revisited. *J. Phys. Chem. B* 102, 4477-4482 (1998).

120 Szabó, T., Berkesi, O., Forgó, P., Josepovits, K., Sanakis, Y., Petridis, D. & Dékány, I. Evolution of Surface Functional Groups in a Series of Progressively Oxidized Graphite Oxides. *Chem. Mater.* 18, 2740-2749 (2006).

121 Campos, M. F., Damasceno, J. C., Machado, R., & Achete, C. A. Auncertainty estimation of lattice parameters measured by x-ray diffraction. *Xviii imeko world congress Metrology for a Sustainable Development* (2006).

122 Xu, B. *et al.* What is the choice for supercapacitors: graphene or graphene oxide? *Energy Environ. Sci.* 4, 2826-2830 (2011).

123 Pierotti, R. A., & Rouquerol, J. Reporting physisorption data for gas/solid systems with special reference to the determination of surface area and porosity. *Pure Appl. Chem.* 57, 603-619 (1985).

124 Ng, S. H. *et al.* Correlations between surface properties of graphite and the first cycle specific charge loss in lithium-ion batteries. *Carbon* 47, 705-712 (2009).

125 Xing, W., Xue, J. S., & Dahn, J. R. Optimizing Pyrolysis of Sugar Carbons for Use as Anode Materials in Lithium-Ion Batteries. *J. Electrochem. Soc.* 143, 3046-3052 (1996).

126 Wang, Y., Alsmeyer, D. C. & McCreery, R. L. Raman Spectroscopy of Carbon Materials: Structural Basis of Observed Spectra. *Chem. Mater.* 2, 557-563 (1990).

127 Cai, W. *et al.* Synthesis and solid-state NMR structural characterization of 13C-labeled graphite oxide. *Science* 321, 1815-1817 (2008).

128 Casabianca, L. B., Shaibat, M., Cai, W., Park, S., Piner, R., Ruoff, R.S., & Ishii, Y. NMR-based structural modeling of graphite oxide using multi-dimensional 13C solid-state NMR and ab-initio chemical shift calculations. *J. Am. Chem. Soc.* 132, 5672-5676 (2010).

129 Gao, W., Alemany, L.B., Ci, L.J., & Ajayan, P.M. New insights into the structure and reduction of graphite oxide. *Nature Chem.* 1, 403-408 (2009).

130 DiVincenzo, D. & Mele, E. Cohesion and structure in stage-1 graphite intercalation compounds. *Phys. Rev. B* 32, 2538-2553 (1985).

131 Gotoh, K., *et al*. NMR study for electrochemically inserted Na in hard carbon electrode of sodium ion battery. *J. Power Sources* 225, 137-140 (2013).

132 Steven, D. A., & Dahn, J. R. High Capacity Anode Materials for Rechargeable Sodium-Ion Batteries. *J. Electrochem. Soc.* 147 (2000).

133 Shao, Y., *et al*. Surface-Driven Sodium Ion Energy Storage in Nanocellular Carbon Foams. *Nano Lett.* 13, 3909-3914 (2013).

134 Zhu, Y. & Wang, C. Galvanostatic Intermittent Titration Technique for Phase-Transformation Electrodes. *J. Phys. Chem.* 114, 2830-2841 (2009).

135 Augustyn, V., *et al*. High-rate electrochemical energy storage through LiC intercalation pseudocapacitance. *Nature Mater.* 12, 518-522 (2013).

136 Ardizzone, S., Fregonara, G. & Trasatti, S. "Inner" and "outer" active surface of RuO_2 electrodes. *Electrochim. Acta* 35, 263-267 (1990).

137 Mochida, I., Ku, C.-H., Yoon, S.-H. & Korai, Y. Anodic performance and mechanism of mesophase-pitch-derived carbons in lithium ion batteries. *J. Power Sources* 75, 214-222 (1998).

138 Liu, N., Wu, H., McDowell, M. T., Yao, Y., Wang, C., & Cui, Y. A yolk-shell design for stabilized and scalable Li-Ion battery alloy anodes. *Nano Lett.* 12, 3315-3321 (2012).

139 Liu, N. *et al.* A pomegranate-inspired nanoscale design for large-volume-change lithium battery anodes. *Nature Nanotech.* 9, 187-192 (2014).

Chapter 6: Conclusion and Future Work

6.1 Conclusions

In this dissertation work, several advanced anode materials were designed and synthesized to target the challenges in current lithium ion batteries and sodium ion batteries developing. In-depth electrochemical analysis was covered to discover the fundamental kinetics and atomic storage mechanism.

For Li-ion batteries, the graphene-bonded and –encapsulated nano-Si anode material was synthesized by a one-step aerosol spray method. The composite reveals good cycling performance and rate capability. More importantly, the simplified synthesis path allows possibility of future commercialization. Detailed study is expected to understand the mechanism behind the cycling stability improvement.

Further attempt on carbon-Si anode development was taken by fabricating carbon nanotubes -bonded and -entangled Si nanoparticles. Different from traditional method in which the Si was physically mixed with or deposited on conductive carbon, the carbon nanotubes framework was grown directly on the well dispersed functionalized Si nanoparticle surface. The nanotubes –bonded and –entangled Si composite shows significantly enhanced conductivity with electrode and ensure the crack free electricity connection along cycling. The loading amount and morphologies of the carbon nanotubes were manipulated by controlling CVD time and the surface oxidation extend of the Si, which allows further engineering of the material in the future.

For Na-ion batteries, to improve the anodic electrode performance, novel expanded graphite was designed and synthesized. Detail kinetic study and atomic scale

observation by *in situ* TEM demonstrated that the expanded graphite can store Na^+ mainly by intercalation reaction in a similar way that graphite stores Li^+. And the robust layer structure ensures long superior long cycling performance. The investigation of expanded graphite as anode material for NIB provides an alternative approach to engineer NIB carbon anodes.

6.2 Potential future work

Potential future work involves further detail fundamental study of known system and exploration of new systems, which are listed as below.

6.2.1 Carbon coated Si-graphene and Si-CNT anodes for LIB

In chapter 3 and 4, graphene-Si and CNT-Si composites were designed and synthesized for LIB anodes. Using of graphene and CNT was proved to be efficiently buffer the volume change of Si anode during lithiation/delithiation process. In the future work, morphology modifications can be carried out to improve the long term stability. As reported in the several researches, capacity fading in the long term performance of Si anode is attributed to the continuous growth of the solid-electrolyte interphase(SEI).[138] Inspired by the recent research on pomegranate structure Si-C anode, [139] future improvement can be done by coating the graphene-Si and CNT-Si particles by a layer of condensed carbon. This layer of carbon shell would act as an electrolyte barrier that would reduce the direct SEI formation on the Si and thus stop the SEI growth during cycling.

6.2.2 Oxygen-content control in expanded graphite

In chapter 5, expanded graphite was synthesized and studied as potential long-cycling NIB anode. In the initial design, the *d* spacing of expanded graphite can be ideally controlled by manipulating the oxygen-containing groups in between the graphene layers. In this dissertation, this hypothesis is proved by comparing the EG-1hr and EG-5hr on both electrochemical performance and morphologies. It is also known that the oxygen-content removal rate would also affect the layer morphology of the material. [140 141]

In future work, more study can be carried out to explore how the oxygen-content removing rate and optimize the oxygen-containing amount in the materials. The experiment can be performed on lower heating rate at various heating rate. Ideally, the optimal balance of oxygen containing amount and the inter layer spacing would allow Na^+ to intercalate into graphene layer in a single atom intercalation behavior that is exactly the same as Li^+ intercalate into graphite, which would allow all the intercalation reaction occur in a generally similar voltage that would facilitate the full cell design and performance.

More detail study can be approached by studying the ambience factor. Since the removal of the oxygen-containing groups would directly affect the *d* spacing in expanded graphite, the reduction ambience would be critical. Reduction experiment in a more reductive ambience, for example, H_2/Ar gas, would result in higher reduction yield in shorter reaction time. It will be interesting to perform a systematic study under different ambience to achieve the optimal condition.

Alternative approach could be taken by finding new oxidation method that would be controlled during oxidation and minimize the layer morphology distortion during layer distance expansion reaction. Modified oxidation method excludes the usage of KMnO4 in the initial oxidation and could significant reduce the oxygen concentration. [142] By carefully manipulate the initial oxidization process, the reduction step can be omitted. The expanded graphite can be produced in a one-step reaction which would significantly benefit future commercialization. Moreover, the distortion and the defects sites in expanded graphite can be dramatically reduced. This would not only improve the electronic conductivity in a great extent, but more importantly, would be able to achieve better long range layered structure, which would be idealize for Na^+ intercalation.

6.2.3 Red phosphorous as anode for Na-ion batteries.In the previous chapter, we have discussed the expanded graphite, a typical soft carbon material as anode for Na-ion batteries. Even though the cycling performance is great, the capacities for hard/soft carbon anodes are generally low (~200mAh g-1). Element phosphorous (P) is a particular attractive anode material for NIB since red phosphorus is earth abundant and eco-friendly material. The existent of stable phase of Na_3P brings the theoretical capacity of P to as high as 2355 mAh g^{-1}. The main drawback of red phosphorus as NIB anode is that phosphorus is electronic insulation. Similar to red P anode in LIB, the pure red P reveals a much lower experimental capacity that theoretical value with fast fading.[17] Earlier, Kim *et al.*[143] and Qian *et al.*[144] reported the amorphous red phosphorous/ carbon composites as Na-ion battery anode. In these two publications, red phosphorus was mixed with conductive carbon by high energy ball-milling to

form amorphous phosphorus/carbon composite. However, even though it was proved that P is able to store large amount of Na^+, the reported P-carbon composites reveal moderate cycling stability. Wang *et al.* reported nano-structured phosphorus composite by vaporization/adsorption method for Li-ion battery, revealing good cycling stability as anode for LIB.[140] Following the same idea as using mesoporous carbon as frame work to improve the electronic conductivity in sulfur cathode,[145] the nano red phosphorus was deposited on porous carbon. However, similar method has not yet been used for NIB anode synthesis.

In the future work, the gas phase deposition synthesis technique can be utilized to fabricate P-carbon composite, targeting on more stable P-carbon NIB anode. The idea is to confine phosphorus particles within small pores in carbon framework including mesoporous carbon and carbon nanotubes. In the preliminary experiments, different types of carbon host, including porous carbon and carbon nanotubes with different diameters, were used. The result was compared mainly based on the electrochemical cycling stability.

To compare the effect of the morphology of carbon host, as long as the pores size/inner diameters of the carbon frame work materials, meso porous (with pore size of ~3.5 nm) and carbon nanotubes with different inner diameters (MWCNT at ~30nm, SWCNT at ~1.5 nm and DWCNT at ~2nm) were used as carbon host.

In a typical synthesis process, red phosphorus powder (> 99.99% trace metals basis, Sigma Aldrich) was mixed with carbon material (porous carbon, homemade; multiwall carbon nanotubes, Nanostructured & Amorphous Material, Inc.; single wall carbon nanotubes, Nanostructured & Amorphous Material, Inc.; double wall carbon

nanotubes, Nanostructured & Amorphous Materials, Inc.) in a 1:2 mass ratio. The powder was firstly mixed by hand milling for ~30min. Upon well mixing, the mixture was then transferred into quartz tube. The quartz tube was vacuumed and sealed before heat treatment. In a typical annealing process, the sealed quartz tube with mixed precursor materials was heated up in 5 ºC/min to 600 ºC. The temperature was maintained at 600 ºC for 5 hr, and then cooled down to 280 ºC. The sample was hold at 280 ºC for 24hr before it is naturally cooled down to room temperature. The final powder materials were collected for further characterization.

The morphology of the Carbon-P composite was characterized by scanning electron microscopy (SEM) in the University of Maryland Nanocenter. In a typical SEM observation experiment, powder samples were glued onto the SEM sample holder by conductive carbon tape.

Electrochemical testing carbon-P electrodes were prepared by the slurry coating method. The active material was mixed with 15 wt% binder (PVDF) and 10% of carbon black, and milled for 30 minutes to form a slurry. Then, the obtained slurry was cast on copper foil and dried in a vacuum oven at 100 °C overnight. The loading amount of active material was ~ 0.2mg cm^{-2}. Coin cells, consisting of a carbon-P working electrode, a lithium metal counter electrode, Celgard 3501 separator, and 1.0 M $NaClO_4$ in dimethyl carbonate (DMC) : fluoroethylene carbonate (FEC) (1:1) co-solvent liquid electrolyte, were assembled in an argon-filled glove box for electrochemical tests.

Galvanostatic charge/discharge was performed using an Arbin test station. Cells were cycled between 0V and 2 V at different currents. After the cell reached the cut off

voltages, it was relaxed for 10 mins before subsequent charge or discharge. Cyclic voltammetry (CV) test with voltage ranging from 0 V to 2 V was performed at a scan rate of 0.1 mV s^{-1} using a Solatron 1260/1287 Electrochemical Interface (Solatron Metrology, UK).

For the rate capability tests, cells were pre-cycled for 20 cycles for activation and then charged-discharged at various C rates between 0 V and 2 V. The capacity is calculated based on the overall mass of carbon/phosphorus.

Scanning electron microscopy (SEM) was carried out for morphology observation.

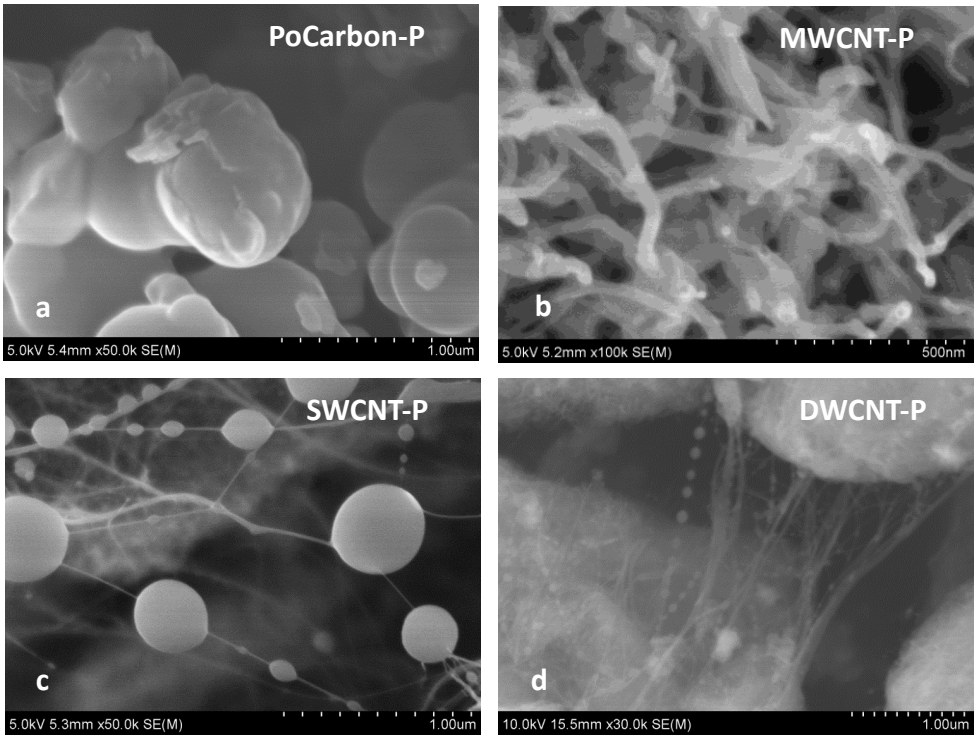

Figure 6.1 SEM images of (a) PoCarbon-P with 50k magnification, (b) MWCNT-P with 100k magnification, (c) SWCNT-P with 50k magnification and (d) DWCNT-P with 30k magnification.

Figure 6.1 shows the image of P @ porous carbon (PoCarbon-P), P @ carbon nanotubes (SWCNT-P, DWCNT-P and MWCNT-P).

In the images of PoCarbon-P (Figure 6.1a) and MWCNT-P (Figure 6.1b), there is no significant sigh show that P exists on the outer surface of the material. Details analysis need be done by XRD-EDS in the future to verify this information. Possible explanation could be that the special inner of the material provide sufficient accommodation of the loaded P. Comparing to the SWCNT and DWCNT that with smaller inner diameter, it is kinetically more feasible for P to get into the carbon host in PoCarbon and MWCNT.

On the other hand, interestingly, considerable amount of the P was observed on the outer surface of the carbon host in SWCNT (Figure 6.1c) and DWCNT (Figure 6.1d) to form this beaded-string morphology. Same morphology was also found in the Si-CNT composite reported by Sun et al.[146] in which the defects on the carbon nanotubes serves as nucleation centers for Si to grow on. Similar growth mechanism could also occur during the P deposition on SWCNT and DWCNT.

The electrochemical performance of the P-carbon composites was firstly evaluated be cycling performance. The cells consist of working electrode made of PoCarbon-P, MWCNT-P, SWCNT-P and DWCNT-P were cycled between 0-2V at current density of 250 mA g^{-1}. And the cycling performance of the first 30 cycles is shown in Figure 6.2.

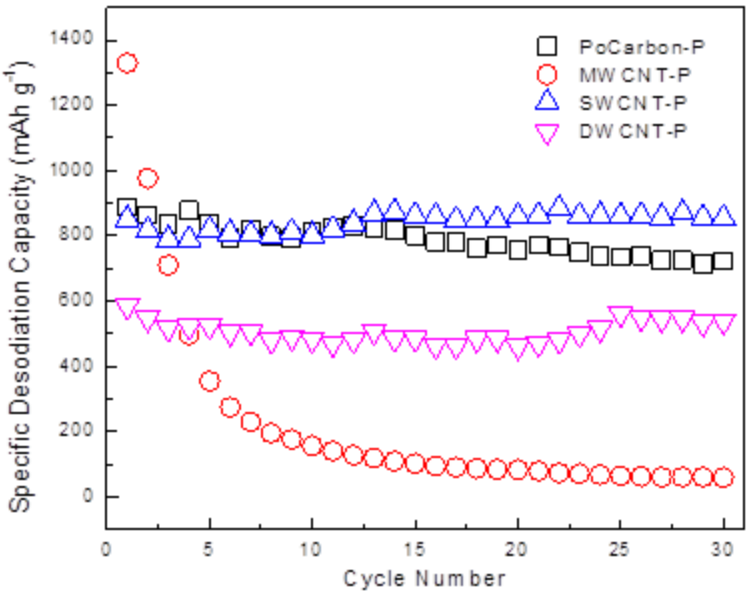

Figure 6.2 Short term cycling performance for PoCarbon-P, SWCNT-P, DWCNT-P and MWCNT-P at current density of 250mA g^{-1}.

It is interesting to see that with significantly larger inner diameter size than the other three carbon host materials, multi-wall carbon nanotubes reveal poorer ability on the improvement of the cycling stability of P anode. On the other hand, porous carbon and carbon nanotubes with pore size/inner diameter < 3.5 nm shows significant improvement on stabilizing the P anode in the first 30 cycles.

The long term cycling performance test were carried out to study the cycling ability of PoCarbon-P, SWCNT-P and DWCNT-P. In the initial 2 cycles, low current density of 50 mA g^{-1} was used to ensure full sodiation/desodiation of material. Comparatively high current density of 250 mA g^{-1} was used in the following cycles to achieve long cycling data in a reasonable time frame. And the cycling profiles for PoCarbon-P,

SWCNT-P and DWCNT-P are shown in Figure 6.3. Figure 6.4 and Figure 6.5, respectively.

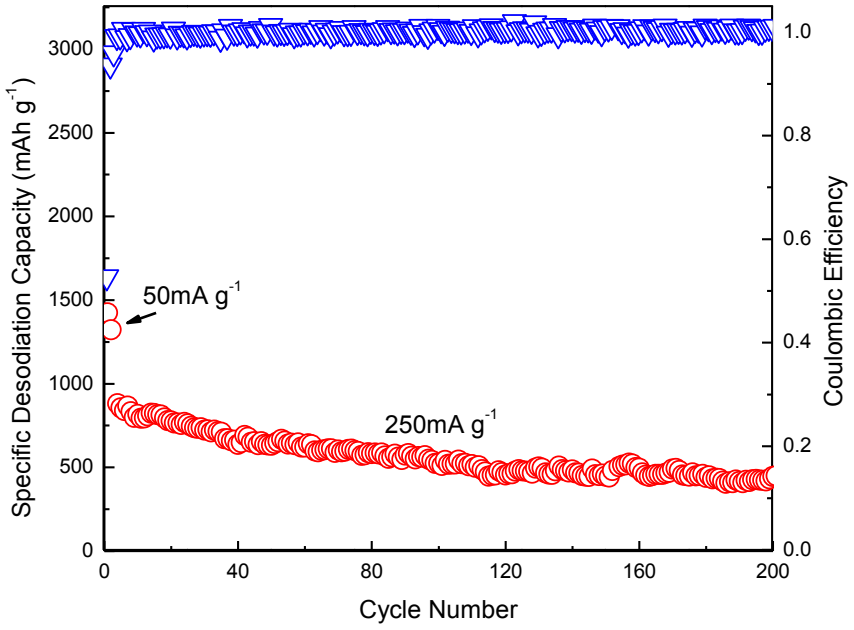

Figure 6.3 Cycling performance of PoCarbon-P vs Na/Na^+ up to 200 cycles.

While PoCarbon-P reveals a gradually decreasing profile and retains only ~ 49.8% of the capacity as in 3rd cycle, both SWCNT-P and DWCNT-P shows good long term cycling stability. The SWCNT-P shows a small increase on capacity at the initial cycles and retains ~100% of the capacity as in the 3rd cycle, while the capacity retention of DWCNT-P after 270 cycles is around 71%. It is obvious that SWCNT and DWCNT work differently than PoCarbon functioning as frame works, which allow more stable cycling in the long term. Possible explanation is that the beaded-string morphology of SWNT-P and DWNT-P contribute to the constraining the Si particles and maintaining crack-free electrical connection during

lithiation/delithiation process.[146] Suffering from the same pulverization problem induced by significantly volume change as Si, P anode could be potentially benefitial from the beaded-string structure.

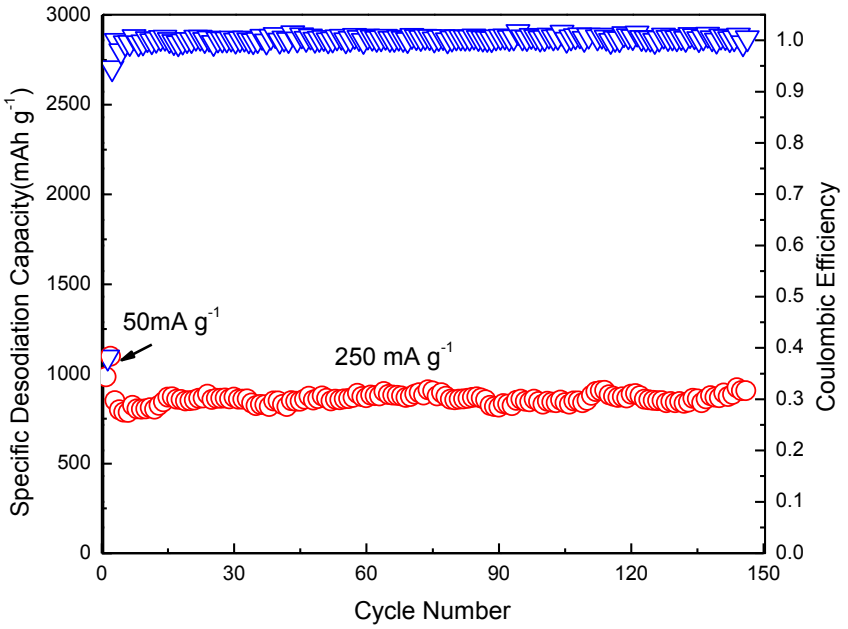

Figure 6.4 Cycling performance of SWCNT-P vs Na/Na^+ up to 146 cycles.

The first cycle coulombic efficiencies of all samples are around 40%-50%. The general low first cycle coulombic efficiency could be due to the large amount of the solid-electrolyte interphase (SEI) formation. It could be potentially improved by reduce the solid- electrolyte interaction area.

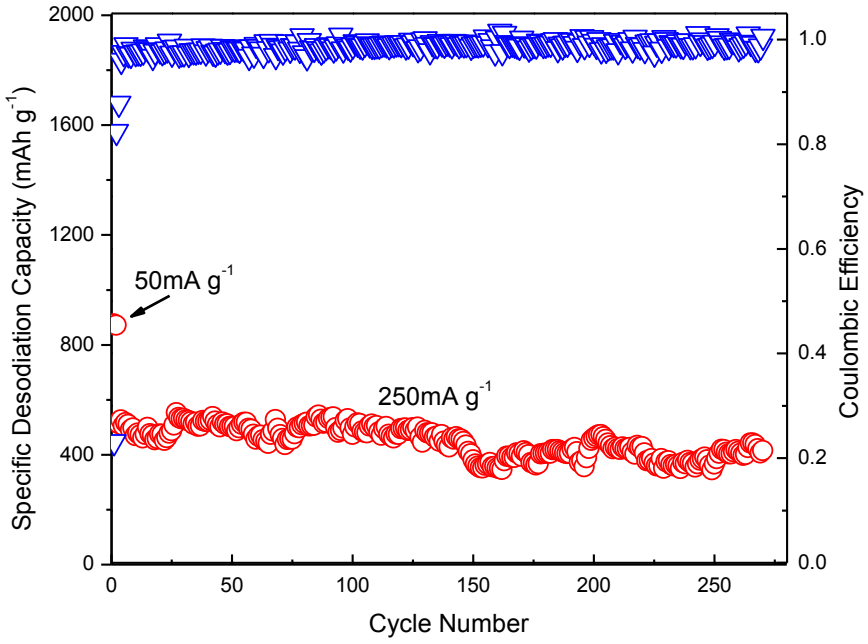

Figure 6.5 Cycling performance of DWCNT-P vs Na/Na^+ up to 270 cycles.

In summary of the preliminary data, the red phosphorus/carbon composites were synthesized through vaporization/deposition methods and studied as anode for NIB. Several different type of carbon frame work materials were used as carbon host. SWCNT and DWCNT were proved to have the superior ability to stabilized P anode. The potential reason is that, instead of confine the phosphorus in small pores/tubes, the beads-on-tubes morphology allows stronger interaction between carbon and phosphorus, and more enhancements on the electronic conductivity during sodiation/desodiaiton process.

More fundamental studies are expected in the future to understand the mechanism behind the superior cycling performance of SWCNT-P and DWCNT-P towards Na/Na^+.

The morphology of the material need to be further studied by transition electron microscopy (TEM). Getting detail elemental information within the meso pores/nanotubnes as well as on the surface of the carbon frames would be beneficial to further discuss the connection between structures and electrochemical performance. To better know the interaction between SWNT-P, DWNT-P and Na^+, atomic scale observation such like XPS and in situ TEM are highly recommended to get direct interaction information. The Na^+ storage mechanism can be interpreted by analyzing the P-Na interaction by XPS. It is possible that this interaction is different in the SWCNT-P and DWCNT-P than other carbon-P composites, which is the direct reason behind long cycling stability. On the other hand, since large amount of volume change is expected, in situ TEM could serve the purpose of probing the real time sodiation/disodiation behavior of the material. Also, to study the formation mechanism, defect engineering could be carried out to manipulate the beaded-string morphology to achieve the optimal structure.

6.2.4 Phosphide as anode for Na-ion batteries

As an extension on the phosphorus species as anode material for NIB, phosphides are also attractive candidates for high energy density NIB fabrication.

It is reported that Sn_4P_3 can store Na^+ through alloying/de-alloying reaction of Na_3P and $Na_{15}Sn_4$, as shown below in equations (7.1) and (7.2). [147,148]

$$Na_{15}Sn_4 \leftrightarrow 4Sn + 15Na \quad (7.1)$$

$$Na_3P \leftrightarrow P + 3Na \quad (7.2)$$

This would bring to an enormous Na-storage capacity. The typical drawback of the material is the significant volume change (~525% volume expansion from Sn to

$Na_{15}Sn_4$ and ~490% volume change from P to Na_3P) during cycling which would lead to continuous pulverization.[147] Current studies mainly use ball-milling to synthesize Sn_4P_3 and mix it with high conductive carbon. However, no reactions were taken to prevent the pulverization or improve the continuity of electronic conductivity during cycling. In the future study, various methods such as electron spinning and aerosol pyrolysis can be utilized to fabricate Sn_4P_3/carbon composites, targeting on long cycling Sn_4P_3 anode.

On the other hand, phosphides like antimony phosphide (SbP) and indium phosphide (InP) are also expected to form stable phases while reacting with Na^+. Thus similar alloy and de-alloy reactions can also be expected and SbP and InP can potentially be good alternatives for NIB anode materials.

6.3 Related references

17 Tarascom, J.-M. & Armand, M. Issues and challenges facing rechargeable lithium batteries. *Nature* 414, 359-367 (2001).

140 Wang, L. *et al.* Nano-Structured Phosphorus Composite as High-Capacity Anode Materials for Lithium Batteries. *Angew. Chem. Int. Ed.* 51, 9034-9037 (2012).

141 Palomares, V. *et al.* Na-ion batteries, recent advances and present challenges to become low cost energy storage systems. *Energy Environ. Sci.* 5, 5884-5901 (2012).

142 Kim, S. W., Seo, D. H., Ma, X., Ceder, G. & Kang, K. Electrode Materials for Rechargeable Sodium-Ion Batteries: Potential Alternatives to Current Lithium-Ion Batteries. *Adv. Energy Mater.* 2, 710-721 (2012).

143 Kim, Y. et al. An Amorphous Red Phosphorus/Carbon Composite as a Promising Anode Material for Sodium Ion Batteries. Adv. Mater. 25, 3045-3049 (2013).

144 Qian, J., Wu, X., Cao, Y., Ai, X. & Yang, H. High capacity and rate capability of amorphous phosphorus for sodium ion batteries. *Angewandte Chemie* 125, 4731-4734 (2013).

145 Ji, X., Lee, K. T. & Nazar, L. F. A highly ordered nanostructured carbon–sulphur cathode for lithium–sulphur batteries. *Nature mater.* 8, 500-506 (2009).

146 Sun, C.-F., *et al*. A Beaded-String Silicon Anode. *ACS Nano* 7, 2717-2724 (2013).

147 Qian, J., Xiong, Y., Cao, Y., Ai, X. & Yang, H. Synergistic Na-Storage Reactions in Sn4P3 as a High-Capacity, Cycle-stable Anode of Na-Ion Batteries. *Nano lett.*14, 1865-1869 (2014).

148 Li, W. *et al.* $Sn_{4+x}P_3$@ Amorphous Sn-P Composites as Anodes for Sodium-Ion Batteries with Low Cost, High Capacity, Long Life, and Superior Rate Capability. *Adv.Mater.* (2014).

Bibliography

1 Jasinski, R. High-energy Batteries. *Plenum Press, New York* (1967).

2 Steele, B. C. H. in Fast Ion Transport in Solids (ed. Van Gool, W.) 103-109 (1973).

3 Armand, M. B. in Fast Ion Transport in Solids (ed. Van Gool, W.) 665–673 (1973).

4 Dunn, B., Kamath, H., & Tarascon, J.-M. Electrical Energy Storage for the Grid: A Battery of Choices. *Science* 334, 928-935 (2011).

5 Whittingham, M. S. chemistry of intercalation compounds metal guests in chalcogenide hosts. *Prog. Solid St. Chem.* 12, 41-99 (1978).

6 Nagelberg, A. S. & Worrell, W. L. A thermodynamic study of sodium-intercalated TaS_2 and TiS_2. *J. Solid State Chem.* 29, 345-354 (1979).

7 Delmas, C., Braconnier, J.-J., Fouassier, C., & Hagenmuller, P. Electrochemical intercalation of sodium in Na_xCoO_2 bronzes. *Solid State Ionics* 3-4, 165-169 (1981).

8 Shacklette, L. W., Jow, T. R. & Townsend, L. Rechargeable electrodes from sodium cobalt bronzes. *J Electrochem Soc* 135, 2669-2674 (1985).

9 Tarascon, J.-M. & Hull, G. Sodium intercalaction into the layered oxides Na_xMoO_4. *Solid State Ionics* 22, 85-96 (1986).

10 Jow, T. R., Shacklette, L., Maxfield M &Vernick D. The role of conductive polymers in alkali-metal secondary electrodes. *J Electrochem Soc* 134, 1730-1733 (1987).

11 West, K, Zachau-Christiansenm, B., Jacobsen, T. & Skaarup, S. Sodium insertion in vanadium oxides. *Solid State Ionics* 30, 1128-1131 (1988).

12 Slater, M. D., Kim, D., Lee, E., & Johnson, C. S. Sodium-Ion Batteries. *Adv. Funct. Mater.* 23, 947-958 (2013).

13 Komaba, S. *et al.* Electrochemical Na Insertion and Solid Electrolyte Interphase for Hard-Carbon Electrodes and Application to Na-Ion Batteries. *Adv.Func. Mater.* 21, 3859-3867 (2011).

14 E. Fitzer, K.-H. K., H. P. Boehm, H. Marsh. Recommended terminology for the description of carbon as a solid (IUPAC Recommendations 1995). *Pure and Applied Chemistry* 67, 473-506 (2009).

15 Novoselov, A. K. G. a. K. S. The rise of graphene. *Nature Mater.* 6, 183-191 (2007).

16 Kang, B. & Ceder, G. Battery materials for ultrafast charging and discharging. *Nature* 458, 190-193 (2009).

17 Tarascom, J.-M. & Armand, M. Issues and challenges facing rechargeable lithium batteries. *Nature* 414, 359-367 (2001).

18 Simon, P. & Gogotsi, Y. Materials for electrochemical capacitors. *Nature mater.* 7, 845-854 (2008).

19 Pierson, H. O. *Handbook of carbon, graphite, diamonds and fullerenes: processing, properties and applications*. (William Andrew, 1994).

20 Fauteux, D. & Koksbang, R. Rechargeable lithium battery anodes: alternatives to metallic lithium. *J. Appl. electrochem.* 23, 1-10 (1993).
21 Winter, M., Besenhard, J. O., Spahr, M. E. & Novak, P. Insertion electrode materials for rechargeable lithium batteries. *Adv. mater.* 10, 725-763 (1998).
22 Aurbach, D. *et al.* The Study of Electrolyte Solutions Based on Ethylene and Diethyl Carbonates for Rechargeable Li Batteries II. Graphite Electrodes. *J.of Electrochem. Soc.* 142, 2882-2890 (1995).
23 Ein-Eli, Y. Dithiocarbonic anhydride (CS_2)—a new additive in Li-ion battery electrolytes. *J. Electroanal. Chem.*531, 95-99 (2002).
24 Bok, H. K. & Oh, S. M. Electrochemical activation of expanded graphite electrode for electrochemical capacitor. *J. Electrochem. Soc.* 155, A685-A692 (2008).
25 A. H. Castro Neto, F. G., N. M. R. Peres, K.S. Novoselov, A.K. Geim. The Electronic Properties of Graphene. *Rev. Mod. Phys.* 81, 109-162 (2009).
26 Sasha Stankovich, D. A. D., Geoffrey H. B. Dommett, Kevin M. Kohlhaas, Eric J. Zimney, Eric A. Stach, Richard D. Piner, SonBinh T. Nguyen and Rodney S. Ruoff. Graphene-based Composite Materials. *Nature* 442, 282-286 (2006).
27 Novoselov, K. S. *et al.* Electric field effect in atomically thin carbon films. *science* 306, 666-669 (2004).
28 Zhao, W. *et al.* Preparation of graphene by exfoliation of graphite using wet ball milling. *J. Mater. Chem.* 20, 5817-5819 (2010).
29 Hummers JR, W.S. & Offeman, R. E. Preparation of Graphitic Oxide. *J. Am. Chem. Soc.* 80, 1339-1339 (1957).
30 Wu, Z.-S. *et al.* Graphene anchored with Co3O4 nanoparticles as anode of lithium ion batteries with enhanced reversible capacity and cyclic performance. *ACS nano* 4, 3187-3194 (2010).
31 Zhou, G. *et al.* Graphene-wrapped Fe3O4 anode material with improved reversible capacity and cyclic stability for lithium ion batteries. *Chem. Mater.* 22, 5306-5313 (2010).
32 Wang, H. *et al.* Mn3O4− graphene hybrid as a high-capacity anode material for lithium ion batteries. *J. Am. Chem. Soc.* 132, 13978-13980 (2010).
33 Yoo, E. *et al.* Large reversible Li storage of graphene nanosheet families for use in rechargeable lithium ion batteries. *Nano Lett.* 8, 2277-2282 (2008).
34 Wang, H. *et al.* Graphene-wrapped sulfur particles as a rechargeable lithium–sulfur battery cathode material with high capacity and cycling stability. *Nano lett.* 11, 2644-2647 (2011).
35 Wang, D. *et al.* Self-assembled TiO2–graphene hybrid nanostructures for enhanced Li-ion insertion. *ACS nano* 3, 907-914 (2009).
36 Su, D., Ahn, H. J. & Wang, G. SnO_2@graphene nanocomposites as anode materials for Na-ion batteries with superior electrochemical performance. *Chem. Commun.* 49, 3131-3133 (2013).
37 Zhu, H. *et al.* Free-standing $Na_{2/3}Fe_{1/2}Mn_{1/2}O_2$@graphene film for a sodium-ion battery cathode. *ACS appl. Mater. Interfaces* 6, 4242-4247 (2014).

38 Wang, Y.-X. *et al.* Ultrafine SnO_2 nanoparticle loading onto reduced graphene oxide as anodes for sodium-ion batteries with superior rate and cycling performances. *J. Mater.Chem. A* 2, 529-534 (2014).
39 Fan, Q., Lei, L., Yin, G., Chen, Y. & Sun, Y. Direct growth of $FePO_4$/graphene hybrids for Li-ion and Na-ion storage. *Electrochemistry Communications* 38, 120-123 (2014)
40 Ling, C. & Mizuno, F. Boron-doped graphene as a promising anode for Na-ion batteries. *Phys. Chem. Chem. Phys.* 16, 10419-10424 (2014).
41 Su, D., Dou, S. & Wang, G. WS_2@graphene nanocomposites as anode materials for Na-ion batteries with enhanced electrochemical performances. *Chem. Commun.* 50, 4192-4195 (2014).
42 Pang, G. *et al.* Synthesis of NASICON-type structured $NaTi_2(PO_4)_3$-graphene nanocomposite as an anode for aqueous rechargeable Na-ion batteries. *Nanoscale.* 6, 6328-6334 (2014).
43 Zhang, Y. *et al.* Activation of electrochemical lithium and sodium storage of nanocrystalline antimony by anchoring on graphene via a facile in situ solvothermal route. *J. Power Sources* 247, 204-212 (2014).
44 Iijima, S. Helical microtubules of graphitic carbon. *Nature* 354, 56-58 (1991).
45 Reddy, A. L. M., Shaijumon, M. M., Gowda, S. R. & Ajayan, P. M. Coaxial MnO_2/carbon nanotube array electrodes for high-performance lithium batteries. *Nano Lett.* 9, 1002-1006 (2009).
46 Che, G., Lakshmi, B. B., Fisher, E. R. & Martin, C. R. Carbon nanotubule membranes for electrochemical energy storage and production. *Nature* 393, 346-349 (1998).
47 Zhang, Y. *et al.* Composite anode material of silicon/graphite/carbon nanotubes for Li-ion batteries. *Electrochim. Acta* 51, 4994-5000 (2006).
48 Li, X., Kang, F., Bai, X. & Shen, W. A novel network composite cathode of $LiFePO_4$/multiwalled carbon nanotubes with high rate capability for lithium ion batteries. *Electrochem. Commun.* 9, 663-666 (2007).
49 Morris, R. S., Dixon, B. G., Gennett, T., Raffaelle, R. & Heben, M. J. High-energy, rechargeable Li-ion battery based on carbon nanotube technology. *J. Power Sources* 138, 277-280 (2004).
50 Chen, J. *et al.* Flexible, aligned carbon nanotube/conducting polymer electrodes for a lithium-ion battery. *Chem. mater.* 19, 3595-3597 (2007).
51 Shu, J., Li, H., Yang, R., Shi, Y. & Huang, X. Cage-like carbon nanotubes/Si composite as anode material for lithium ion batteries. *Electrochem. commun.* 8, 51-54 (2006).
52 Cui, L.-F., Hu, L., Choi, J. W. & Cui, Y. Light-weight free-standing carbon nanotube-silicon films for anodes of lithium ion batteries. *Acs Nano* 4, 3671-3678 (2010).
53 de las Casas, C. & Li, W. A review of application of carbon nanotubes for lithium ion battery anode material. *J. Power Sources* 208, 74-85 (2012).
54 Landi, B. J., Ganter, M. J., Cress, C. D., DiLeo, R. A. & Raffaelle, R. P. Carbon nanotubes for lithium ion batteries. *Energy Env. Sci.* 2, 638-654 (2009).

55 Johan, C. & Rydha, B. S. Impact on global metal flows arising from the use of portable rechargeable batteries. *Sci. Total Environ.* 302, 167-184 (2003).
56 Hideto Azuma), H. I., Shin'ichiro Yamada, Koji Sekai. Advanced carbon anode materials for lithium ion cells. *J. Power Sources* 81-82, 1-7 (1999).
57 Dahn, J. D., Zheng, T., Liu, Y.-H. & Xue, J. S. Mechanisms for Lithium Insertion in Carbonaceous Materials. *Science* 270, 590-593 (1995).
58 Armand, M. & Tarascon, J. M. Building better batteries. *Nature* 451, 652-657 (2008).
59 Holzapfel, M., Buga, H., Scheifele, W., Novák, P. & Petrat, F.-M. A new type of nano-sized silicon/carbon composite electrode for reversible lithium insertion. *Chem.Commun.* 1566-1568 (2005).
60 Cheol-Min Park, J.-H. K., Hansu Kim and Hun-Joon Sohn. Li-alloy based anode materials for Li secondary batteries. *Chem. Soc. Rev.* 39, 3115-3141 (2010).
61 Park, S. II, Gocheva, I., Okada, S. & Yamaki, J.-I. Yamaki. Electrochemical properties of $NaTi_2(PO_4)_3$ anode for rechargeable Aqueous sodium-ion batteries. *J. Electrochem. Soc.* 158, A1067-A1070 (2011).
62 Senguttuvan, P., Rousse, G., Seznec, V., Tarascon, J.-M. & Palacín, a. M. R. $Na_2Ti_3O_7$: Lowest Voltage Ever Reported Oxide Insertion Electrode for Sodium Ion Batteries. *Chem. Mater.* 23, 4109-4111 (2011).
63 Liua, H., Zhou, H., Chena, L., Tanga, Z., & Yang, W. Electrochemical insertion/deinsertion of sodium on NaV_6O_{15} nanorods as cathode material of rechargeable sodiumbased batteries. *J. Power Sources* 196, 814-819 (2011).
64 Ellis, B. L. & Nazar, L. F. Sodium and sodium-ion energy storage batteries. *Curr. Opin. Solid State Mater. Sci.* 16, 168-177 (2012).
65 Chen, J. & Cheng, F. Combination of Lightweight Elements and Nanostructured Materials for Batteries. *Acc. Chem. Res.* 42, 713-723 (2009).
66 Goodenough, J. B., & Kim, Y. Challenges for Rechargeable Li Batteries. *Chem. Mater.* 22, 587-603 (2010).
67 Li, H., Wang, Z., Chen, L. & Huang, X. Research on Advanced Materials for Li-ion Batteries. *Adv.Mater.* 21, 4593–4607 (2009).
68 Poizot, P., Laruell, S., Grugeon, S., Dupont, L. & Tarascon, J.-M. Searching for new anode materials for the Li-ion technology: time to deviate from the usual path. *J. Power Sources* 97-98, 235-239 (2001).
69 Liu, H. K., Guo, Z. P., Wang, J. Z., & Konstantinov, K. Si-based anode materials for lithium rechargeable batteries. *J. Mater. Chem.* 20, 10055-10057 (2010).
70 Chou, S. L., Wang, J. Z., Choucair, M., Liu, H. K., Stride, J. A., & Dou, S. X. Enhanced reversible lithium storage in a nanosize silicon/graphene composite. *Electrochem. Commun.* 12, 303-306 (2010).
71 Lee, J. K., Smith, K. B., Hayner, C. M. & Kung, H. H. Silicon nanoparticles–graphene paper composites for Li ion battery anodes. *Chem. Commun.* 46, 2025-2027 (2010).
72 Tao, H.-C., Fan, L.-Z., Mei, Y. & Qu, X. Self-supporting Si/Reduced Graphene Oxide nanocomposite films as anode for lithium ion batteries. *Electrochem. Commun.* 13, 1332-1335 (2011).

73 Zhao, X., Hayner, C. M., Kung, M. C. & Kung, H. H. In-Plane Vacancy-Enabled High-Power Si–Graphene Composite Electrode for Lithium-Ion Batteries. *Adv. Energy Mater.* 1, 1079-1084 (2011).
74 Luo, J., Zhao, X., Wu, J.-S., Jang, H. D., Kung, H. H. & Huang, J. Crumpled Graphene-Encapsulated Si Nanoparticles for Lithium Ion Battery Anodes. *J. Phys. Chem. Lett.* (2012).
75 Gómez-Navarro, C., et al. Atomic Structure of Reduced Graphene Oxide. *Nano Lett.* 10, 1144-1148 (2010).
76 Erickson, K., Erni, R., Lee, Z., Alem, N., Gannett, W., & Zettl, A. Determination of the Local Chemical Structure of Graphene Oxide and Reduced Graphene Oxide. *Adv. Mater.* 22, 4467-4472 (2010).
77 Ma, X., Zachariah, M. R. & Zangmeister, C. D. Crumpled nanopaper from graphene oxide. *Nano lett.* 12, 486-489 (2011).
78 Zangmeister, C. D., Ma, X. & Zachariah, M. R. Restructuring of graphene oxide sheets into monodisperse nanospheres. *Chem. Mater.* 24, 2554-2557 (2012).
79 Ma, X., Zachariah, M. R. & Zangmeister, C. D. Reduction of suspended graphene oxide single sheet nanopaper: the effect of crumpling. *J. Phys. Chem. C* 117, 3185-3191 (2013).
80 Si, Y. & Samulski, E. T. Synthesis of Water Soluble Graphene. *Nano Lett.* 8, 1679-1682 (2008).
81 Guo, H.-L., Wang, X.-F., Qian, Q.-Y., Wang, F.-B. & Xia, X.-H. A Green Appraoch to the Synthesis of Graphene Nanosheets. *ACS Nano* 3, 2653-2659 (2009).
82 Lee, Y. M., Lee, J. Y., Shim, H.-T., Lee, J. K. & Park, J,-K. SEI Layer Formation on Amorphous Si Thin Electrode during Precycling. *J. Electrochem. Soc.* 154, A515-A519 (2007).
83 McArthur, M. A., Trussler, S. & Dahn, J. R. In Situ Investigations of SEI Layer Growth on Electrode Materials for Lithium-Ion Batteries Using Spectroscopic Ellipsometry. *J. Electrochem. Soc.* 159, A198-A207 (2012).
84 Zhou, X., Yin, Y.-X., Wan, L.-J. & Guo, Y.-G. Facile synthesis of silicon nanoparticles inserted into graphene sheets as improved anode materials for lithium-ion batteries. *Chem. Commun.* 48, 2198-2200 (2012).
85 Wang, W. & Kumta, P. N. Nanostructured Hybrid Silicon/Carbon Nanotube Heterostructures: Reversible High-Capacity Lithium-Ion Anodes. *ACS Nano* 4, 2233-2241 (2010).
86 Su, J.-F., Huang, Z., Yuan, X.-Y., Wang, X.-Y. & Li, M. Structure and properties of carboxymethyl cellulose/soy protein isolate blend edible films crosslinked by Maillard reactions. *Carbohydr. Polym.* 79, 145-153 (2010).
87 Ichiura, H., Kaneda, Y. & Ohtani, Y. Functional geraniol-Ca (OH) 2 composite/sodium acetate alginate film on nonwoven polyethylene sheet: acetic acid gas production in response to acid. *J. Mater. Sci.* 45, 1343-1349 (2010).
88 Kovalenko, I., *et al*. A Major Constituent of Brown Algae for Use in High-Capacity Li-Ion Batteries. *Science* 334, 75-79 (2011).

89 Bridel, J. S., Azais, T., Morcrette, M., Tarascon, J. M. & Larcher, D. Key Parameters Governing the Reversibility of Si/Carbon/CMC Electrodes for Li-Ion Batteries. *Chem. Mater.* 22, 1229-1241 (2009).

90 Mazouzi, D., Lestriez,, B., Roué, L. & Guyomard, D. Silicon Composite Electrode with High Capacity and Long Cycle Life. *Electrochem. Solid-State Lett.* 12, A215-A218 (2009).

91 Shi, H., Barker, J., Saidi, M. & Koksbang, R. Structure and lithium intercalation properties of synthetic and natural graphite. *J. Electrochem. Soc.* 143, 3466-3472 (1996).

92 Idota, Y., Kubota, T., Matsufuji, A., Maekawa, Y. & Miyasaka, T. Tin-based amorphous oxide: a high-capacity lithium-ion-storage material. *Science* 276, 1395-1397 (1997).

93 Amezawa, K., Yamamoto, N., Tomii, Y. & Ito, Y. Single-Electrode Peltier Heats of Li-Si Alloy Electrodes in LiCl-KCl Eutectic Melt. *J. Electrochem. Soc.* 145, 1986-1993 (1998).

94 Mao, O. & Dahn, J. Mechanically Alloyed Sn-Fe (-C) Powders as Anode Materials for Li-Ion Batteries: II. The Sn-Fe System. *J. Electrochem. Soc.* 146, 414-422 (1999).

95 Endo, M. *et al.* Vapor-grown carbon fibers (VGCFs): basic properties and their battery applications. *Carbon* 39, 1287-1297 (2001).

96 Kim, I.-S., Blomgren, G. & Kumta, P. Nanostructured Si/TiB_2 composite anodes for Li-ion batteries. *Electrochem. solid-state lett.* 6, A157-A161 (2003).

97 Kim, H., Seo, M., Park, M. H. & Cho, J. A Critical Size of Silicon Nano-Anodes for Lithium Rechargeable Batteries. *Angew. Chem. Int. Ed.* 49, 2146-2149 (2010).

98 Zhang, X.-W. *et al.* Electrochemical performance of lithium ion battery, nano-silicon-based, disordered carbon composite anodes with different microstructures. *J. Power sources* 125, 206-213 (2004).

99 Dong, H., Feng, R., Ai, X., Cao, Y. & Yang, H. Structural and electrochemical characterization of Fe–Si/C composite anodes for Li-ion batteries synthesized by mechanical alloying. *Electrochim. acta* 49, 5217-5222 (2004).

100 Wolf, H., Pajkic, Z., Gerdes, T. & Willert-Porada, M. Carbon–fiber–silicon-nanocomposites for lithium-ion battery anodes by microwave plasma chemical vapor deposition. *J. Power Sources* 190, 157-161 (2009).

101 Fu, Y., Yu, S.-l., Yu, Y.-z., Qiu, L.-P. & Hui, B. Reaction mode between Si and Fe and evaluation of optimal species in poly-silicic-ferric coagulant. *J.Environ.Sci.* 19, 678-688 (2007).

102 Yoshio, M. *et al.* Carbon-coated Si as a lithium-ion battery anode material. *J. Electrochem. Soc.* 149, A1598-A1603 (2002).

103 Kim, H. & Cho, J. Superior lithium electroactive mesoporous Si@ Carbon core− shell nanowires for lithium battery anode material. *Nano Lett.* 8, 3688-3691 (2008).

104 Liu, X. H. *et al.* In situ TEM experiments of electrochemical lithiation and delithiation of individual nanostructures. *Adv. Energy Mater.* 2, 722-741 (2012).
105 Obrovac, M. & Christensen, L. Structural changes in silicon anodes during lithium insertion/extraction. *Electrochem. Solid-State Lett.* 7, A93-A96 (2004).
106 Molenda, J., Delmas, C. & Hagenmuller, P. Electronic and electrochemical properties of Na_xCoO_{2-y} cathode. *Solid State Ionics* 431-435 (1983).
107 Pascal Ge, M. F. Electrochemical interaction of sodium in graphite. *Solid State Ionics* 28-30, 1172-1175 (1988).
108 Stevens, D. A. & Dahn, J. R. The Mechanisms of Lithium and Sodium Insertion in Carbon Materials. *J. Electrochem. Soc.* 148, A803-A811 (2001).
109 Cao, Y., *et al*. Sodium Ion Insertion in Hollow Carbon Nanowires for Battery Applications. *Nano lETT.* 12, 3783-3787 (2012).
110 Wenzel, S., Hara, T., Janek, J., & Adelhelm, P. Room-temperature sodium-ion batteries: Improving the rate capability of carbon anode materials by templating strategies. *Energy Environ. Sci.* 4, 3342-3345 (2011).
111 Tang, K., *et al*. Hollow Carbon Nanosphere with Superior Rate Capability for Sodium-Based Batteries. *Adv. Energy Mater.* 2, 873-877 (2012).
112 Wang, Y.-X., Chou, S.-L., Liu, H.-K. & Dou, S.-X. Reduced graphene oxide with superior cycling stability and rate capability for sodium storage. *Carbon* 57, 202-208 (2013).
113 Sangster, J. C-Na (Carbon-Sodium) System. *J. Phase Equilib. Deff.* 28, 571-579 (2007).
114 Chen, Q., Hou, S. S. & Schmidt-Rohr, K. A simple scheme for probehead background suppression in one-pulse H-1 NMR. *Solid State Nucl. Magn. Reson.* 26, 11-15 (2004).
115 Ishii, Y., Chimon, S. & Wickramasinghe, N. P. A new approach in 1D and 2D 13C high resolution solid-state NMR spectroscopy of paramagnetic organometallic complexes by very fast magic-angle spinning. *J. Am. Chem. Soc.* 125, 3438-3439 (2003).
116 Wickramasinghe, N. P. *et al.* Progress in 13C and 1H solid-state NMR for paramagnetic systems under very fast MAS. *J. Chem. Phys.* 128, 52210 (2008).
117 Yagi, T., Utsumi, W., Yamakata, M.-a., Kikegawa, T. & Shimomura, O. High-pressure in situ x-ray-diffraction study of the phase transformation from graphite to hexagonal diamond at room temperature. *Phys. Rev. B* 46, 6031-6039 (1992).
118 Ein-Eli, D. A. a. Y. The Study of Li-Graphite Intercalation Processes in Several Electrolyte Systems Using In Situ X-Ray Diffraction. *J. Electrochem. Soc.* 142, 1746-1752 (1995).
119 Lerf, A., He, H., Forster, M. & Klinowski, J. Structure of Graphite Oxide Revisited. *J. Phys. Chem. B* 102, 4477-4482 (1998).
120 Szabó, T., Berkesi, O., Forgó, P., Josepovits, K., Sanakis, Y., Petridis, D. & Dékány, I. Evolution of Surface Functional Groups in a Series of Progressively Oxidized Graphite Oxides. *Chem. Mater.* 18, 2740-2749 (2006).

121 Campos, M. F., Damasceno, J. C., Machado, R., & Achete, C. A. Auncertainty estimation of lattice parameters measured by x-ray diffraction. *Xviii imeko world congress Metrology for a Sustainable Development* (2006).
122 Xu, B. *et al.* What is the choice for supercapacitors: graphene or graphene oxide? *Energy Environ. Sci.* 4, 2826-2830 (2011).
123 Pierotti, R. A., & Rouquerol, J. Reporting physisorption data for gas/solid systems with special reference to the determination of surface area and porosity. *Pure Appl. Chem.* 57, 603-619 (1985).
124 Ng, S. H. *et al.* Correlations between surface properties of graphite and the first cycle specific charge loss in lithium-ion batteries. *Carbon* 47, 705-712 (2009).
125 Xing, W., Xue, J. S., & Dahn, J. R. Optimizing Pyrolysis of Sugar Carbons for Use as Anode Materials in Lithium-Ion Batteries. *J. Electrochem. Soc.* 143, 3046-3052 (1996).
126 Wang, Y., Alsmeyer, D. C. & McCreery, R. L. Raman Spectroscopy of Carbon Materials: Structural Basis of Observed Spectra. *Chem. Mater.* 2, 557-563 (1990).
127 Cai, W. *et al.* Synthesis and solid-state NMR structural characterization of 13C-labeled graphite oxide. *Science* 321, 1815-1817 (2008).
128 Casabianca, L. B., Shaibat, M., Cai, W., Park, S., Piner, R., Ruoff, R.S., & Ishii, Y. NMR-based structural modeling of graphite oxide using multi-dimensional 13C solid-state NMR and ab-initio chemical shift calculations. *J. Am. Chem. Soc.* 132, 5672-5676 (2010).
129 Gao, W., Alemany, L.B., Ci, L.J., & Ajayan, P.M. New insights into the structure and reduction of graphite oxide. *Nature Chem.* 1, 403-408 (2009).
130 DiVincenzo, D. & Mele, E. Cohesion and structure in stage-1 graphite intercalation compounds. *Phys. Rev. B* 32, 2538-2553 (1985).
131 Gotoh, K., *et al*. NMR study for electrochemically inserted Na in hard carbon electrode of sodium ion battery. *J. Power Sources* 225, 137-140 (2013).
132 Steven, D. A., & Dahn, J. R. High Capacity Anode Materials for Rechargeable Sodium-Ion Batteries. *J. Electrochem. Soc.* 147 (2000).
133 Shao, Y., *et al*. Surface-Driven Sodium Ion Energy Storage in Nanocellular Carbon Foams. *Nano Lett.* 13, 3909-3914 (2013).
134 Zhu, Y. & Wang, C. Galvanostatic Intermittent Titration Technique for Phase-Transformation Electrodes. *J. Phys. Chem.* 114, 2830-2841 (2009).
135 Augustyn, V., *et al*. High-rate electrochemical energy storage through LiC intercalation pseudocapacitance. *Nature Mater.* 12, 518-522 (2013).
136 Ardizzone, S., Fregonara, G. & Trasatti, S. "Inner" and "outer" active surface of RuO_2 electrodes. *Electrochim. Acta* 35, 263-267 (1990).
137 Mochida, I., Ku, C.-H., Yoon, S.-H. & Korai, Y. Anodic performance and mechanism of mesophase-pitch-derived carbons in lithium ion batteries. *J. Power Sources* 75, 214-222 (1998).

138 Liu, N., Wu, H., McDowell, M. T., Yao, Y., Wang, C., & Cui, Y. A yolk-shell design for stabilized and scalable Li-Ion battery alloy anodes. *Nano Lett.* 12, 3315-3321 (2012).

139 Liu, N. *et al.* A pomegranate-inspired nanoscale design for large-volume-change lithium battery anodes. *Nature Nanotech.* 9, 187-192 (2014).

140 Wang, L. *et al.* Nano-Structured Phosphorus Composite as High-Capacity Anode Materials for Lithium Batteries. *Angew. Chem. Int. Ed.* 51, 9034-9037 (2012).

141 Palomares, V. *et al.* Na-ion batteries, recent advances and present challenges to become low cost energy storage systems. *Energy Environ. Sci.* 5, 5884-5901 (2012).

142 Kim, S. W., Seo, D. H., Ma, X., Ceder, G. & Kang, K. Electrode Materials for Rechargeable Sodium-Ion Batteries: Potential Alternatives to Current Lithium-Ion Batteries. *Adv. Energy Mater.* 2, 710-721 (2012).

143 Kim, Y. et al. An Amorphous Red Phosphorus/Carbon Composite as a Promising Anode Material for Sodium Ion Batteries. Adv. Mater. 25, 3045-3049 (2013).

144 Qian, J., Wu, X., Cao, Y., Ai, X. & Yang, H. High capacity and rate capability of amorphous phosphorus for sodium ion batteries. *Angewandte Chemie* 125, 4731-4734 (2013).

145 Ji, X., Lee, K. T. & Nazar, L. F. A highly ordered nanostructured carbon–sulphur cathode for lithium–sulphur batteries. *Nature mater.* 8, 500-506 (2009).

146 Sun, C.-F., *et al*. A Beaded-String Silicon Anode. *ACS Nano* 7, 2717-2724 (2013).

147 Qian, J., Xiong, Y., Cao, Y., Ai, X. & Yang, H. Synergistic Na-Storage Reactions in Sn4P3 as a High-Capacity, Cycle-stable Anode of Na-Ion Batteries. *Nano lett.*14, 1865-1869 (2014).

148 Li, W. *et al.* $Sn_{4+x}P_3$@ Amorphous Sn-P Composites as Anodes for Sodium-Ion Batteries with Low Cost, High Capacity, Long Life, and Superior Rate Capability. *Adv.Mater.* (2014).

Innovation of the Dissertation Work

1. New method for synthesis of Si-graphene was developed to achieve long cycling stability. Different from existing technology that physically blending the Si and graphene, chemical bonding between the two components was created to enhance the structure stability and electrical conductivity.
2. Novel in situ bottom-up fabrication method was developed to fabricate the Si-carbon nanotubes (CNT) anode. Different from traditional synthesis method, the carbon frame work consisting of CNT was directly grown on the Si surface through metal catalyst chemical vapor deposition, which is a superior approach to engineer the Si-carbon composites with good electrochemical performance and optimal Si-carbon ratio.
3. For the first time, expanded graphite was designed and studied for NIB anode. Different from the most studied amorphous carbon NIB anode, EG allows reversible Na^+ intercalation and stores the Na ions in a similar way that graphite stores Li ions. The robustness of the layer structure of EG ensures long cyclic ability. And the EG material could be a good candidate for next generation NIBs.
4. Novel method was used to improve the red phosphorus NIB anode. Instead of the typical ball-milling mixing, red phosphorus was loaded on the carbon frame work by evaporation/adsorption method. The gas infusion approach provides more possibilities of engineering P-carbon composites with various morphologies. And the novel beaded-string P-CNT composite shows superior cycling performance than the reported P-carbon.

List of Publications and Conference Proceedings

Peer-reviewed Journal Publications

Y. Wen, Y. Zhu, A. Langrock, A. Manivannan, S. H. Ehrman, C. Wang. "Graphene-Bonded and -Encapsulated Si Nanoparticles for Lithium Ion Battery Anodes". *Small.* 9(16), 2810-2816(2013)

Y. Wen, K. He, Y. Zhu, F. Han, Y. Xu, I. Matsuda, Y. Ishii, J. Cumings, C. Wang. "Expanded Graphite as Superior Anode for Sodium-Ion Batteries". *Nature Communications*. 5(2014):4033.

C. Luo, Y. Zhu, Y. Wen, J. Wang, C. Wang, "Carbonized Polyacrylonitrile Stabilized SeSx Cathodes for Long Cycle Life and High Power Density Lithium Ion Batteries, *Advanced Functional Materials,* In press.

S. Zheng, Y. Wen, Y. Zhu, Z. Han, J. Wang, J. Yang, C. Wang, "In-situ Sulfur Reduction and Intercalation of Graphite Oxides for Li-S Battery Cathodes" *Advanced Energy Materials,* Accepted

Y. Xu, Y. Wen, Y. Zhu, K. Gaskell, B. Eichhorn, K. Xu, C. Wang, "Confined Sulphur in C/S_2 Composites Renders Superior Cycling Stability in Li/S Battery", *Nature Communications*, Under Review

Conference Proceedings

Y. Wen, C. Wang, " Graphene-encapsulated-Si-Nanoparticles for Li-ion Battery anodes", Poster Presentation. *2012 EFRC-NEES Semi-annual Meeting*. Silver Spring, MD 2012

Y. Wen, K. He, J. Cumings, C. Wang. "In-situ TEM Study on Sodiation/Desodiation of Expanded Graphite". Poster Presentation. *2013 DOE Energy Frontier Research Centers Principal Investigators' Meeting*. Washington DC, 2013

Y. Wen, C. Wang, " Red Phosphorus @ Porous Carbon for Na-ion Batteries". Oral Presentation. *225th Electrochemistry Society Meeting.* Orlando, FL 2014